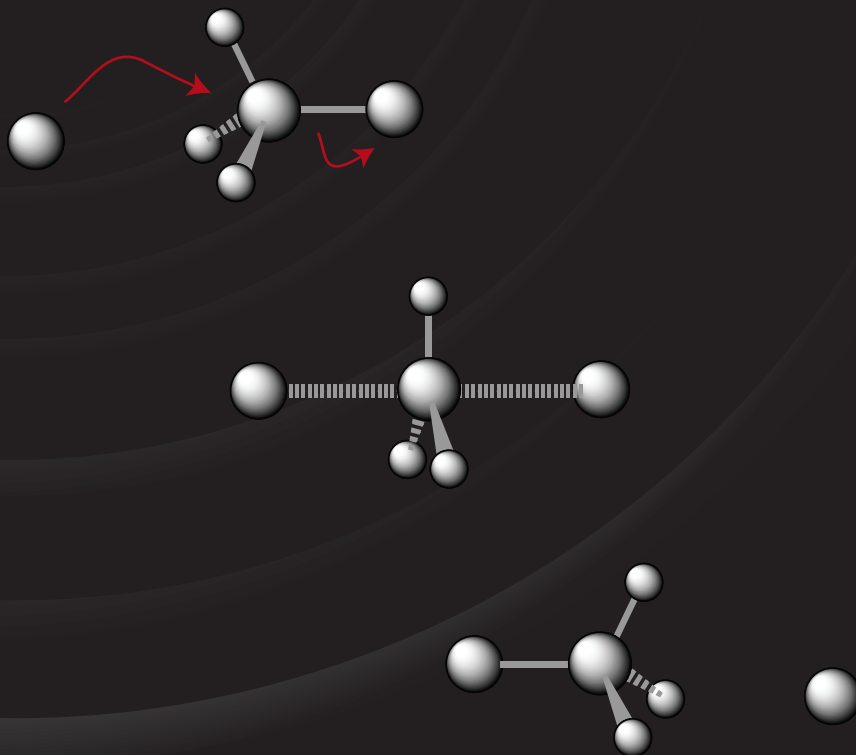


Theoretical Study on the Origin of Reaction Barriers



A. Patrícia Bento

VRIJE UNIVERSITEIT

Nucleophilic Substitution Reactions

Theoretical Study on the Origin of Reaction Barriers

ACADEMISCH PROEFSCHRIFT

ter verkrijging van de graad Doctor aan
de Vrije Universiteit Amsterdam,
op gezag van de rector magnificus
prof.dr. L.M. Bouter,
in het openbaar te verdedigen
ten overstaan van de promotiecommissie
van de faculteit der Exact Wetenschappen
op maandag 27 oktober 2008 om 10.45 uur
in de aula van de universiteit,
De Boelelaan 1105

door

Ana Patrícia dos Santos Franco Ferreira Bento

geboren te Porto, Portugal

promotor: prof.dr. E.J. Baerends
copromotor: dr. F.M. Bickelhaupt

Nucleophilic Substitution Reactions

Theoretical Study on the Origin of Reaction Barriers

A. Patrícia Bento

Contents

| | | |
|----------|--|-----------|
| 1 | <i>Introduction</i> | 9 |
| 1.1. | From Experiments to Theory | 9 |
| 1.2. | This Thesis | 11 |
| | References | 12 |
| 2 | <i>Theory and Methods</i> | 15 |
| 2.1. | <i>Ab Initio</i> Theory | 15 |
| 2.2. | Density Functional Theory | 17 |
| 2.3. | Activation Strain Model of Chemical Reactivity | 19 |
| | References | 20 |
| 3 | <i>Ab Initio and DFT Benchmark Study for Nucleophilic Substitution at Carbon ($S_N2@C$) and Silicon ($S_N2@Si$)</i> | 23 |
| 3.1. | Introduction | 25 |
| 3.2. | Methods | 27 |
| 3.2.1. | DFT Geometries and Potential Energy Surfaces | 27 |
| 3.2.2. | <i>Ab Initio</i> Potential Energy Surfaces | 28 |
| 3.3. | Results and Discussion | 26 |
| 3.3.1. | Geometries of Stationary Points | 26 |
| 3.3.2. | <i>Ab Initio</i> Benchmark Potential Energy Surfaces | 30 |
| 3.3.3. | Validation of DFT Potential Energy Surfaces | 32 |
| 3.4. | Conclusions | 34 |
| | References | 35 |
| 4 | <i>E2 and S_N2 Reactions of $X^- + CH_3CH_2X$. An <i>Ab Initio</i> and DFT Benchmark Study</i> | 39 |
| 4.1. | Introduction | 41 |
| 4.2. | Methods | 43 |
| 4.2.1. | DFT Geometries and Potential Energy Surfaces | 43 |
| 4.2.2. | <i>Ab Initio</i> Potential Energy Surfaces | 43 |
| 4.3. | Results and Discussion | 44 |

| | |
|---|----|
| 4.3.1. Geometries of Stationary Points and Reaction Paths | 44 |
| 4.3.2. <i>Ab Initio</i> Benchmark Potential Energy Surfaces | 46 |
| 4.3.3. Validation of DFT: Mean Absolute Error | 49 |
| 4.3.4. Validation of DFT: Trends | 54 |
| 4.4. Conclusions | 55 |
| References | 56 |

5 *Nucleophilic Substitution at Silicon via a Central Reaction Barrier* 61

| | |
|--|----|
| 5.1. Introduction | 63 |
| 5.2. Methods | 65 |
| 5.2.1. Computational Details | 65 |
| 5.2.2. Analysis of the Potential Energy Surfaces | 65 |
| 5.3. Results and Discussion | 66 |
| 5.3.1. Potential Energy Surfaces | 66 |
| 5.3.2. Activation Strain Analyses of the Model Reactions | 68 |
| 5.3.2.1. Nucleophilic Substitution at Carbon | 70 |
| 5.3.2.2. Nucleophilic Substitution at Silicon | 71 |
| 5.3.2.3. Introducing Bulky Substituents | 72 |
| 5.4. Conclusions | 74 |
| References | 74 |

6 *Frontside versus Backside S_N2 Substitution at Group-14 Atoms: Origin of Reaction Barriers and Reasons for their Absence* 77

| | |
|--|----|
| 6.1. Introduction | 79 |
| 6.2. Methods | 81 |
| 6.2.1. Computational Details | 81 |
| 6.2.2. Analysis of the Potential Energy Surfaces | 82 |
| 6.3. Results and Discussion | 82 |
| 6.3.1. Backside S _N 2-b: Reaction Profiles | 82 |
| 6.3.2. Frontside S _N 2-f: Reaction Profiles | 84 |
| 6.3.3. Frontside S _N 2-f: Berry Pseudorotation and/or Turnstile Rotation? | 86 |
| 6.3.4. Backside S _N 2-b: Activation Strain Analyses | 88 |
| 6.3.5. Frontside S _N 2-f: Activation Strain Analyses | 90 |
| 6.3.6. Relativistic Effects | 91 |
| 6.4. Conclusions | 92 |
| References | 93 |

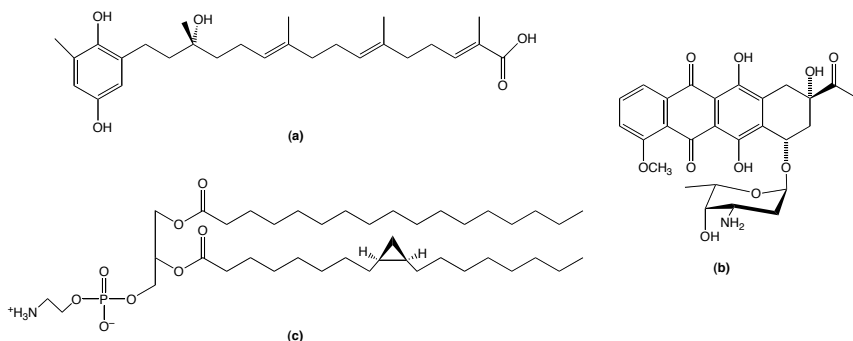
| | |
|--|------------|
| 7 Nucleophilicity and Leaving-Group Ability in Frontside and Backside S_N2 Reactions | 97 |
| 7.1. Introduction | 99 |
| 7.2. Methods | 100 |
| 7.2.1. Computational Details | 100 |
| 7.2.2. Analysis of the Potential Energy Surfaces | 101 |
| 7.3. Results and Discussion | 102 |
| 7.3.1. Reaction Profiles Backside S_N2 -b | 102 |
| 7.3.2. Reaction Profiles Frontside S_N2 -f | 106 |
| 7.3.3. Activation Strain Analyses: Nucleophilicity in S_N2 -b | 107 |
| 7.3.4. Activation Strain Analyses: Leaving-Group Ability in S_N2 -b | 111 |
| 7.3.5. Activation Strain Analyses: S_N2 -f versus S_N2 -b | 111 |
| 7.4. Conclusions | 113 |
| References | 113 |
| Summary | 117 |
| Samenvatting | 121 |
| Acknowledgements | 125 |
| List of Publications | 127 |

1 Introduction

1.1. From Experiments to Theory

Bimolecular nucleophilic substitution (S_N2) is one of the most fundamental chemical transformations. The enormous amount of interest in this mechanism lies in the fact that it plays a central role, not only, in organic chemistry^{1,2} but also in biological systems.³⁻⁶ S_N2 reactions occur, for example, in the synthesis of compounds like the Chrysochlamic Acid (Scheme 1.1a), an inhibitor of a DNA polymerase that is involved in the DNA repair,³ and Daunorubicin (Scheme 1.1b), a widely used anti-tumor drug.^{4,7} Moreover, they play a key role in the formation of Cyclopropane Fatty Acid (Scheme 1.1c) that, in *Escherichia coli*'s membrane, is a major factor in acid resistance of the bacterium.^{5,8}

Scheme 1.1. Structures of (a) Chrysochlamic Acid, (b) Daunorubicin and (c) Cyclopropane Fatty Acid.



Much insight⁹⁻¹⁴ into how S_N2 substitution reactions occur has emerged since, in the early 1930s, Hughes and Ingold have rationalized their observations and characterized this class of reactions.² Its mechanism (in the anionic form)



has been described as being kinetically of first order in each of the reactants, the nucleophile X and the substrate MY (second order overall). It was postulated that the observed second order kinetics is the result of the well-known Walden inversion reaction,

in which the nucleophile X displaces the leaving group Y from the backside in a single concerted reaction step.

Much of this insight comes from experiments in the condensed phase. However, solvation effects are likely to mask the intrinsic nature of the reaction system which may lead to an ambiguous and erroneous interpretation of the mechanism. Thus, it is important to perform mechanistic studies on this class of reactions in the gas phase, i.e., without the interference of surrounding molecules. In this way, the intrinsic behavior of these processes may be studied and the role of solvent exposed by comparing the gas-phase results with those of condensed-phase experiments.

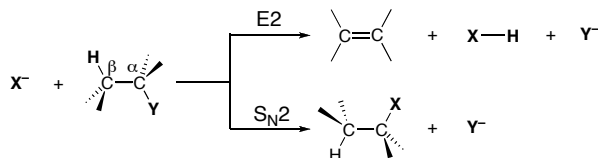
Most of S_N2 substitutions are ionic and thus they are well suited for mass spectrometry investigations. In pioneering work, Olmstead and Brauman¹² have proposed that, in gas-phase S_N2 reactions, the ion and molecule collide at a rate determined by the long-range attractive forces between them and that the overall efficiency of the reactions is determined by the competition between the dissociation of the resulting collision complex back into the reactants and the overcoming of the central barrier to the second ion-molecule complex. These conclusions gave rise to the well-known double-well potential energy surface (PES) associated with gas-phase reactions.

After their work, a large number of reactions have been studied using techniques like flowing afterglow^{14,15} (FA) and Fourier transform-ion cyclotron resonance^{13,16} (FT-ICR). However, there are experimental limitations on the range of rates that can be studied in the gas phase. As discussed before, in a gas-phase nucleophilic substitution, the ion and molecule, both initially at room temperature, are strongly attracted to one another, resulting in a long-lived reactant complex. The complex may eventually dissociate with loss of its attractive force, but during its lifetime a reaction may occur. Under low-pressure conditions, this reaction is only efficient if the energy barrier is below or only slightly above the energy of the reactants. Furthermore, entropy effects also play an important role in addition to the energetics of the reaction profile. For example, dissociation of the reactant complex is entropically favored over the highly structured S_N2 displacement step for reactions with a central barrier. Thus, even reactions with a negative overall energy barrier may occur with low efficiency. At variance, for exothermic reactions with an insignificant barrier, the displacement may occur at nearly every encounter. Heating or cooling the reactants has only a minor effect on the rate of the reactions, since most of the energy for surmounting the barrier comes from the attractive potential. Thus, there is a relatively small range of reactions that have measurable rates and which therefore can be studied experimentally in the gas phase.

These experimental problems are compounded by the fact that many conditions that favor S_N2 substitutions are similar to those that promote base-induced eliminations (E2)^{10,14,17} and thus discriminating between the two pathways is problematic, since they

lead to different neutral species but to the same ionic product, and are therefore not distinguishable through mass spectrometric techniques (Scheme 1.2).

Scheme 1.2. E2 and S_N2 reactions.



Due to all these difficulties in experimental investigations and in the interpretation of the experimental data in terms of potential energy surfaces, computational chemistry methods have arisen as a sound and efficient alternative for the study of potential energy surfaces for the gas-phase nucleophilic substitution reactions. Computational methods, not only, do not suffer from the above experimental limitations, but they can also model these and other reactions⁹ in a reliable and accurate way, providing data from which experimentalists may gain insight and thereby rationalize the behavior of a large class of reactions. In this way, computational methods have become an indispensable tool for complementing experimental investigations.

1.2. This Thesis

In this thesis, a computational study on gas-phase nucleophilic substitution reactions using mainly density functional theory (DFT) calculations is presented. The purpose of the work described herein is twofold. In the first place, the purpose is to evaluate and validate the performance of several popular density functionals in describing S_N2 substitution and E2 elimination reactions. This is done by first computing highly accurate *ab initio* benchmark PESes for this class of reactions against which the various DFT PESes can be validated. Although *ab initio* theory is satisfactory in terms of accuracy and reliability, it is at the same time prohibitively expensive if one wishes to study more realistic model reactions involving larger nucleophiles and substrates (see Chapter 2 for a description of the quantum theoretical approaches used to perform the computational studies reported in this thesis). A survey of density functionals serves thus to validate one or more of these DFT approaches as a computationally more efficient alternative to high-level *ab initio* theory in future investigations. The results of these validation studies are presented in Chapters 3 and 4.

A second purpose is to understand gas-phase S_N2 substitutions, in particular, when it comes to the factors affecting their intrinsic reactivity, such as, the steric hindrance in the substrate, the center of nucleophilic attack and the nucleophilicity and leaving-group ability. The long-term goal is to contribute to a more rational and thus efficient design of

chemical reactions. Thus, in Chapter 5, the PESes of various $\text{Cl}^- + \text{CR}_3\text{Cl}$ ($\text{R} = \text{H}, \text{CH}_3$) and $\text{Cl}^- + \text{SiR}_3\text{Cl}$ model reactions ($\text{R} = \text{H}, \text{CH}_3, \text{C}_2\text{H}_5$ and OCH_3) have been investigated. If $\text{R} = \text{H}$, the former proceeds via a central reaction barrier which disappears in the latter. While this phenomenon as such is well known, it is still not fully understood. Why does the central reaction barrier disappear if we go from $\text{S}_{\text{N}}2@C$ to the corresponding $\text{S}_{\text{N}}2@Si$ process? And what causes the existence of a central barrier for $\text{S}_{\text{N}}2@C$ in the first place? Is there an electronic factor responsible for the barrier in the case of $\text{S}_{\text{N}}2@C$ (e.g., less favorable bonding capability of carbon as compared to silicon) or is this barrier steric in origin, i.e., caused by repulsion between substituents around the smaller carbon atom? These and other questions will be answered in this chapter. In Chapter 6, a study on how the potential energy surfaces along the reaction coordinate ζ vary as the center of nucleophilic attack changes from carbon to the heavier group-14 atoms is presented. This is done not only for the more common backside reaction but also for the frontside pathway. Moreover, the question in how far the trends are influenced by relativistic effects, especially for the heaviest group-14 congeners, is explored. Finally, in Chapter 7, the concepts of nucleophilicity and leaving-group ability are examined. They have been related to various reactant properties, such as, electronegativity, size, polarizability and others. Yet, the state of the art is still to some extent phenomenological. In this chapter, we develop a straightforward, causal relationship between the reactants' electronic structure and their $\text{S}_{\text{N}}2$ reactivity.

References

- 1 Smith, M. B.; March, J. *March's Advanced Organic Chemistry: Reactions, Mechanisms, and Structure*; Wiley: New York, 2007; Carey, F. A.; Sundberg, R. J. *Advanced Organic Chemistry, Part A*; 5th ed.; Springer: New York, 2007; Lowry, T. H.; Richardson, K. S. *Mechanism and Theory in Organic Chemistry*; Harper and Row: New York, 1987.
- 2 Ingold, C. *Structure and Mechanism in Organic Chemistry*; 2nd ed.; Cornell University Press: Ithaca, NY, 1969.
- 3 Maloney, D. J.; Hecht, S. M. *Org. Lett.* **2005**, 7, 4297.
- 4 Jansson, A.; Koskiniemi, H.; Mäntsälä, P.; Niemi, J.; Schneider, G. *J. Biol. Chem.* **2004**, 279, 41149.
- 5 Iwig, D. F.; Grippe, A. T.; McIntyre, T. A.; Booker, S. J. *Biochemistry* **2004**, 43, 13510.
- 6 Rodgers, J.; Femec, D. A.; Schowen, R. L. *J. Am. Chem. Soc.* **1982**, 104, 3263.

- 7 Barone, G.; Fonseca Guerra, C.; Gambino, N.; Silvestri, A.; Lauria, A.; Almerico, A. M.; Bickelhaupt, F. M. *J. Biomol. Struct. Dyn.* **2008**, 26, 115.
- 8 Chang, Y.-Y.; Cronan Jr., J. E. *Mol. Microbiol.* **1999**, 33, 249.
- 9 Bento, A. P.; Bickelhaupt, F. M. *J. Org. Chem.* **2007**, 72, 2201; Vayner, G.; Houk, K. N.; Jorgensen, W. L.; Brauman, J. I. *J. Am. Chem. Soc.* **2004**, 126, 9054; Botschwina, P. *Theor. Chem. Acc.* **1998**, 99, 426; Chandrasekhar, J.; Smith, S. F.; Jorgensen, W. L. *J. Am. Chem. Soc.* **1985**, 107, 154; Lee, I.; Kim, C. K.; Sohn, C. K.; Li, H. G.; Lee, H. W. *J. Phys. Chem. A* **2002**, 106, 1081; van Bochove, M. A.; Swart, M.; Bickelhaupt, F. M. *ChemPhysChem* **2007**, 8, 2452; Bach, R. D.; Dmitrenko, O.; Thorpe, C. J. *Org. Chem.* **2008**, 73, 12; van Bochove, M. A.; Bickelhaupt, F. M. *Eur. J. Org. Chem.* **2008**, 649; Glukhovtsev, M. N.; Pross, A.; Radom, L. *J. Am. Chem. Soc.* **1995**, 117, 2024; Norton, S. H.; Bachrach, S. M.; Hayes, J. M. *J. Org. Chem.* **2005**, 70, 5896; Bachrach, S. M.; Pereverzev, A. *Org. Biomol. Chem.* **2005**, 3, 2095; Deng, L.; Branchadell, V.; Ziegler, T. *J. Am. Chem. Soc.* **1994**, 116, 10645; Harder, S.; Streitwieser, A.; Petty, J. T.; Schleyer, P. v. R. *J. Am. Chem. Soc.* **1995**, 117, 3253; Bickelhaupt, F. M. *J. Comput. Chem.* **1999**, 20, 114; van Bochove, M. A.; Swart, M.; Bickelhaupt, F. M. *J. Am. Chem. Soc.* **2006**, 128, 10738; Pierrefixe, S. C. A. H.; Fonseca Guerra, C.; Bickelhaupt, F. M. *Chem. Eur. J.* **2008**, 14, 819.
- 10 Gronert, S. *Acc. Chem. Res.* **2003**, 36, 848.
- 11 Laerdahl, J. K.; Uggerud, E. *Int. J. Mass Spectrom.* **2002**, 214, 277; Chabiny, M. L.; Craig, S. L.; Regan, C. K.; Brauman, J. I. *Science* **1998**, 279, 1882; Shaik, S. S.; Schlegel, H. B.; Wolfe, S. *Theoretical Aspects of Physical Organic Chemistry: The S_N2 Mechanism*; Wiley: New York, 1992; Carvalho, A. T. P.; Swart, M.; van Stralen, J. N. P.; Fernandes, P. A.; Ramos, M. J.; Bickelhaupt, F. M. *J. Phys. Chem. B* **2008**, 112, 2511; Graul, S. T.; Bowers, M. T. *J. Am. Chem. Soc.* **1991**, 113, 9696; Viggiano, A. A.; Morris, R. A.; Paschkewitz, J. S.; Paulson, J. F. *J. Am. Chem. Soc.* **1992**, 114, 10477; Li, C.; Ross, P.; Szulejko, J. E.; McMahon, T. B. *J. Am. Chem. Soc.* **1996**, 118, 9360; Bickelhaupt, F. M.; de Koning, L. J.; Nibbering, N. M. M.; Baerends, E. J. *J. Phys. Org. Chem.* **1992**, 5, 179.
- 12 Olmstead, W. N.; Brauman, J. I. *J. Am. Chem. Soc.* **1977**, 99, 4219.
- 13 Nibbering, N. M. M. *Acc. Chem. Res.* **1990**, 23, 279; Bickelhaupt, F. M.; Buisman, G. J. H.; de Koning, L. J.; Nibbering, N. M. M.; Baerends, E. J. *J. Am. Chem. Soc.* **1995**, 117, 9889.
- 14 DePuy, C. H.; Gronert, S.; Mulin, A.; Bierbaum, V. M. *J. Am. Chem. Soc.* **1990**, 112, 8650.
- 15 Bohme, D. K.; Raksit, A. B. *J. Am. Chem. Soc.* **1984**, 106, 3447; Damrauer, R.; DePuy, C. H.; Bierbaum, V. M. *Organometallics* **1982**, 1, 1553; Barlow, S. E.; Van

- Doren, J. M.; Bierbaum, V. M. *J. Am. Chem. Soc.* **1988**, *110*, 7240; Bohme, D. K.; Mackay, G. I. *J. Am. Chem. Soc.* **1981**, *103*, 978.
- 16 Wladkowski, B. D.; Brauman, J. I. *J. Phys. Chem.* **1993**, *97*, 13158; van der Wel, H.; Nibbering, N. M. M.; Sheldon, J. C.; Hayes, R. N.; Bowie, J. H. *J. Am. Chem. Soc.* **1987**, *109*, 5823; Wladkowski, B. D.; Brauman, J. I. *J. Am. Chem. Soc.* **1992**, *114*, 10643; Nibbering, N. M. M. *Mass Spectrom. Rev.* **2006**, *25*, 962.
- 17 Gronert, S.; Pratt, L. M.; Mogali, S. *J. Am. Chem. Soc.* **2001**, *123*, 3081; Bickelhaupt, F. M.; de Koning, L. J.; Nibbering, N. M. M. *J. Org. Chem.* **1993**, *58*, 2436; Uggerud, E.; Bache-Andreassen, L. *Chem. Eur. J* **1999**, *5*, 1917; Gronert, S.; Fagin, A. E.; Okamoto, K.; Mogali, S.; Pratt, L. M. *J. Am. Chem. Soc.* **2004**, *126*, 12977; Villano, S. M.; Kato, S.; Bierbaum, V. M. *J. Am. Chem. Soc.* **2006**, *128*, 736; Flores, A. E.; Gronert, S. *J. Am. Chem. Soc.* **1999**, *121*, 2627.

2 Theory and Methods

This chapter briefly describes the quantum theoretical approaches used to perform the computational studies reported in this thesis. First, Section 2.1 overviews the fundamental features of *ab initio* theory. Next, Section 2.2 focuses on the foundations of density functional (DFT) theory. Finally, in Section 2.3, a brief description of the Activation Strain model is given. This model has been used to understand the chemical reactions explored throughout this thesis and, in particular, the origin of their reaction barriers.

2.1. *Ab Initio* Theory

Ab initio quantum chemistry theory has its foundations in quantum mechanics.¹ It is a postulate of quantum mechanics that the state of a system is fully described by its wavefunction Ψ , which evolves in time according to the equation

$$i\hbar \frac{\partial \Psi}{\partial t} = H\Psi \quad (2.1)$$

This is the Schrödinger equation, introduced by Erwin Schrödinger in 1926.² In this equation, H is the Hamiltonian operator, which corresponds to the total energy of the system. If the total energy does not depend on time, the Schrödinger equation can be separated into a time-dependent and time-independent part. The Schrödinger equation can then be rewritten as

$$H\Psi = E\Psi \quad (2.2)$$

Unfortunately, this equation cannot be solved analytically for all but the simplest systems. Thus, one of the further approximations used in all calculations in this work is the Born-Oppenheimer approximation,³ which states that electronic and nuclear motions can be separated due to the difference in mass (and therefore the difference in time scales of motion) between the electrons and the nuclei. In this way, the electronic energies for fixed nuclear positions are calculated.

As proposed by Wolfgang Pauli, the wavefunction describing the electrons must be antisymmetric with respect to the interchange of any pair of electrons, which is to say that when two electrons are exchanged, the wavefunction must change sign. The simplest way to satisfy this constraint is to approximate the wavefunction Ψ with a linear combination of Slater determinants Ψ_{SD}

$$\Psi_{\text{SD}} = \frac{1}{\sqrt{n!}} \begin{vmatrix} \psi_1(1) & \psi_2(1) & \cdots & \psi_n(1) \\ \psi_1(2) & \psi_2(2) & \cdots & \psi_n(2) \\ \vdots & \vdots & \ddots & \vdots \\ \psi_1(n) & \psi_2(n) & \cdots & \psi_n(n) \end{vmatrix} \quad (2.3)$$

In this equation, ψ_i are single-electron wavefunctions, called orbitals, and n is the total number of electrons. Although the exact electronic wavefunction is given by an infinite sum of Ψ_{SD} , a further approximation can be made in which only one determinant is used. This approximation implies that the electron-electron repulsion is taken into account as an average effect and not explicitly. This is the so-called Hartree-Fock method. Invoking the variational principle, one can find the set of orbitals ψ_i that give the most accurate total wavefunction Ψ_{SD} , which corresponds to the wavefunction Ψ_{SD} associated with the lowest energy. The Hartree-Fock energy is an upper bound of the exact energy and tends to a limiting value called the Hartree-Fock limit as the basis set is improved. A basis set is a set of functions used to describe the orbitals. In practice, the orbitals ψ_i are approximated by a linear combination of the basis functions φ_j

$$\psi_i = \sum_j c_{ji} \varphi_j \quad (2.4)$$

Basically, solving the Schrödinger equation in the Hartree-Fock approximation consists of finding a set of coefficients c_{ji} which minimizes the energy of the electronic system. The basis functions φ_j are chosen such that the wavefunction approaches the Hartree-Fock limit as closely as possible. This objective must be in balance with the restrictions imposed by the computational resources. In this thesis, we used basis sets of quality of up to augmented correlation consistent polarized valence basis set of quadruple- ζ quality.

For molecules, Hartree-Fock is the central starting point for most *ab initio* quantum chemistry methods, which are then subsequently corrected for Coulomb correlation, which is not taken into account at the Hartree-Fock level. Including correlation generally improves the accuracy of computed energies and molecular geometries. At present, there exists a wide range of methods to include electron correlation. In general, in *ab initio* theory, it consists of using a multi-determinant trial wavefunction by including excited

states from the reference Hartree-Fock wavefunction. In this thesis, we have been able to treat electron correlation at the level of coupled-cluster theory with single and double excitations and triple excitations treated perturbatively.

In general, *ab initio* calculations can yield increasingly accurate quantitative results as the molecule in question becomes smaller. However, computationally, these methods are very expensive, since it often takes enormous amount of computer CPU time, memory and disk space. Moreover, the Hartree-Fock method formally scales as N^4 (although better scaling algorithms have been developed in practice), where N is the number of basis functions, meaning that a calculation ten times as big takes ten thousand times as long to complete. Correlated calculations scale in general much worse than this.

In this thesis, these methods were used to obtain reliable benchmarks for the potential energy surfaces of nucleophilic substitution and elimination reactions. This will be discussed further in Chapters 3 and 4.

2.2. Density Functional Theory

The *ab initio* methods are widely used by quantum chemists. However, as discussed above, they do have limitations, in particular the computational difficulty of performing accurate calculations with large basis sets on molecules containing many atoms and many electrons.

A more efficient alternative is provided by density functional theory⁴ (DFT). The premise behind DFT is the proof by Hohenberg and Kohn⁵ that the energy of a molecule can be determined from the electron density instead of a wavefunction. Thus the energy is a functional of the electron density: $E = E[\rho]$. A practical application of this theory was developed by Kohn and Sham. The basic ingredient of the Kohn-Sham approach⁶ is the postulation of a reference system of N non-interacting electrons, moving in an effective local external potential, $v_s(\mathbf{r})$, such that its density, $\rho_s(\mathbf{r})$, is equal to the exact density, $\rho(\mathbf{r})$, of the interacting electron system. Thus, according to the Kohn-Sham theorem,⁶ the exact energy functional can be expressed as

$$E[\rho(\mathbf{r})] = T_s[\rho(\mathbf{r})] + E_n[\rho(\mathbf{r})] + E_C[\rho(\mathbf{r})] + E_{XC}[\rho(\mathbf{r})] \quad (2.5)$$

in which the exact electron density can be expressed as a linear combination of the Kohn-Sham orbital densities:

$$\rho(\mathbf{r}) = \sum_i |\phi_i|^2 \quad (2.6)$$

In eq 2.5, $T_S[\rho(\mathbf{r})]$ represents the kinetic energy of the electrons of the non-interacting reference system, $E_n[\rho(\mathbf{r})]$ is the electrostatic attraction between the electrons and the nuclei, and $E_C[\rho(\mathbf{r})]$ is the classical Coulomb repulsion of the electronic cloud with itself. $E_{xc}[\rho(\mathbf{r})]$ is the so-called exchange-correlation energy, which accounts, not only for the self-interaction correction, exchange and Coulomb correlation between electrons but also includes a correction for the fact that $T_S[\rho(\mathbf{r})]$ differs from the exact kinetic energy $T[\rho(\mathbf{r})]$.

The orbitals ϕ_i can be obtained from the effective one-electron Kohn-Sham equation

$$\begin{aligned} h_{eff}\phi_i &= \varepsilon_i\phi_i \\ \left[-\frac{1}{2}\nabla^2 + v_S(\mathbf{r}) \right] \phi_i &= \varepsilon_i\phi_i \end{aligned} \quad (2.7)$$

Here, the Kohn-Sham potential, $v_S(\mathbf{r})$, that the reference electron experiences comprises the attractive potential, $v(\mathbf{r})$, of the nuclei and the classical Coulomb repulsion, $V_C[\rho(\mathbf{r})]$, with the electron density $\rho(\mathbf{r})$, as well as the self-interaction correction and all exchange and correlation effects contained in the so-called exchange-correlation potential, $V_{xc}[\rho(\mathbf{r})]$.

The exact exchange-correlation potential, $V_{xc}[\rho(\mathbf{r})]$, is not known and thus several approximations have been developed. These include the local density approximation (LDA), which assumes that the exchange-correlation energy at any point in space is a function of the electron density at that point in space and the generalized gradient approximations (GGAs), in which the exchange and correlation energies depend not only on the density but also on its gradient $\nabla\rho(\mathbf{r})$. The quality of these approximations determines the level of density functional theory applied. In this thesis, most DFT calculations have been carried out using the OPTX functional for exchange⁷ and the Lee-Yang-Parr functional for correlation.⁸

For molecular systems with heavy elements, as is the case of the model systems studied in this thesis, it is necessary to include relativistic effects to correctly describe the behavior of the heavy elements. This is so, because the electrons closest to the heavy nuclei can reach velocities approaching the speed of light. In this thesis, the model reactions with heavy elements were performed using relativistic DFT methods, which were formulated using the zero-order regular approximation (ZORA).⁹ For more details, the reader is referred to the literature.⁹

2.3. Activation Strain Model of Chemical Reactivity

One of the goals of this thesis includes gathering insight into how the activation barriers arise. This insight is obtained through the Activation Strain analyses of the various model reactions studied in this thesis.^{10,11} The Activation Strain model^{10,11} of chemical reactivity is a fragment approach to understanding chemical reactions in which the height of reaction barriers is described and understood in terms of the original reactants. For earlier applications of the fragment concept, see also, for example, Ref. 12-15. In this model, the entire reaction profile $\Delta E(\zeta)$ is decomposed, along the reaction coordinate ζ , into the strain $\Delta E_{\text{strain}}(\zeta)$ associated with deforming the individual reactants, plus the actual interaction $\Delta E_{\text{int}}(\zeta)$ between the deformed reactants (eq 2.8; see also Figure 2.1). The reaction profiles were generated and analyzed using the Pyfrag program.¹¹

$$\Delta E(\zeta) = \Delta E_{\text{strain}}(\zeta) + \Delta E_{\text{int}}(\zeta) \quad (2.8)$$

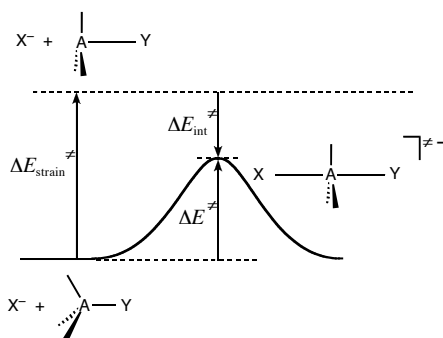


Figure 2.1. Illustration of the Activation Strain model in the case of a backside nucleophilic substitution of $X^- + AH_3Y$. The activation energy ΔE^\ddagger is decomposed into the activation strain $\Delta E_{\text{strain}}^\ddagger$ of and the stabilizing TS interaction $\Delta E_{\text{int}}^\ddagger$ between the reactants in the transition state.

The strain $\Delta E_{\text{strain}}(\zeta)$ is determined by the rigidity of the reactants and on the extent to which groups must reorganize in a particular reaction mechanism, whereas the interaction $\Delta E_{\text{int}}(\zeta)$ between the reactants depends on their electronic structure and on how they are mutually oriented as they approach each other. It is the interplay between $\Delta E_{\text{strain}}(\zeta)$ and $\Delta E_{\text{int}}(\zeta)$ that determines if and at which point along ζ a barrier arises. The activation energy of a reaction $\Delta E^\ddagger = \Delta E(\zeta^{\text{TS}})$ consists of the activation strain $\Delta E_{\text{strain}}^\ddagger = \Delta E_{\text{strain}}(\zeta^{\text{TS}})$ plus the TS interaction $\Delta E_{\text{int}}^\ddagger = \Delta E_{\text{int}}(\zeta^{\text{TS}})$:

$$\Delta E^\ddagger = \Delta E_{\text{strain}}^\ddagger + \Delta E_{\text{int}}^\ddagger \quad (2.9)$$

The interaction $\Delta E_{\text{int}}(\zeta)$ between the strained reactants is further analyzed in the conceptual framework provided by the Kohn-Sham molecular orbital (KS-MO) model.^{12,13} To this end, it is further decomposed into three physically meaningful terms:

$$\Delta E_{\text{int}}(\zeta) = \Delta V_{\text{elstat}} + \Delta E_{\text{Pauli}} + \Delta E_{\text{oi}} \quad (2.10)$$

The term ΔV_{elstat} corresponds to the classical electrostatic interaction between the unperturbed charge distributions of the deformed reactants and is usually attractive. The Pauli repulsion ΔE_{Pauli} comprises the destabilizing interactions between occupied orbitals and is responsible for any steric repulsion (see Ref. 12 for an exhaustive discussion). The orbital interaction ΔE_{oi} accounts for charge transfer (interaction between occupied orbitals on one moiety with unoccupied orbitals on the other, including the HOMO–LUMO interactions) and polarization (empty–occupied orbital mixing on one fragment due to the presence of another fragment). Since the Kohn-Sham MO method of density functional theory in principle yields exact energies and, in practice, with the available density functionals for exchange and correlation, rather accurate energies, we have the special situation that a seemingly one-particle model in principle accounts for the bonding energies.¹²

The results obtained in the forthcoming chapters demonstrate that the Activation Strain model provides transparent explanations of trends in reactivity. In this way, it makes MO theory, which we use to further analyze and interpret the origin of these trends, catch up with the VB theory in which such trends can be nicely understood on the basis of the Curve Crossing model developed by Shaik, Hiberty and others.¹⁶

References

- 1 Cramer, C. J. *Essentials of Computational Theory: Theories and Models*; Wiley: Chichester, 2002; Jensen, F. *Introduction to Computational Chemistry*; Wiley: Chichester, 1999; Atkins, P. W.; Friedman, R. S. *Molecular Quantum Mechanics*; 4th ed.; Oxford University Press: Oxford, 2005.
- 2 Schrödinger, E. *Phys. Rev.* **1926**, 28, 1049.
- 3 Born, M.; Oppenheimer, R. *Ann. Phys. (Leipzig)* **1927**, 84, 457; Kozłowski, P. M.; Adamowicz, L. *Chem. Rev.* **1993**, 93, 2007.
- 4 Parr, R. G.; Yang, W. *Density-Functional Theory of Atoms and Molecules*; Oxford University Press: New York, 1989.
- 5 Hohenberg, P.; Kohn, W. *Phys. Rev.* **1964**, 136, B864.
- 6 Kohn, W.; Sham, L. J. *Phys. Rev.* **1965**, 140, A1133.
- 7 Handy, N. C.; Cohen, A. J. *Mol. Phys.* **2001**, 99, 403.

- 8 Lee, C.; Yang, W.; Parr, R. G. *Phys. Rev. B* **1988**, *37*, 785.
- 9 van Lenthe, E.; Baerends, E. J.; Snijders, J. G. *J. Chem. Phys.* **1994**, *101*, 9783.
- 10 Bickelhaupt, F. M. *J. Comput. Chem.* **1999**, *20*, 114; Diefenbach, A.; de Jong, G. Th.; Bickelhaupt, F. M. *J. Chem. Theory Comput.* **2005**, *1*, 286; Diefenbach, A.; Bickelhaupt, F. M. *J. Chem. Phys.* **2001**, *115*, 4030; de Jong, G. Th.; Bickelhaupt, F. M. *ChemPhysChem* **2007**, *8*, 1170.
- 11 van Zeist, W. J.; Fonseca Guerra, C.; Bickelhaupt, F. M. *J. Comput. Chem.* **2008**, *29*, 312.
- 12 Bickelhaupt, F. M.; Baerends, E. J. In *Reviews in Computational Chemistry*; Lipkowitz, K. B., Boyd, D. B., Eds.; Wiley-VCH: New York, 2000; Vol. 15, p 1-86; Baerends, E. J.; Gritsenko, O. V. *J. Phys. Chem. A* **1997**, *101*, 5383.
- 13 Ziegler, T.; Rauk, A. *Theor. Chim. Acta* **1977**, *46*, 1; Bickelhaupt, F. M.; Nibbering, N. M. M.; van Wezenbeek, E. M.; Baerends, E. J. *J. Phys. Chem.* **1992**, *96*, 4864; Bickelhaupt, F. M.; Diefenbach, A.; de Visser, S. P.; de Koning, L. J.; Nibbering, N. M. M. *J. Phys. Chem. A* **1998**, *102*, 9549; Ziegler, T.; Rauk, A. *Inorg. Chem.* **1979**, *18*, 1558; Ziegler, T.; Rauk, A. *Inorg. Chem.* **1979**, *18*, 1755.
- 14 Morokuma, K. *J. Chem. Phys.* **1971**, *55*, 1236; Kitaura, K.; Morokuma, K. *Int. J. Quantum. Chem.* **1976**, *10*, 325.
- 15 Hoffmann, R. *Angew. Chem.* **1982**, *94*, 725; *Angew. Chem. Int. Ed. Engl.* **1982**, *21*, 711.
- 16 Shaik, S. S.; Schlegel, H. B.; Wolfe, S. *Theoretical Aspects of Physical Organic Chemistry: The S_N2 Mechanism*; Wiley: New York, 1992; Shaik, S. S.; Hiberty, P. C. *The Chemist's Guide to Valence Bond Theory*; John Wiley & Sons, Inc: New Jersey, 2008.

3 *Ab Initio and DFT Benchmark Study for Nucleophilic Substitution at Carbon ($S_N2@C$) and Silicon ($S_N2@Si$)*

Adapted from

Bento, A. P.; Solà, M.; Bickelhaupt, F. M. *J. Comput. Chem.* **2005**, 26, 1497

Abstract

To obtain a set of consistent benchmark potential energy surfaces (PES) for the two archetypal nucleophilic substitution reactions of the chloride anion at carbon in chloromethane ($S_N2@C$) and at silicon in chlorosilane ($S_N2@Si$), we have explored these PESes using a hierarchical series of *ab initio* methods [HF, MP2, MP4SDQ, CCSD, CCSD(T)] in combination with a hierarchical series of six Gaussian-type basis sets, up to *g* polarization. Relative energies of stationary points are converged to within 0.01 to 0.56 kcal/mol as a function of the basis-set size. Our best estimate, at CCSD(T)/aug-cc-pVQZ, for the relative energies of the $[Cl^-, CH_3Cl]$ reactant complex, the $[Cl-CH_3-Cl]^-$ transition state and the stable $[Cl-SiH_3-Cl]^-$ transition complex is -10.42, +2.52 and -27.10 kcal/mol, respectively. Furthermore, we have investigated the performance for these reactions of four popular density functionals, namely, BP86, BLYP, B3LYP and OLYP, in combination with a large doubly polarized Slater-type basis set of triple- ζ quality (TZ2P). Best overall agreement with our CCSD(T)/aug-cc-pVQZ benchmark is obtained with OLYP and B3LYP. However, OLYP performs better for the $S_N2@C$ overall and central barriers, which it underestimates by 2.65 and 4.05 kcal/mol, respectively. The other DFT approaches underestimate these barriers by some 4.8 (B3LYP) to 9.0 kcal/mol (BLYP).

3.1. Introduction

Bimolecular nucleophilic substitution (S_N2) constitutes a class of elementary chemical reactions that play an important role in organic chemistry.^{1,2} Various theoretical³⁻¹³ and experimental¹⁴⁻¹⁶ studies have been conducted to obtain a detailed description of the potential energy surface of S_N2 reactions. The symmetric, thermoneutral S_N2 reaction between the chloride anion and chloromethane in the gas phase is generally used as the archetypal model for nucleophilic substitution (see eq 3.1):



This reaction proceeds preferentially through a backside nucleophilic attack of the chloride anion at the carbon atom ($S_N2@C$) which goes with concerted expulsion of the leaving group.⁴ Studying the $S_N2@C$ reaction in the gas phase reveals the intrinsic behavior of this process, that is, its behavior without the interference of solvent molecules. This, in turn, can also shed light on the nature of $S_N2@C$ reactions in solution, in particular the effect of the solvent, by comparing the gas-phase results with those from condensed-phase^{1,17} and microsolvation¹⁸ investigations. A well-known feature of gas-phase $S_N2@C$ reactions is their double-well potential energy surface along the reaction coordinate,¹⁶ shown in Figure 3.1, solid line. This PES is characterized by two pronounced minima, associated with the reactant and product ion–molecule complexes (RC and PC) that are interconverted through the transition state (TS) for nucleophilic substitution at carbon.

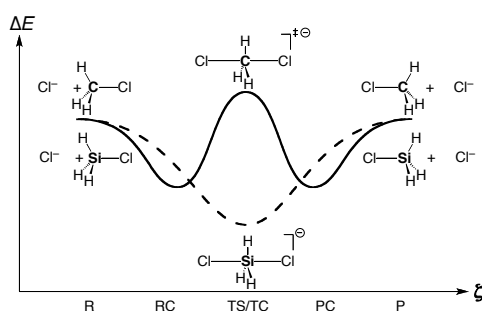


Figure 3.1. Double-well $S_N2@C$ (solid line) and single-well $S_N2@Si$ (dashed line) potential energy surfaces along the reaction coordinate ξ (R = reactants, RC = reactant complex, TS = transition state, TC = stable transition complex, PC = product complex, P = products).

Thus, whereas the $S_N2@C$ reaction has been extensively studied, much less investigations both, experimental^{19,20} and theoretical,²⁰⁻²² have been devoted to studying the nature and mechanism of gas-phase nucleophilic substitution at silicon ($S_N2@Si$). An

example of an archetypal $S_N2@Si$ reaction is the symmetric, thermoneutral reaction between the chloride anion and chlorosilane (see eq 3.2):



The structural transformation associated with the above $S_N2@Si$ substitution is equivalent to that of the $S_N2@C$ reaction of eq 3.1. Further, both reaction systems are isoelectronic. A striking difference is however that $S_N2@Si$ proceeds via a single-well PES, as shown in Figure 3.1, dashed line, that is, it proceeds without encountering a first-order saddle point on the PES along the reaction coordinate. Thus, the D_{3h} symmetric transition structure $[Cl-AH_3-Cl]^-$ turns from a transition state (TS) for $S_N2@C$ into a stable transition complex (TC) for $S_N2@Si$.

The purpose of the present study is twofold. In the first place, we wish to obtain reliable benchmarks for the PESes of the two nucleophilic substitution reactions of eqs 3.1 and 3.2. This is done by exploring these PESes with a hierarchical series of *ab initio* methods [HF, MP2, MP4SDQ, CCSD, CCSD(T)] in combination with a hierarchical series of Gaussian-type basis sets of increasing flexibility (up to quadruple- ζ + diffuse functions) and polarization (up to *g* functions). This provides the first solid benchmark for the $S_N2@Si$ reaction of $Cl^- + SiH_3Cl$. For the $S_N2@C$ reaction of $Cl^- + CH_3Cl$, authoritative benchmarks PES have been computed by Botschwina and coworkers,^{6a,b} with CCSD(T) relative energies of -10.26 and $+2.65$ kcal/mol for RC and TS relative to reactants and by Gonzales *et al.*,⁷ with CCSD(T) relative energies of -10.70 and $+2.57$ kcal/mol for RC and TS, respectively (see Table 3.1). These benchmarks PES will be confirmed and thus further consolidated in the present investigation. The main purpose of our work is however to provide a consistent set of *ab initio* PES data for accurately estimating trends associated with going from $S_N2@C$ to $S_N2@Si$ substitution.

A second purpose is to evaluate and validate the performance of four popular density functionals, BP86, BLYP, B3LYP and OLYP, for describing the above $S_N2@C$ and $S_N2@Si$ substitution reactions against our *ab initio* benchmark PESes for the two model reactions. While the *ab initio* approach turns out to be satisfactory in terms of accuracy and reliability, it is at the same time prohibitively expensive if one wishes to study more realistic model reactions involving larger nucleophiles and substrates. Thus, our survey of density functionals serves to validate one or more of these density functional theory (DFT) approaches as a computationally more efficient alternative to high-level *ab initio* theory in future investigations. A general concern associated with the application of DFT to the investigation of chemical reactions is its notorious tendency to underestimate activation energies.^{7,23-25} Thus, we arrive at a ranking of density functional approaches in terms of the accuracy with which they describe the PES of our model reaction, in

particular the activation energy. We focus on the overall activation energy, that is, the difference in energy between the TS and the separate reactants, which is decisive for the rate of chemical reactions in the gas phase, in particular, if they occur under low-pressure conditions in which the reaction system is (in good approximation) thermally isolated,^{15,26} see also Section II of Ref. 27. But we also address the central barrier, that is, the difference in energy between the TS and the reactant complex. Here, we anticipate that the (nonhybrid) functional OLYP is found to perform very satisfactorily, in fact as good as the much advocated hybrid functional B3LYP.

Table 3.1. Selected literature values for relative energies (in kcal/mol) of stationary points along the reaction coordinate for the $S_N2@C$ and $S_N2@Si$ reactions of $Cl^- + CH_3Cl$ and $Cl^- + SiH_3Cl$.

| Reaction | Method | RC | TS | Reference |
|------------------|--------------------------------------|--------|-------|-----------|
| $Cl^- + CH_3Cl$ | MP2/6-311++G(2d, p) | -10.64 | 3.05 | 11 |
| | MP2/6-31+G* | -9.66 | 7.66 | 12 |
| | MP2/6-31G** | -10.96 | 4.55 | 12 |
| | MP-SAC2/6-31G**//MP2/6-31G** | -11.04 | 4.56 | 12 |
| | G2(+) | -10.50 | 2.75 | 5 |
| | RHF/6-31+G*/RHF/6-31+G* | -8.87 | 6.60 | 8 |
| | MP2/6-31+G*/RHF/6-31+G* | -9.44 | 8.49 | 8 |
| | MP3/6-31+G*/RHF/6-31+G* | -9.46 | 9.04 | 8 |
| | MP4/6-31+G*/RHF/6-31+G* | -9.53 | 6.48 | 8 |
| | CBS-QB3//B3LYP/6-311G(2d, d, p) | -10.60 | 2.00 | 9 |
| | QCISD(T)/6-31++G(3df, 2pd) | -10.84 | 3.00 | 13 |
| | HF | | 7.65 | a |
| | MP2 | | 4.02 | a |
| | CCSD | | 5.07 | a |
| | CCSD(T) | -10.26 | 2.65 | a |
| | RHF/TZ2Pf+dif | -8.86 | 7.20 | 7 |
| | B3LYP/TZ2Pf+dif | -9.57 | -0.76 | 7 |
| | BLYP/TZ2Pf+dif | -9.70 | -4.29 | 7 |
| | BP86/TZ2Pf+dif | -9.85 | -3.66 | 7 |
| | MP2/TZ2Pf+dif | -10.62 | 3.65 | 7 |
| | CCSD/TZ2Pf+dif | -10.22 | 4.89 | 7 |
| | CCSD(T)/TZ2Pf+dif | -10.70 | 2.57 | 7 |
| $Cl^- + SiH_3Cl$ | MNDO//RHF/6-31G* | -35.20 | b | 20 |
| | RHF/6-31G* | -21.00 | b | 20 |
| | MP4/6-31++G(d, p)//MP2/6-31++G(d, p) | -22.40 | b | 22 |

*For RC: aug-cc-pVQZ(Cl), cc-pVQZ(C), (H: sp aug-cc-pVTZ, d cc-pVTZ) basis set; see Ref. 6a. For TS, aug-cc-pV5Z(Cl), cc-pV5Z(C), cc-pVQZ(H) basis set; see Ref. 6b. ^bNo first-order saddle point exists.

3.2. Methods

3.2.1. DFT Geometries and Potential Energy Surfaces

All geometry optimizations have been done with DFT²⁸ using the Amsterdam Density Functional (ADF) program.^{29,30} The performance for computing the geometries and relative energies of the stationary points along the PESes of our model reactions (see

Figure 3.1) was compared for the following density functionals: BP86,^{31,32} BLYP^{31,33} and OLYP.^{33,34} They were used in combination with the TZ2P basis set, which is a large uncontracted set of Slater-type orbitals (STOs) containing diffuse functions, which is of triple- ζ quality and has been augmented with two sets of polarization functions: $2p$ and $3d$ on hydrogen, $3d$ and $4f$ on carbon, silicon and chlorine. The core shells of carbon ($1s$), silicon ($1s2s2p$) and chlorine ($1s2s2p$) were treated by the frozen-core approximation.³⁰ An auxiliary set of s , p , d , f and g STOs was used to fit the molecular density and to represent the Coulomb and exchange potentials accurately in each SCF cycle. The importance of relativistic effects was investigated in case of the OLYP functional using the zeroth-order regular approximation,³⁵ i.e., at ZORA-OLYP. Relativistic effects were found to be negligible. For each of the four approaches, i.e., BP86, BLYP, OLYP and ZORA-OLYP, all stationary points were confirmed to be equilibrium structures (no imaginary frequencies) or a transition state (one imaginary frequency) through vibrational analysis. In addition, based on both BLYP/TZ2P and OLYP/TZ2P geometries, we have computed the relative energies of stationary points along the PES for the B3LYP hybrid functional.^{33,36} For technical reasons, our B3LYP/TZ2P energies are computed in a post-SCF manner, that is, using the electron density obtained at BLYP/TZ2P. Recently, we have extensively tested this approximation and have shown that it introduces an error in the computed B3LYP energies of a few tenths of a kcal/mol.³⁷

3.2.2. *Ab Initio* Potential Energy Surfaces

Based on the ZORA-OLYP/TZ2P geometries, energies of the stationary points were computed in a series of single-point calculations with the program package Gaussian³⁸ using the following hierarchy of quantum chemical methods: Hartree-Fock (HF), Møller-Plesset perturbation theory³⁹ through second order (MP2) and fourth order with omission of the triple substitutions (MP4SDQ),⁴⁰ and coupled-cluster theory⁴¹ with single and double excitations (CCSD)⁴² and with triple excitations treated perturbatively [CCSD(T)].⁴³ At each level of theory, a hierarchical series of 6 Gaussian-type basis sets was used: Pople's 6-31+G*, 6-31++G**, 6-311++G** basis sets, and Dunning's⁴⁴ augmented correlation consistent polarized valence basis sets of double-, triple-, and quadruple- ζ quality, i.e., aug-cc-pVDZ, aug-cc-pVTZ and aug-cc-pVQZ.

3.3. Results and Discussion

3.3.1. Geometries of Stationary Points

First, we examine the geometries of stationary points along the reaction coordinate of the $S_N2@C$ reaction of $Cl^- + CH_3Cl$ and the $S_N2@Si$ reaction of $Cl^- + SiH_3Cl$, computed with the GGA functionals BP86, BLYP, OLYP and ZORA-OLYP in combination with the TZ2P basis set. The computed geometry parameters are defined and their values collected in Figure 3.2 (see also Figure 3.1). For each of the functionals, the $S_N2@C$ reaction proceeds, not unexpectedly, from the reactants via formation of a stable C_{3v} symmetric reactant complex (RC), in which Cl^- sticks in an η^3 fashion to the three hydrogen atoms of chloromethane, followed by the D_{3h} symmetric transition state (TS). The latter leads to the product complex (PC) and finally the products (P), which in this thermoneutral automerization are equivalent to RC and R, respectively. On the other hand, the $S_N2@Si$ reaction proceeds from the reactants directly, without a barrier to a D_{3h} symmetric TC, i.e., a stable pentavalent silicate intermediate, which corresponds structurally and is isoelectronic with the TS of the $S_N2@C$ reaction. From this TC the products, which are equivalent to the reactants, are reached without the occurrence of a reverse barrier. These results agree well with earlier experimental and theoretical work (see Section 3.1). All species have been verified through a vibrational analysis to represent equilibrium structures (no imaginary frequencies) or a transition state (one imaginary frequency, only in the case of $S_N2@C$). The imaginary frequency in the $S_N2@C$ transition state, associated with the normal mode that connects RC and PC, varies, depending on the functional, between 282 and 356 cm^{-1} (for BP86, BLYP, OLYP and ZORA-OLYP it amounts to 316, 282, 356 and 354 cm^{-1}).

The geometries obtained with the various density functionals (BP86, BLYP, OLYP) do not show significant mutual discrepancies, and they agree reasonably well with gas-phase experimental values^{45,46} obtained through microwave (MW) spectroscopy (compare Figure 3.2 and Table 3.2). The C–H and Si–H bond distance values are very robust with respect to changing the functional, with variations in the order of a few thousandths of an Å (Figure 3.2). The same holds for H–C–Cl and H–Si–Cl (or H–C–H and H–Si–H) angles, which typically vary by a few tenths of a degree; only in the case of the RC of $Cl^- + CH_3Cl$ they vary up to ca. 1°. Variations in the length of the C–Cl and Si–Cl bonds, in the substrate and TS, are in the order of a few hundredths of an Å. Relativistic effects on geometry parameters are virtually negligible (compare OLYP and ZORA-OLYP in Figure 3.2): bond distances values change by 0.001 Å or less and bond angles change by 0.1° or less. Comparison with MW experiments for CH_3Cl and SiH_3Cl (Table 3.2) furthermore shows that all three density functionals somewhat overestimate bond distan-

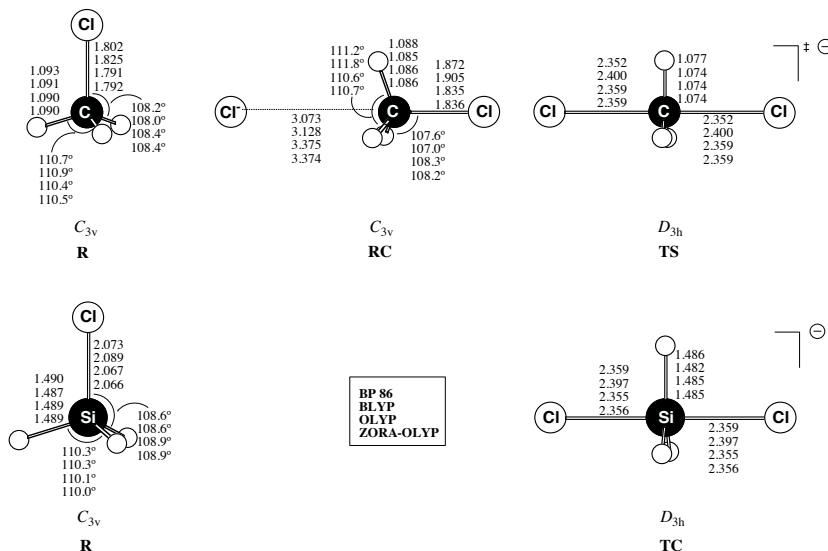


Figure 3.2. Geometries (in Å, deg.) of stationary points along the potential energy surfaces for the $S_N2@C$ and $S_N2@Si$ substitution of $Cl^- + CH_3Cl$ and $Cl^- + SiH_3Cl$, respectively, optimized at BP86, BLYP, OLYP and ZORA-OLYP in combination with the TZ2P basis set.

ces, by up to 0.003 (C–H), 0.008 (Si–H), 0.04 (C–Cl) and 0.041 Å (Si–Cl), whereas bond angles agree within 1° for all methods. OLYP (or ZORA-OLYP) performs overall slightly better than the other functionals with bond-length overestimations of 0 (C–H), 0.008 (Si–H), 0.007 (C–Cl) and 0.018 Å (Si–Cl). Likewise, OLYP (or ZORA-OLYP) compares slightly better than the other functionals with CCSD(T) geometries^{6a,b} for CH_3Cl (C–H and C–Cl are 1.0853 and 1.7821 Å at CCSD(T), which is close to the MW experimental values, see Table 3.2) and for the TS of the $S_N2@C$ reaction [C–H and C–Cl are 1.0704 and 2.3071 Å at CCSD(T)].

Table 3.2. Experimental geometries (in Å, deg) of CH_3Cl and SiH_3Cl .

| Molecule | Method | R(A–Cl) | R(A–H) | ∠CIAH | ∠HAH | Ref. |
|---------------------|--------|---------|--------|-------|-------|------|
| CH ₃ Cl | MW | 1.778 | 1.086 | 108.2 | 110.7 | 46 |
| | MW, IR | 1.785 | 1.090 | | 110.8 | 45 |
| SiH ₃ Cl | MW | 2.048 | 1.482 | 107.9 | 111.0 | 46 |
| | MW, IR | 2.048 | 1.481 | 108.0 | | 45 |

3.3.2. *Ab Initio* Benchmark Potential Energy Surfaces

The various functionals thus yield essentially the same geometries. Later on, in the section hereafter, we show that OLYP also performs excellently in terms of relative energies of stationary points. Based on these findings, and the fact that OLYP is numerically robust and agrees slightly better with available experimental and CCSD(T)

geometries, we choose the geometries of this functional, i.e., ZORA-OLYP/TZ2P, to compute the *ab initio* benchmark potential energy surfaces, which are summarized as relative energies in Table 3.3.

The energy of the $S_N2@C$ reactant complex computed with our best basis set (aug-cc-pVQZ) varies relatively little along the range of methods, i.e., from -8.77 to -10.30 to -10.02 to -10.00 to -10.42 kcal/mol for HF, MP2, MP4SDQ, CCSD and CCSD(T), and the three highest-level values are equal to each other within less than half a kcal/mol, see Table 3.3. At variance, the energy of the $S_N2@C$ transition state depends more delicately on the level at which correlation is treated. This TS energy computed again with our best basis set (aug-cc-pVQZ) varies from 7.44 to 4.34 to 4.80 to 4.89 to 2.52 kcal/mol along HF, MP2, MP4SDQ, CCSD and CCSD(T), see Table 3.3. Thus, not unexpectedly, HF significantly overestimates the barrier, which is significantly lowered by the incorporation of Coulomb correlation into theoretical treatment. Note that for the TS the three highest-level values are distributed over a range of 2.37 kcal/mol. Furthermore, the CCSD(T) values are converged as a function of the basis-set size (at aug-cc-pVQZ) to within a few hundredths of a kcal/mol for the RC and to about half a kcal/mol for the TS. In Chapter 4, we have applied CBS extrapolations to hierarchical series for similar reactions (S_N2 and E2), which yield, in all cases, values for barriers that differ less than a few tenths of a kcal/mol from the direct, i.e., unextrapolated, value at the best level of theory. Thus, our best estimates at CCSD(T) of -10.42 and $+2.52$ kcal/mol for the RC and TS of the $S_N2@C$ reaction agree excellently with and further consolidate the corresponding CCSD(T) benchmarks values of -10.26 and $+2.65$ kcal/mol computed by Botschwina and coworkers^{6a,b} and of -10.70 and $+2.57$ kcal/mol computed by Gonzales *et al.*⁷

The energy of the stable $S_N2@Si$ transition complex shows a similar behavior as that of the $S_N2@C$ transition state in the sense that it also delicately depends on the level at which correlation is treated. The energy of this TC computed with our best basis set (aug-cc-pVQZ) varies from -18.08 to -27.64 to -25.87 to -25.71 to -27.10 kcal/mol along HF, MP2, MP4SDQ, CCSD and CCSD(T), see Table 3.3. Note how HF dramatically underestimates the stability of the TC, i.e., by 9 kcal/mol! The three highest-level values are within a range of 1.39 kcal/mol. Furthermore, the CCSD(T) values for the stable TC are converged as a function of the basis-set size (at aug-cc-pVQZ) to within 0.01 kcal/mol. Thus, our best estimate at CCSD(T) of -27.10 kcal/mol for the TC of the $S_N2@Si$ reaction is 4.7 kcal/mol more bonding than the best value of -22.4 kcal/mol obtained previously by Gordon and coworkers²² at MP4/6-31++G(d,p)//MP2/6-31++G(d,p). Note that the latter value closely agrees with our MP4SDQ/6-31++G**//OLYP/TZ2P value of -21.46 kcal/mol. We conclude that the pentavalent silicate

intermediate (i.e., TC) displays the same strong correlation phenomena, associated with 3-center–4-electron bonding,^{10,25} as the transition state of the $S_N2@C$ reaction.

Table 3.3. Relative energies (in kcal/mol) of stationary points along the reaction coordinate for the $S_N2@C$ and $S_N2@Si$ reactions of $Cl^- + CH_3Cl$ and $Cl^- + SiH_3Cl$, computed at several levels of *ab initio*.

| Method | | CH ₃ Cl + Cl [−] | | SiH ₃ Cl + Cl [−] |
|---------|-------------|--------------------------------------|------|---------------------------------------|
| | | RC | TS | TC |
| HF | 6-31+G* | −8.83 | 6.77 | −17.41 |
| | 6-31++G** | −8.92 | 6.65 | −17.33 |
| | 6-311++G** | −9.13 | 7.05 | −18.05 |
| | aug-cc-pVDZ | −9.32 | 5.23 | −19.69 |
| | aug-cc-pVTZ | −8.89 | 6.94 | −18.40 |
| | aug-cc-pVQZ | −8.77 | 7.44 | −18.08 |
| MP2 | 6-31+G* | −9.39 | 7.87 | −21.70 |
| | 6-31++G** | −9.42 | 7.91 | −22.15 |
| | 6-311++G** | −9.66 | 8.43 | −24.06 |
| | aug-cc-pVDZ | −10.78 | 2.54 | −27.27 |
| | aug-cc-pVTZ | −10.36 | 3.88 | −27.67 |
| | aug-cc-pVQZ | −10.30 | 4.34 | −27.64 |
| MP4SDQ | 6-31+G* | −9.37 | 7.48 | −21.01 |
| | 6-31++G** | −9.40 | 7.42 | −21.46 |
| | 6-311++G** | −9.64 | 8.01 | −23.35 |
| | aug-cc-pVDZ | −10.58 | 2.71 | −25.98 |
| | aug-cc-pVTZ | −10.07 | 4.31 | −25.98 |
| | aug-cc-pVQZ | −10.02 | 4.80 | −25.87 |
| CCSD | 6-31+G* | −9.35 | 7.40 | −20.89 |
| | 6-31++G** | −9.39 | 7.26 | −21.35 |
| | 6-311++G** | −9.66 | 7.73 | −23.23 |
| | aug-cc-pVDZ | −10.57 | 2.66 | −25.84 |
| | aug-cc-pVTZ | −10.06 | 4.34 | −25.82 |
| | aug-cc-pVQZ | −10.00 | 4.89 | −25.71 |
| CCSD(T) | 6-31+G* | −9.54 | 5.80 | −21.29 |
| | 6-31++G** | −9.59 | 5.62 | −21.80 |
| | 6-311++G** | −9.88 | 5.93 | −23.83 |
| | aug-cc-pVDZ | −10.95 | 0.54 | −26.80 |
| | aug-cc-pVTZ | −10.48 | 1.96 | −27.11 |
| | aug-cc-pVQZ | −10.42 | 2.52 | −27.10 |

3.3.3. Validation of DFT Potential Energy Surfaces

Next, we examine the relative energies of stationary points computed with the density functionals BP86, BLYP, OLYP, ZORA-OLYP and B3LYP in combination with the TZ2P basis set. Note that for all density functionals but B3LYP we use consistently the geometries optimized with that functional, for example, OLYP//OLYP. In the case of B3LYP, we have carried out single-point computations using both the BLYP and the OLYP geometries. First, we focus on the overall activation energy, that is, the difference

in energy between the TS and the separate reactants. This barrier, as pointed out in the introduction, is decisive for the rate of chemical reactions in the gas phase, in particular, if they occur under low-pressure conditions.^{15,26,27} The central barrier, that is, the difference in energy between the TS and the reactant complex is discussed thereafter. The DFT relative energies are collected in Table 3.4. The performance of the various density functional approaches is assessed by a systematic comparison of the resulting potential energy surfaces with our CCSD(T)/aug-cc-pVQZ benchmark values (see Table 3.3).

It is clear from the data in Table 3.4 that OLYP outperforms both BP86 and BLYP and, furthermore, that it performs similarly well as the much advocated B3LYP hybrid functional. The mean absolute errors (MAE) in energies of stationary points relative to reactants for OLYP (2.2 kcal/mol) and B3LYP (2.3 – 2.5 kcal/mol) are equal within a few tenths of a kcal/mol and clearly smaller than those of BP86 (3.4 kcal/mol). Note that these MAE values are merely to be used as a rough indicator of overall performance for relative energies of the stationary points (i.e., RC and TS for $S_N2@C$, and TC for $S_N2@Si$), which need to be inspected individually. OLYP performs particularly well for the overall activation energy (i.e., TS relative to R) of the $S_N2@C$ reaction, which it underestimates by only 2.65 kcal/mol compared to an underestimation of 4.7 to 4.9 kcal/mol for B3LYP and of ca. 8 – 9 kcal/mol for BP86 and BLYP. Relativistic effects on the OLYP energies are negligible, that is, one-tenth of a kcal/mol or less. Note also that the effect of using either BLYP or OLYP geometries for the computation of B3LYP energies is 0.3 kcal/mol at most (namely for the $S_N2@C$ central barrier, i.e., TS relative to RC) and even much less for all other relative energies. Thus, the OLYP potential energy surfaces for $S_N2@C$ (–9.0 and –0.1 kcal/mol for RC and TS relative to R) and $S_N2@Si$ (–24.4 kcal/mol for TC relative to R) appears to be as good as that of B3LYP

Table 3.4. Relative energies (in kcal/mol) of stationary points along the reaction coordinate for the $S_N2@C$ and $S_N2@Si$ reactions of $Cl^- + CH_3Cl$ and $Cl^- + SiH_3Cl$, computed at several levels of density functional theory.^a

| Method | $Cl^- + CH_3Cl$ | | | | $Cl^- + SiH_3Cl$ | | |
|-------------|-----------------|-------|--------------------------|---------------------------|------------------|-------------------------|--------------------------|
| | RC | TS | (Err. in Barr. | (Err. in Barr. | TC | (Mean Abs. Err. | (Mean Abs. Err. |
| | | | Rel. to R ^b) | Rel. to RC ^b) | | Rel to R ^b) | Rel to RC ^b) |
| BP86 | –10.98 | –5.32 | (–7.84) | (–7.28) | –28.75 | (3.35) | (3.16) |
| BLYP | –11.19 | –6.46 | (–8.98) | (–8.21) | –25.92 | (3.64) | (3.39) |
| OLYP | –9.02 | –0.13 | (–2.65) | (–4.05) | –24.42 | (2.24) | (2.71) |
| ZORA-OLYP | –8.99 | –0.22 | (–2.74) | (–4.17) | –24.36 | (2.30) | (2.78) |
| B3LYP//BLYP | –10.07 | –2.17 | (–4.69) | (–5.04) | –25.29 | (2.28) | (2.40) |
| B3LYP//OLYP | –9.93 | –2.35 | (–4.87) | (–5.36) | –25.11 | (2.45) | (2.61) |

^aComputed with TZ2P basis set (see methodological section). Geometries (see Figure 3.2) and energies computed at the same level of theory, unless indicated otherwise. ^bError in Overall Barrier (TS relative to R) and Central Barrier (TS relative to RC) and mean absolute error for the energies of the two stationary points of $Cl^- + CH_3Cl$ (i.e., RC and TS) plus that of $Cl^- + SiH_3Cl$ (i.e., TC) both relative to R and relative to RC, compared with the CCSD(T)/aug-cc-pVQZ benchmark values from this work (see Table 3.3).

and both compare reasonably well (although not perfect) with the *ab initio* benchmark PES. This agrees with the work of Baker and Pulay for other organic reactions.²⁴

Finally, we address the central barrier, that is, the difference in energy between the TS and the reactant complex, which becomes decisive in the high-pressure regime, when termolecular collisions are sufficiently efficient to cool the otherwise rovibrationally hot reactant complex, causing it to be in thermal equilibrium with the environment.^{15,26,27} Also for the central barrier of the $S_N2@C$ reaction, OLYP outperforms both BP86 and BLYP and it performs also slightly better than the much advocated B3LYP hybrid functional. Thus, OLYP underestimates this central activation energy (i.e., TS relative to RC) by 4.1 kcal/mol compared to an underestimation of 5.0 to 5.4 kcal/mol for B3LYP and of ca. 7 – 8 kcal/mol for BP86 and BLYP. On the other hand, if one examines the overall performance in terms of the mean absolute error in energies of stationary points *relative to the reactant complex*, it is B3LYP (with an error of 2.4 – 2.6 kcal/mol) that is slightly better than OLYP (with an error of 2.7 – 2.8 kcal/mol). All together, we conclude that both OLYP and B3LYP are reasonable approaches for tackling the $S_N2@C$ and $S_N2@Si$ reactions.

3.4. Conclusions

We have computed *ab initio* benchmarks for the archetypal nucleophilic substitution of chloride at chloromethane carbon ($S_N2@C$) and chlorosilane silicon ($S_N2@Si$) and, thus, for the trend from $S_N2@C$ to $S_N2@Si$. These benchmarks derive from a hierarchical series of methods up to CCSD(T)/aug-cc-pVQZ, which is converged with respect to the basis-set size within a few tenths of a kcal/mol. Previous benchmarks for the $S_N2@C$ reaction,^{6,7} in particular the activation energy, are confirmed and thus further consolidated. The previous best *ab initio* estimate of the stability of the D_{3h} symmetric transition complex (TC) occurring in the $S_N2@Si$ reaction is shown to be too weakly bonding by ca. 5 kcal/mol.

This benchmark is used to evaluate the performance of four popular density functionals, BP86, BLYP, B3LYP and OLYP, for describing the above $S_N2@C$ and $S_N2@Si$ substitution reactions. Relativistic effects (ZORA) are shown to be negligible. Interestingly, the relatively new OLYP functional, which features Handy's improved exchange functional OPTX,³⁴ performs satisfactorily with a mean absolute error of 2.2 and 2.7 kcal/mol (in energies of stationary points of both reactions relative to reactants, R, and reactant complex, RC, respectively) and an underestimation of the overall $S_N2@C$ barrier (i.e., TS relative to R) by about two and a half kcal/mol and of the central $S_N2@C$ barrier (i.e., TS relative to RC) by 4.1 kcal/mol. The B3LYP hybrid functional too performs well with a mean absolute error of about 2.4 and 2.5 kcal/mol (in energies

relative to R and RC, respectively), an underestimation of the overall $S_N2@C$ barrier by ca. 4.8 kcal/mol and an underestimation of the central $S_N2@C$ barrier of 5.0 – 5.4 kcal/mol. Thus, OLYP/TZ2P emerges from this investigation as a sound and efficient approach for the routine investigation of trends in nucleophilic substitution reactions at carbon and silicon, also in larger, more realistic model systems.

References

- 1 Smith, M. B.; March, J. *March's Advanced Organic Chemistry: Reactions, Mechanisms, and Structure*; Wiley: New York, 2007; Carey, F. A.; Sundberg, R. J. *Advanced Organic Chemistry, Part A*; 5th ed.; Springer: New York, 2007.
- 2 Ingold, C. *Structure and Mechanism in Organic Chemistry*; 2nd ed.; Cornell University Press: Ithaca, NY, 1969.
- 3 Deng, L.; Branchadell, V.; Ziegler, T. *J. Am. Chem. Soc.* **1994**, *116*, 10645; Bickelhaupt, F. M. *J. Comput. Chem.* **1999**, *20*, 114; Gonzales, J. M.; Pak, C.; Cox, R. S.; Allen, W. D.; Schaefer III, H. F.; Császár, A. G.; Tarczay, G. *Chem. Eur. J.* **2003**, *9*, 2173; Parthiban, S.; de Oliveira, G.; Martin, J. M. L. *J. Phys. Chem. A* **2001**, *105*, 895; Chandrasekhar, J.; Smith, S. F.; Jorgensen, W. L. *J. Am. Chem. Soc.* **1985**, *107*, 154; Shaik, S. S.; Schlegel, H. B.; Wolfe, S. *Theoretical Aspects of Physical Organic Chemistry: The S_N2 Mechanism*; Wiley: New York, 1992; Laerdahl, J. K.; Uggerud, E. *Int. J. Mass Spectrom.* **2002**, *214*, 277.
- 4 Hase, W. L. *Science* **1994**, *266*, 998; Chabinye, M. L.; Craig, S. L.; Regan, C. K.; Brauman, J. I. *Science* **1998**, *279*, 1882.
- 5 Glukhovtsev, M. N.; Pross, A.; Radom, L. *J. Am. Chem. Soc.* **1995**, *117*, 2024.
- 6 (a) Schmatz, S.; Botschwina, P.; Hauschildt, J.; Schinke, R. *J. Chem. Phys.* **2001**, *114*, 5233. (b) Botschwina, P. *Theor. Chem. Acc.* **1998**, *99*, 426.
- 7 Gonzales, J. M.; Allen, W. D.; Schaefer III, H. F. *J. Phys. Chem. A* **2005**, *109*, 10613.
- 8 Harder, S.; Streitwieser, A.; Petty, J. T.; Schleyer, P. v. R. *J. Am. Chem. Soc.* **1995**, *117*, 3253.
- 9 Vayner, G.; Houk, K. N.; Jorgensen, W. L.; Brauman, J. I. *J. Am. Chem. Soc.* **2004**, *126*, 9054.
- 10 Grüning, M.; Gritsenko, O. V.; Baerends, E. J. *J. Phys. Chem. A* **2004**, *108*, 4459.
- 11 Okuno, Y. *Int. J. Quantum Chem.* **1998**, *68*, 261.
- 12 Tucker, S. C.; Truhlar, D. G. *J. Phys. Chem.* **1989**, *93*, 8138.
- 13 Lee, I.; Kim, C. K.; Sohn, C. K.; Li, H. G.; Lee, H. W. *J. Phys. Chem. A* **2002**, *106*, 1081.

- 14 Gronert, S. *Acc. Chem. Res.* **2003**, 36, 848; Gronert, S. *Chem. Rev.* **2001**, 101, 329; DePuy, C. H.; Gronert, S.; Mulin, A.; Bierbaum, V. M. *J. Am. Chem. Soc.* **1990**, 112, 8650; Graul, S. T.; Bowers, M. T. *J. Am. Chem. Soc.* **1991**, 113, 9696; Viggiano, A. A.; Morris, R. A.; Paschkewitz, J. S.; Paulson, J. F. *J. Am. Chem. Soc.* **1992**, 114, 10477; Li, C.; Ross, P.; Szulejko, J. E.; McMahon, T. B. *J. Am. Chem. Soc.* **1996**, 118, 9360; Bickelhaupt, F. M.; de Koning, L. J.; Nibbering, N. M. M.; Baerends, E. J. *J. Phys. Org. Chem.* **1992**, 5, 179; Bickelhaupt, F. M.; Buisman, G. J. H.; de Koning, L. J.; Nibbering, N. M. M.; Baerends, E. J. *J. Am. Chem. Soc.* **1995**, 117, 9889; Wladkowski, B. D.; Brauman, J. I. *J. Phys. Chem.* **1993**, 97, 13158.
- 15 Nibbering, N. M. M. *Acc. Chem. Res.* **1990**, 23, 279.
- 16 Olmstead, W. N.; Brauman, J. I. *J. Am. Chem. Soc.* **1977**, 99, 4219.
- 17 Ensing, B.; Meijer, E. J.; Blöchl, P. E.; Baerends, E. J. *J. Phys. Chem. A* **2001**, 105, 3300; Uggerud, E.; Bache-Andreassen, L. *Chem. Eur. J* **1999**, 5, 1917; Truong, T. N.; Stefanovich, E. V. *J. Phys. Chem.* **1995**, 99, 14700; Mo, Y.; Gao, J. *J. Comput. Chem.* **2000**, 21, 1458; Aleman, C.; Maseras, F.; Lledós, A.; Duran, M.; Bertran, J. *J. Phys. Org. Chem.* **1989**, 2, 611.
- 18 Mohamed, A. A.; Jensen, F. *J. Phys. Chem. A* **2001**, 105, 3259; Bickelhaupt, F. M.; Baerends, E. J.; Nibbering, N. M. M. *Chem. Eur. J.* **1996**, 2, 196; Bohme, D. K.; Raksit, A. B. *J. Am. Chem. Soc.* **1984**, 106, 3447; Bohme, D. K.; Raksit, A. B. *Can. J. Chem.* **1985**, 63, 3007; Henchman, M.; Hierl, P. M.; Paulson, J. F. *J. Am. Chem. Soc.* **1985**, 107, 2812; Hierl, P. M.; Ahrens, A. F.; Henchman, M.; Viggiano, A. A.; Paulson, J. F. *J. Am. Chem. Soc.* **1986**, 108, 3142.
- 19 Hilderbrandt, R. L.; Homer, G. D.; Boudjouk, P. *J. Am. Chem. Soc.* **1976**, 98, 7476; Sommer, L. H.; Parker, G. A.; Lloyd, N. C.; Frye, C. L.; Michael, K. W. *J. Am. Chem. Soc.* **1967**, 89, 857.
- 20 Damrauer, R.; Burggraf, L. W.; Davis, L. P.; Gordon, M. S. *J. Am. Chem. Soc.* **1988**, 110, 6601.
- 21 Gronert, S.; Glaser, R.; Streitwieser, A. *J. Am. Chem. Soc.* **1989**, 111, 3111.
- 22 Windus, T. L.; Gordon, M. S.; Davis, L. P.; Burggraf, L. W. *J. Am. Chem. Soc.* **1994**, 116, 3568.
- 23 Bach, R. D.; Glukhovtsev, M. N.; Gonzalez, C. *J. Am. Chem. Soc.* **1998**, 120, 9902; Baker, J.; Muir, M.; Andzelm, J. *J. Chem. Phys.* **1995**, 102, 2063; Barone, V.; Adamo, C. *J. Chem. Phys.* **1996**, 105, 11007; Poater, J.; Solà, M.; Duran, M.; Robles, J. *J. Phys. Chem. Chem. Phys.* **2002**, 4, 722; Thümmel, H. T.; Bauschlicher, C. W. *J. Phys. Chem. A* **1997**, 101, 1188; Diefenbach, A.; Bickelhaupt, F. M. *J. Chem. Phys.* **2001**, 115, 4030; Gonzales, J. M.; Cox III, S.; Brown, S. T.; Allen, W. D.; Schaefer III, H. F. *J. Phys. Chem. A* **2001**, 105, 11327.
- 24 Baker, J.; Pulay, P. *J. Chem. Phys.* **2002**, 117, 1441.

- 25 Gritsenko, O. V.; Ensing, B.; Schipper, P. R. T.; Baerends, E. J. *J. Phys. Chem. A* **2000**, *104*, 8558.
- 26 Nibbering, N. M. M. *Adv. Phys. Org. Chem.* **1988**, *24*, 1.
- 27 Bickelhaupt, F. M. *Mass Spectrom. Rev.* **2001**, *20*, 347.
- 28 Parr, R. G.; Yang, W. *Density-Functional Theory of Atoms and Molecules*; Oxford University Press: New York, 1989; Ziegler, T. *Can. J. Chem.* **1995**, *73*, 743; Ziegler, T. *Chem. Rev.* **1991**, *91*, 651; Bickelhaupt, F. M.; Baerends, E. J. In *Reviews in Computational Chemistry*; Lipkowitz, K. B., Boyd, D. B., Eds.; Wiley-VCH: New York, 2000; Vol. 15, p 1-86.
- 29 Baerends, E. J.; Autschbach, J.; Bérces, A.; Berger, J. A.; Bickelhaupt, F. M.; Bo, C.; de Boeij, P. L.; Boerrigter, P. M.; Cavallo, L.; Chong, D. P.; Deng, L.; Dickson, R. M.; Ellis, D. E.; van Faassen, M.; Fan, L.; Fischer, T. H.; Fonseca Guerra, C.; van Gisbergen, S. J. A.; Groeneveld, J. A.; Gritsenko, O. V.; Grüning, M.; Harris, F. E.; van den Hoek, P.; Jacob, C. R.; Jacobsen, H.; Jensen, L.; Kadantsev, E. S.; van Kessel, G.; Klooster, R.; Kootstra, F.; van Lenthe, E.; McCormack, D. A.; Michalak, A.; Neugebauer, J.; Nicu, V. P.; Osinga, V. P.; Patchkovskii, S.; Philipsen, P. H. T.; Post, D.; Pye, C. C.; Ravenek, W.; Romaniello, P.; Ros, P.; Schipper, P. R. T.; Schreckenbach, G.; Snijders, J.; Solà, M.; Swart, M.; Swerhone, D.; te Velde, G.; Vernooijs, P.; Versluis, L.; Visscher, L.; Visser, O.; Wang, F.; Wesolowski, T. A.; Van Wezenbeek, E. M.; Wiesenekker, G.; Wolff, S. K.; Woo, T. K.; Yakovlev, A. L.; Ziegler, T.; *ADF2002.03*, SCM: Amsterdam, The Netherlands; Fonseca Guerra, C.; Snijders, J. G.; te Velde, G.; Baerends, E. J. *Theor. Chem. Acc.* **1998**, *99*, 391; te Velde, G.; Bickelhaupt, F. M.; Baerends, E. J.; Fonseca Guerra, C.; van Gisbergen, S. J. A.; Snijders, J. G.; Ziegler, T. *J. Comput. Chem.* **2001**, *22*, 931.
- 30 Baerends, E. J.; Ellis, D. E.; Ros, P. *Chem. Phys.* **1973**, *2*, 41.
- 31 Becke, A. D. *Phys. Rev. A* **1988**, *38*, 3098.
- 32 Perdew, J. P. *Phys. Rev. B* **1986**, *33*, 8822.
- 33 Lee, C.; Yang, W.; Parr, R. G. *Phys. Rev. B* **1988**, *37*, 785.
- 34 Handy, N. C.; Cohen, A. J. *Mol. Phys.* **2001**, *99*, 403.
- 35 van Lenthe, E.; Baerends, E. J.; Snijders, J. G. *J. Chem. Phys.* **1994**, *101*, 9783.
- 36 Becke, A. D. *J. Chem. Phys.* **1993**, *98*, 5648.
- 37 de Jong, G. Th.; Geerke, D. P.; Diefenbach, A.; Bickelhaupt, F. M. *Chem. Phys.* **2005**, *313*, 261; de Jong, G. Th.; Geerke, D. P.; Diefenbach, A.; Solà, M.; Bickelhaupt, F. M. *J. Comput. Chem.* **2005**, *26*, 1006.
- 38 Frisch, M. J.; Trucks, G. W.; Schlegel, H. B.; Scuseria, G. E.; Robb, M. A.; Cheeseman, J. R.; Montgomery Jr., J. A.; Vreven, T.; Kudin, K. N.; Burant, J. C.; Millam, J. M.; Iyengar, S. S.; Tomasi, J.; Barone, V.; Mennucci, B.; Cossi, M.; Scalmani, G.; Rega, N.; Petersson, G. A.; Nakatsuji, H.; Hada, M.; Ehara, M.;

- Toyota, K.; Fukuda, R.; Hasegawa, J.; Ishida, M.; Nakajima, T.; Honda, Y.; Kitao, O.; Nakai, H.; Klene, M.; Li, X.; Knox, J. E.; Hratchian, H. P.; Cross, J. B.; Bakken, V.; Adamo, C.; Jaramillo, J.; Gomperts, R.; Stratmann, R. E.; Yazyev, O.; Austin, A. J.; Cammi, R.; Pomelli, C.; Ochterski, J. W.; Ayala, P. Y.; Morokuma, K.; Voth, G. A.; Salvador, P.; Dannenberg, J. J.; Zakrzewski, G.; Dapprich, S.; Daniels, A. D.; Strain, M. C.; Farkas, O.; Malick, D. K.; Rabuck, A. D.; Raghavachari, K.; Foresman, J. B.; Ortiz, J. V.; Cui, Q.; Baboul, A. G.; Clifford, S.; Cioslowski, J.; Stefanov, B. B.; Liu, G.; Liashenko, A.; Piskorz, P.; Komaromi, I.; Martin, R. L.; Fox, D. J.; Keith, T.; Al-Laham, M. A.; Peng, C. Y.; Nanayakkara, A.; Challacombe, M.; Gill, P. M. W.; Johnson, B.; Cheng, W.; Wong, M. W.; Gonzalez, C.; Pople, J. A.; *Gaussian 03*. Gaussian Inc.: Pittsburgh, 2003.
- 39 Møller, C.; Plesset, M. S. *Phys. Rev.* **1934**, 46, 618.
- 40 Krishnan, R.; Pople, J. A. *Int. J. Quantum Chem.* **1978**, 14, 91; Krishnan, R.; Frisch, M. J.; Pople, J. A. *J. Chem. Phys.* **1980**, 72, 4244.
- 41 Cizek, J. *J. Chem. Phys.* **1966**, 45, 4256.
- 42 Purvis III, G. D.; Barlett, R. J. *J. Chem. Phys.* **1982**, 76, 1910.
- 43 Raghavachari, K.; Trucks, G. W.; Pople, J. A.; Head-Gordon, M. *Chem. Phys. Lett.* **1989**, 157, 479.
- 44 Dunning Jr., T. H. *J. Chem. Phys.* **1989**, 90, 1007; Kendall, R. A.; Dunning Jr., T. H.; Harrison, R. J. *J. Chem. Phys.* **1992**, 96, 6796.
- 45 Callomon, J. H.; Hirota, E.; Kuchitsu, K.; Lafferty, W. J.; Maki, A. G.; Pote, C. S. *Strukturdaten freier mehratomiger Molekeln, Landolt-Börnstein, Neue Serie, Gruppe II: Atom- und Molekularphysik, Band 7*; Springer-Verlag: Berlin, 1976.
- 46 Harmony, M. D.; Laurie, V. W.; Kuczkowski, R. L.; Schwendeman, R. H.; Ramsay, D. A.; Lovas, F. J.; Lafferty, W. J.; Maki, A. G. *J. Phys. Chem. Ref. Data* **1979**, 8, 619.

4 *E2 and S_N2 Reactions of X⁻ + CH₃CH₂X. An Ab Initio and DFT Benchmark Study*

Adapted from

Bento, A. P.; Solà, M.; Bickelhaupt, F. M. *J. Chem. Theory Comput.* **2008**, *4*, 929

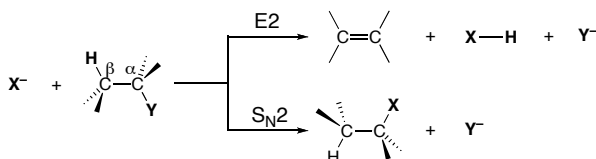
Abstract

We have computed consistent benchmark potential energy surfaces (PES) for the anti-E2, syn-E2 and S_N2 pathways of X⁻ + CH₃CH₂X with X = F, Cl. This benchmark has been used to evaluate the performance of 31 popular density functionals, covering LDA, GGA, meta-GGA and hybrid DFT. The *ab initio* benchmark has been obtained by exploring the PESes using a hierarchical series of *ab initio* methods [up to CCSD(T)] in combination with a hierarchical series of Gaussian-type basis set (up to aug-cc-pVQZ). Our best CCSD(T) estimates show that the overall barriers for the various pathways increase in the order anti-E2 (X = F) < S_N2 (X = F) < S_N2 (X = Cl) ~ syn-E2 (X = F) < anti-E2 (X = Cl) < syn-E2 (X = Cl). Thus, anti-E2 dominates for F⁻ + CH₃CH₂F and S_N2 dominates for Cl⁻ + CH₃CH₂Cl while syn-E2 is in all cases the least favorable pathway. Best overall agreement with our *ab initio* benchmark is obtained by representatives from each of the three categories of functionals, GGA, meta-GGA and hybrid DFT, with mean absolute errors in, e.g., central barriers of 4.3 (OPBE), 2.2 (M06-L) and 2.0 kcal/mol (M06), respectively. Importantly, the hybrid functional BHandH and the meta-GGA M06-L yield incorrect trends and qualitative features of the PESes (in particular, an erroneous preference for S_N2 over the anti-E2 in the case of F⁻ + CH₃CH₂F) even though they are among the best functionals as measured by their small mean absolute errors of 3.3 and 2.2 kcal/mol in reaction barriers. OLYP and B3LYP have somewhat higher mean absolute errors in central barriers (5.6 and 4.8 kcal/mol, respectively) but the error distribution is somewhat more uniform and, as a consequence, the correct trends are reproduced.

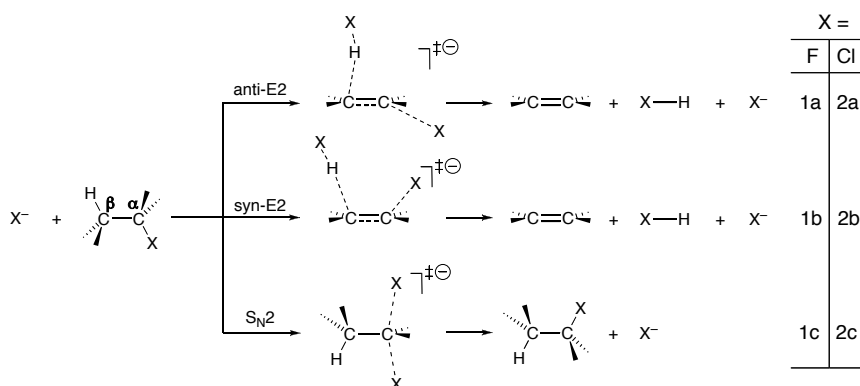
4.1. Introduction

Base-induced elimination (E2) and nucleophilic substitution (S_N2) constitute two fundamental types of chemical reactions that play an important role in organic synthesis.¹ E2 elimination is, in principle, always in competition with S_N2 substitution and the two pathways may occur as unwanted side reactions of each other (see Scheme 4.1). Gas-phase experiments have enabled the study of the intrinsic reactivity of reaction systems without the interference of solvent molecules. The resulting insights, in turn, can also shed light on the nature of the E2 and S_N2 reactions in solution, in particular the effect of the solvent, by comparing the gas-phase^{2,3} results with those of condensed-phase⁴ experiments. The various experimental investigations have over the years been augmented by an increasing number of theoretical studies, which provide a detailed description of the stationary points and the potential energy surfaces (PESes) that determine the feasibility of the various competing E2 and S_N2 reaction channels.⁵⁻⁷

Scheme 4.1. E2 and S_N2 reactions.



The purpose of the present study is twofold. First, we wish to obtain reliable benchmarks for the PESes of the E2 and S_N2 reactions of $F^- + CH_3CH_2F$ as well as $Cl^- + CH_3CH_2Cl$ (see reactions 1 and 2 in Scheme 4.2). Note that E2 eliminations can in principle proceed via two stereochemical different pathways, namely, with the base and the β -proton anti-(anti-E2) and syn-periplanar (syn-E2) with respect to the leaving group (compare reactions a and b, respectively, in Scheme 4.2). This is done by exploring for both reaction systems the PESes of each of the three reaction mechanisms with a hierarchical series of *ab initio* methods [HF, MP2, MP4, CCSD, CCSD(T)] in combination with a hierarchical series of Gaussian-type basis sets of increasing flexibility [up to quadruple- ζ + diffuse functions for reactions involving F and up to (triple + d)- ζ + diffuse functions for reactions involving Cl]. Our purpose is to provide a consistent set of *ab initio* PES data for accurately estimating trends associated with going from $F^- + CH_3CH_2F$ to $Cl^- + CH_3CH_2Cl$ as well as along anti-E2, syn-E2 and S_N2 pathways.

Scheme 4.2. E2 and S_N2 pathways for X⁻ + CH₃CH₂X.

A second purpose is to evaluate and validate the performance of several popular density functionals for describing the above elimination and nucleophilic substitution reactions (see Scheme 4.2) against our *ab initio* benchmark PESes for the six model reactions. Although the *ab initio* approach is satisfactory in terms of accuracy and reliability, it is at the same time prohibitively expensive if one wishes to study more realistic model reactions involving larger nucleophiles and substrates. Thus, a survey of density functionals serves to validate one or more of these density functional theory (DFT) approaches as a computationally more efficient alternative to high-level *ab initio* theory in future investigations. A general concern associated with the application of DFT to the investigation of chemical reactions is its notorious tendency to underestimate activation energies.^{8,9} Thus, we arrive at a ranking of density functional approaches in terms of the accuracy with which they describe the PES of our model reaction, in particular, the activation energy. We focus on the overall activation energy, that is, the difference in energy between the TS and the separate reactants,¹⁰ as well as the central barrier, that is, the difference in energy between the TS and the reactant complex. Previous studies have shown that S_N2 reaction profiles obtained with OLYP and B3LYP agree satisfactorily with highly correlated *ab initio* benchmarks.^{9,11-14} Merrill *et al.*⁶ have shown that B3LYP in combination with the aug-cc-pVDZ basis set performs reasonably well for the E2 and S_N2 reactions of F⁻ + CH₃CH₂F with deviations from G2+ of up to 3.5 kcal/mol but that it fails in locating the transition state associated with the anti-E2 elimination. Guner *et al.*¹³ have also shown that OLYP and O3LYP give comparable results to B3LYP and that these functionals work well for organic reactions. More recently, Truhlar and coworker¹⁴ have carried out an exhaustive performance analysis of various density functionals for describing barrier heights which shows that, for closed-shell S_N2 reactions, M06 and M06-2X perform best, followed by PBEh and M05-2X. B3LYP is also found to work reasonably well.

4.2. Methods

4.2.1. DFT Geometries and Potential Energy Surfaces

All DFT calculations were done with the Amsterdam Density Functional (ADF) program developed by Baerends and others.^{15,16} Geometry optimizations have been carried out with the OLYP^{17,18} density functional which yields robust and accurate geometries.¹¹ This density functional was used in combination with the TZ2P basis set, in which the molecular orbital (MOs) were expanded in a large uncontracted set of Slater-type orbitals (STOs) containing diffuse functions, and is of triple- ζ quality being augmented with two sets of polarization functions: 2p and 3d on hydrogen, 3d and 4f on carbon, fluorine and chlorine. The core shells of carbon (1s), fluorine (1s) and chlorine (1s2s2p) were treated by the frozen-core approximation.¹⁶ An auxiliary set of s, p, d, f and g STOs was used to fit the molecular density and to represent the Coulomb and exchange potentials accurately in each SCF cycle. All stationary points were confirmed to be equilibrium structures (no imaginary frequencies) or a transition state¹⁹ (one imaginary frequency) through vibrational analysis.²⁰ Furthermore, transition states were verified to connect the reactant and product complexes by carrying out intrinsic reaction coordinate (IRC) calculations.

In addition, based on OLYP/TZ2P geometries, we have computed the relative energies of stationary points along the PES for several density functionals: the LDA functional VWN,²¹ the GGA functionals BP86,^{22,23} BLYP,^{18,22} PW91,²⁴ PBE,²⁵ RPBE,²⁶ revPBE,²⁷ FT97,²⁸ HCTH/93,²⁹ HCTH/120,³⁰ HCTH/147,³⁰ HCTH/407,³¹ BOP^{22,32} and OPBE,^{17,25} the meta-GGA functionals PKZB,³³ VS98,³⁴ BLAP3,³⁵ OLAP3,^{17,35} TPSS,³⁶ M06-L,³⁷ and the hybrid functionals B3LYP,^{18,38} O3LYP,³⁹ KMLYP,⁴⁰ BHandH,⁴¹ mPBE0KCIS,⁴² mPW1K,⁴³ M05,⁴⁴ M05-2X,⁴⁵ M06^{14,46} and M06-2X.^{14,46} For technical reasons (i.e., frozen-core approximation and potentials in ADF are not available for all functionals), the energies obtained with these functionals were computed with an *all-electron* TZ2P basis set (ae-TZ2P) and in a post-SCF manner, that is, using the electron density obtained at OLYP/ae-TZ2P. This approximation has been extensively tested and has been shown to introduce an error in the computed energies of only a few tenths of a kcal/mol.⁴⁷

4.2.2. *Ab Initio* Potential Energy Surfaces

Based on the OLYP/TZ2P geometries, energies of the stationary points were computed in a series of single-point calculations with the program package Gaussian⁴⁸ using the following hierarchy of quantum chemical methods: Hartree-Fock (HF), Møller-Plesset perturbation theory⁴⁹ through the second order (MP2) and fourth order (MP4),⁵⁰ and

couple-cluster theory⁵¹ with single and double excitations (CCSD)⁵² and triple excitations treated perturbatively [CCSD(T)].⁵³ At each level of theory, we used Dunning's⁵⁴ augmented correlation consistent polarized valence basis sets of double-, triple-, and quadruple- ζ quality, that is, aug-cc-pVDZ, aug-cc-pVTZ and aug-cc-pVQZ for the reactions involving F, and the modified second-row basis sets aug-cc-pV(D + d)Z and aug-cc-pV(T + d)Z for the reactions involving Cl (limitations of our computational resources prevented us from carrying out calculations with the aug-cc-pV(Q + d)Z basis set for the latter reactions). Furthermore, using equation 7 of Ref. 55, we have extrapolated the CCSD(T) energies to the complete basis set (CBS) values CBS-23 (i.e., based on aug-cc-pVDZ and aug-cc-pVTZ values for reactions involving F, and aug-cc-pV(D + d)Z and aug-cc-pV(T + d)Z values for reactions involving Cl) and CBS-34 (i.e., based on aug-cc-pVTZ and aug-cc-pVQZ values, only for the reactions involving F).

4.3. Results and Discussion

4.3.1. Geometries of Stationary Points and Reaction Paths

First, we examine the geometries of stationary points along the reaction coordinate of anti-E2, syn-E2 and S_N2 reactions of $F^- + CH_3CH_2F$ and $Cl^- + CH_3CH_2Cl$. Previous studies have shown that the GGA functional OLYP is numerically robust and agrees well with available experimental and CCSD(T) geometries.¹¹ Therefore, we choose OLYP in combination with the TZ2P basis set, to compute the geometries of the stationary points

of our model reactions 1 and 2 (see Scheme 4.2). The resulting geometry parameters are collected in Figures 4.1 and 4.2, respectively.

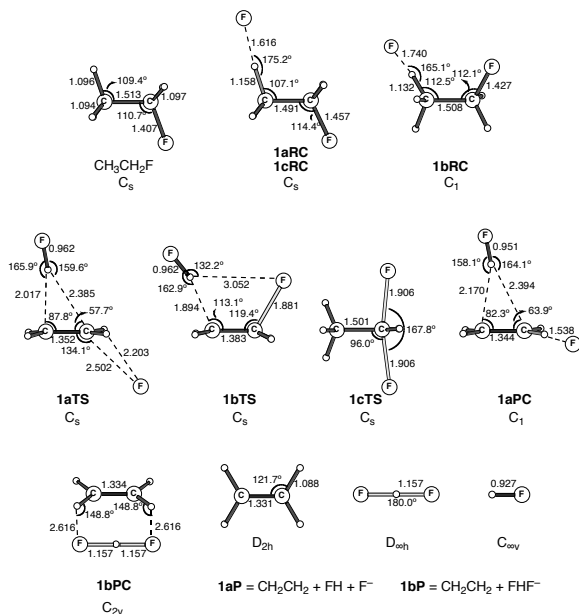


Figure 4.1. Geometries (in Å, deg) of stationary points along the potential energy surfaces for the anti-E2, syn-E2 and S_N2 reactions of $F^- + CH_3CH_2F$ (reaction 1), computed at OLYP/TZ2P.

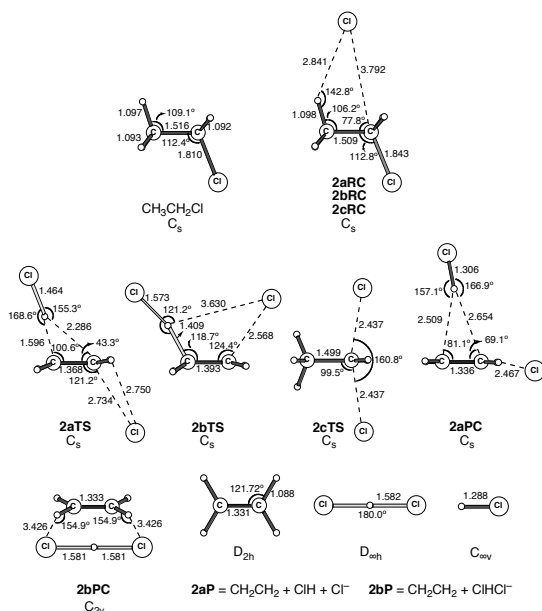


Figure 4.2. Geometries (in Å, deg) of stationary points along the potential energy surfaces for the anti-E2, syn-E2 and S_N2 reactions of $\text{Cl}^- + \text{CH}_3\text{CH}_2\text{Cl}$ (reaction 2), computed at OLYP/TZ2P.

For both, $\text{F}^- + \text{CH}_3\text{CH}_2\text{F}$ and $\text{Cl}^- + \text{CH}_3\text{CH}_2\text{Cl}$, the anti-E2, syn-E2 and S_N2 reactions proceed from the reactants via formation of a reactant complex (RC) towards the transition state (TS) and, finally, a product complex (PC). In the anti-E2 reactant complex, the base X^- binds the $\text{C}^\beta\text{--H}$ bond that is anti to $\text{C}^\alpha\text{--X}$ with $\text{X}^-\text{--H}^\beta$ distances of 1.616 and 2.841 Å in **1aRC** and **2aRC**, respectively (see Figures 4.1 and 4.2). The $\text{C}^\beta\text{--H}$ bond that participates in the hydrogen bond with the halide anion expands by 0.062 Å in **1aRC** (from 1.096 to 1.158 Å) and only very slightly, i.e., by 0.001 Å in **2aRC** (from 1.097 to 1.098) if compared to the isolated substrates $\text{CH}_3\text{CH}_2\text{F}$ and $\text{CH}_3\text{CH}_2\text{Cl}$, respectively. In the anti-E2 transition states **1aTS** and **2aTS**, the elongation of the $\text{C}^\beta\text{--H}$ bonds further increases to 0.921 and 0.499 Å, respectively, again relative to the isolated substrates. The resulting product complexes **1aPC** and **2aPC** are composed of three rigid fragments, the conjugate acid HX , the olefin CH_2CH_2 and the leaving group X^- , that may eventually separate into products (**1aP** and **2aP**).

The syn-E2 elimination proceeds only in the case of $\text{F}^- + \text{CH}_3\text{CH}_2\text{F}$ via a separate reactant complex **1bRC** (see Figure 4.1). For $\text{Cl}^- + \text{CH}_3\text{CH}_2\text{Cl}$, all three elementary reactions (anti-E2, syn-E2 and S_N2) go via one and the same reactant complex, i.e., **2aRC** = **2bRC** = **2cRC** (see Figure 4.2). In the syn-E2 transition states **1bTS** and **2bTS**, the $\text{C}^\beta\text{--H}$ bonds are elongated by 0.798 and 0.312 Å and are oriented syn with respect to the $\text{C}^\alpha\text{--X}$ bond (see Figures 4.1 and 4.2). At variance with the anti-E2 pathway, the syn-E2 pathway leads to product complexes **1bPC** and **2bPC** that are composed of *two* rigid fragments: the leaving group microsolvated by the conjugate acid, XHX^- , and the olefin

CH_2CH_2 . These product complexes most easily dissociate into the products $\text{CH}_2\text{CH}_2 + \text{XHX}^-$ (**1bP** and **2bP**).

$\text{S}_{\text{N}}2$ substitution proceeds for both, $\text{F}^- + \text{CH}_3\text{CH}_2\text{F}$ and $\text{Cl}^- + \text{CH}_3\text{CH}_2\text{Cl}$, from the same reactant complex as the anti-E2 elimination (i.e., $\text{aRC} = \text{cRC}$). But now, the halide anion approaches to the backside of the α -methyl group of the substrate which leads to the $\text{S}_{\text{N}}2$ transition states **1cTS** and **2cTS** in which a new $\text{X}-\text{C}^\alpha$ bond has been partially formed while simultaneously the old $\text{C}^\alpha-\text{X}$ bond is elongated (see Figures 4.1 and 4.2). Note that, in our symmetric $\text{S}_{\text{N}}2$ model reactions, the nucleophile- C^α and C^α -leaving group bonds are of the same length, namely, 1.906 and 2.437 Å in **1cTS** and **2cTS** (see Figures 4.1 and 4.2), and that the product complexes and products are identical to the corresponding reactant complexes and reactants.

4.3.2. *Ab Initio* Benchmark Potential Energy Surfaces

Based on the above OLYP/TZ2P geometries, we have computed our *ab initio* benchmark potential energy surfaces, which are summarized as relative energies in Tables 4.1 and 4.2 for reactions 1 and 2, respectively. The extrapolated CBS CCSD(T) values are also listed therein.

Table 4.1. Energies relative to reactants (in kcal/mol) of stationary points along the reaction coordinate for the anti-E2, syn-E2 and $\text{S}_{\text{N}}2$ reactions of $\text{F}^- + \text{CH}_3\text{CH}_2\text{F}$, computed at several levels of the *ab initio* theory.

| Method | anti-E2 | | | | syn-E2 | | | | $\text{S}_{\text{N}}2$ | |
|------------------------|---------|-------|-------|-------|--------|-------|--------|--------|------------------------|-------|
| | 1aRC | 1aTS | 1aPC | 1aP | 1bRC | 1bTS | 1bPC | 1bP | 1cRC | 1cTS |
| <u>aug-cc-pVDZ</u> | | | | | | | | | | |
| HF | -10.49 | 4.81 | 0.12 | 16.77 | -7.62 | 18.08 | -28.00 | -23.55 | -10.49 | 8.71 |
| MP2 | -15.23 | -1.77 | -6.90 | 15.96 | -11.01 | 4.86 | -33.50 | -27.40 | -15.23 | 1.03 |
| MP4(SDTQ) | -15.64 | -1.44 | -6.03 | 17.10 | -11.49 | 5.00 | -31.68 | -25.30 | -15.64 | -2.74 |
| CCSD | -14.76 | -0.30 | -5.43 | 16.42 | -10.92 | 8.38 | -32.65 | -26.70 | -14.76 | 1.80 |
| CCSD(T) | -15.81 | -2.03 | -7.16 | 16.11 | -11.71 | 5.16 | -33.88 | -27.53 | -15.81 | -1.06 |
| <u>aug-cc-pVTZ</u> | | | | | | | | | | |
| HF | -9.63 | 5.22 | 0.72 | 16.63 | -7.05 | 18.42 | -28.46 | -24.25 | -9.63 | 11.35 |
| MP2 | -14.69 | -1.07 | -6.06 | 16.48 | -10.69 | 5.07 | -33.81 | -27.99 | -14.69 | 3.56 |
| MP4(SDTQ) | -15.02 | -0.88 | -5.35 | 17.29 | -11.08 | 5.05 | -32.33 | -26.27 | -15.02 | -0.20 |
| CCSD | -14.13 | 0.56 | -4.47 | 17.01 | -10.54 | 8.89 | -32.96 | -27.29 | -14.13 | 4.58 |
| CCSD(T) | -15.17 | -1.31 | -6.28 | 16.51 | -11.30 | 5.47 | -34.30 | -28.28 | -15.17 | 1.56 |
| <u>CBS^a</u> | | | | | | | | | | |
| CCSD(T) | -15.27 | -1.19 | -6.17 | 16.74 | -11.37 | 5.46 | -34.28 | -28.29 | -15.27 | 1.55 |
| <u>aug-cc-pVQZ</u> | | | | | | | | | | |
| HF | -9.58 | 5.12 | 0.57 | 16.31 | -7.03 | 18.30 | -28.43 | -24.31 | -9.58 | 11.50 |
| MP2 | -14.61 | -1.25 | -6.33 | 15.88 | -10.60 | 4.93 | -33.92 | -28.30 | -14.61 | 3.81 |
| CCSD | -14.00 | 0.50 | -4.61 | 16.45 | -10.41 | 8.91 | -32.98 | -27.53 | -14.00 | 4.97 |
| CCSD(T) | -14.99 | -1.33 | -6.39 | 15.95 | -11.12 | 5.54 | -34.27 | -28.49 | -14.99 | 1.99 |
| <u>CBS^b</u> | | | | | | | | | | |
| CCSD(T) | -14.89 | -1.27 | -6.35 | 15.77 | -11.00 | 5.68 | -37.39 | -28.60 | -14.89 | 2.20 |

^aThese values were obtained from 2-point fits (aug-cc-pVDZ and aug-cc-pVTZ) to eq 7 of Ref. 55. ^bThese values were obtained from 2-point fits (aug-cc-pVTZ and aug-cc-pVQZ) to eq 7 of Ref. 55.

Table 4.2. Energies relative to reactants (in kcal/mol) of stationary points along the reaction coordinate for the anti-E2, syn-E2 and S_N2 reactions of Cl[−] + CH₃CH₂Cl, computed at several levels of the *ab initio* theory.

| Method | anti-E2 | | | | syn-E2 | | | | S _N 2 | |
|--------------------------|---------|-------|-------|-------|--------|-------|-------|-------|------------------|-------|
| | 2aRC | 2aTS | 2aPC | 2aP | 2bRC | 2bTS | 2bPC | 2bP | 2cRC | 2cTS |
| <u>aug-cc-pV(D + d)Z</u> | | | | | | | | | | |
| HF | −9.33 | 26.88 | 10.03 | 17.93 | −9.33 | 43.57 | 0.43 | 2.61 | −9.33 | 9.06 |
| MP2 | −11.33 | 16.22 | 9.19 | 22.67 | −11.33 | 29.51 | −5.21 | −1.50 | −11.33 | 6.67 |
| MP4(SDTQ) | −11.45 | 16.22 | 8.08 | 21.30 | −11.45 | 29.12 | −5.01 | −1.27 | −11.45 | 4.39 |
| CCSD | −10.98 | 18.95 | 8.30 | 20.40 | −10.98 | 33.10 | −4.12 | −0.67 | −10.98 | 6.43 |
| CCSD(T) | −11.43 | 16.14 | 7.50 | 20.52 | −11.43 | 29.17 | −5.57 | −1.86 | −11.43 | 4.12 |
| <u>aug-cc-pV(T + d)Z</u> | | | | | | | | | | |
| HF | −9.06 | 28.04 | 10.27 | 17.61 | −9.06 | 44.99 | 0.99 | 3.04 | −9.06 | 10.38 |
| MP2 | −11.06 | 17.90 | 10.80 | 23.86 | −11.06 | 31.06 | −4.42 | −0.90 | −11.06 | 8.22 |
| CCSD | −10.64 | 20.97 | 9.90 | 21.38 | −10.64 | 35.11 | −3.15 | 0.07 | −10.64 | 8.15 |
| CCSD(T) | −11.10 | 17.92 | 9.17 | 21.58 | −11.10 | 30.82 | −4.90 | −1.42 | −11.10 | 5.70 |
| CBS ^a | | | | | | | | | | |
| CCSD(T) | −11.07 | 18.18 | 9.77 | 22.16 | −11.07 | 30.92 | −4.85 | −1.42 | −11.07 | 5.81 |

^aThese values were obtained from 2-point fits [aug-cc-pV(D + d)Z and aug-cc-pV(T + d)Z] to eq 7 of Ref. 55.

First, we examine the PES obtained for the anti-E2 elimination of F[−] + CH₃CH₂F. The energy of respective reactant complex, **1aRC**, computed with our best basis set (aug-cc-pVQZ) ranges from −9.58 to −14.61 to −14.00 to −14.99 kcal/mol for HF, MP2, CCSD and CCSD(T). Note that, due to large space requirements, full MP4 calculations for the QZ basis set were not possible. The three highest-level values are equal to each other within 1.0 kcal/mol (see Table 4.1). Similarly, the energy of the transition state, **1aTS**, computed again with our best basis set (aug-cc-pVQZ) varies from 5.12 to −1.25 to 0.50 to −1.33 kcal/mol for HF, MP2, CCSD and CCSD(T). Thus, not unexpectedly, HF significantly overestimates the overall barrier, which is significantly reduced by the incorporation of Coulomb correlation into theoretical treatment. The inclusion of the triple excitations within the CCSD method further reduces the overall barrier by 1.8 kcal/mol. The three highest-level values are within a range of 1.8 kcal/mol. Furthermore, the CCSD(T) values are converged to the basis-set size (at aug-cc-pVQZ) to within a few hundredths of a kcal/mol for the RC and the TS (see Table 4.1). Note that CBS CCSD(T) values do not differ much from the best pure values [CCSD(T)].

For the anti-E2 elimination of Cl[−] + CH₃CH₂Cl, the energy of the reactant complex, **2aRC**, computed with our best basis set [now, with aug-cc-pV(T + d)Z] varies relatively little along the range of methods, that is ca. 2 kcal/mol, from −9.06 to −11.06 to −10.64 to −11.10 for HF, MP2, CCSD and CCSD(T), respectively (see Table 4.2). Now, our three highest-level values are equal to each other within 0.5 kcal/mol. At variance, the energy of the transition state, **2aTS**, depends more delicately on the level at which correlation is treated. This TS energy computed again with aug-cc-pV(T + d)Z varies from 28.04 to 17.90 to 20.97 to 17.92 kcal/mol along HF, MP2, CCSD and CCSD(T). Note how HF dramatically overestimates the overall barrier, that is, by ca. 10 kcal/mol! Also note the

substantial impact of including triple excitations in the CCSD approach which reduced the overall barrier by an additional 3.0 kcal/mol. The three highest-level values are now distributed over a range of 3.1 kcal/mol (see Table 4.2).

Next, we examine the PES of the syn-E2 elimination of $\text{F}^- + \text{CH}_3\text{CH}_2\text{F}$. The energy of reactant complex **1bRC** computed with our best basis set (aug-cc-pVQZ) shows a similar behavior as that of the anti-E2 elimination. The energy of this RC varies from -7.03 to -10.60 to -10.41 to -11.12 kcal/mol for HF, MP2, CCSD and CCSD(T), and the three highest-level values are within a range of less than a kcal/mol (see Table 4.1). In turn, the energy of the TS is more sensitive to the level at which correlation is treated. This TS energy computed again with our best basis set, aug-cc-pVQZ, varies from 18.30 to 4.93 to 8.91 to 5.54 kcal/mol along HF, MP2, CCSD and CCSD(T). Note again that HF clearly overestimates the barrier by 9 kcal/mol (see Table 4.1). Moreover, the CCSD(T) values are converged as a function of the basis-set size (at aug-cc-pVQZ) to within less than half a kcal/mol (see Table 4.1).

The syn-E2 elimination of $\text{Cl}^- + \text{CH}_3\text{CH}_2\text{Cl}$ proceeds via the same reactant complex as the anti-E2 elimination, which has been already examined above. The energy of the syn-E2 transition state computed at aug-cc-pV(T + *d*)Z is again sensitive to the level at which correlation is treated. It ranges from 44.99 to 31.06 to 35.11 to 30.82 along the series of *ab initio* methods (see Table 4.2). The CCSD(T) values change by less than 2 kcal/mol going from the aug-cc-pV(D + *d*)Z to the aug-cc-pV(T + *d*)Z basis set (see Table 4.2) and again do not differ much from the CBS energies.

The $\text{S}_{\text{N}}2$ transition states for reactions 1c and 2c are also found to be quite sensitive to the level at which correlation is treated. Thus, at the HF level, at which Coulomb correlation is not included, the energies of the transition states **1cTS** and **2cTS** computed with our best basis set [aug-cc-pVQZ for X = F and aug-cc-pV(T + *d*)Z for X = Cl] amount to 11.50 and 10.38 kcal/mol, respectively (see Table 4.1 and 4.2). Introducing Coulomb correlation into the theoretical treatment substantially lowers the barrier. Thus, along HF, MP2, CCSD and CCSD(T), the energy of **1cTS** ranges from 11.50 to 3.81 to 4.97 to 1.99 kcal/mol and that of **2cTS** from 10.38 to 8.22 to 8.15 to 5.70 kcal/mol (see Table 4.1 and 4.2). Thus, HF significantly overestimates the overall barriers by some 10 and 5 kcal/mol, respectively. Note again how including the triple excitations in the CCSD calculations reduces the overall barrier by 3.0 and 2.4 kcal/mol, respectively. The three highest-level values are within a range of 3.0 and 2.5 kcal/mol for reaction 1c and 2c, respectively. Furthermore, the CCSD(T) values for **1cTS** is converged as a function of the basis-set size to within 0.4 kcal/mol and again do not differ much from the CBS extrapolated CCSD(T) values.

In conclusion, our best CCSD(T) estimate leads to a relative order in overall barriers (i.e., TS energy relative to reactants) of anti-E2 (X = F: -1.33 kcal/mol) < $\text{S}_{\text{N}}2$ (X = F:

+1.99 kcal/mol) < syn-E2 (X = F: +5.54 kcal/mol) \sim S_N2 (X = Cl: +5.70 kcal/mol) < anti-E2 (X = Cl: +17.92 kcal/mol) < syn-E2 (X = Cl: +30.82 kcal/mol). The change in preference from anti-E2 for X = F to S_N2 for X = Cl is also recovered in the trend of the *central* barriers. Our benchmark consolidates the G2+ values for the relative energies of **1aRC**, **1aTS**, **1bTS** and **1cTS** on the PES of F⁻ + CH₃CH₂F computed by Gronert and coworkers⁷ which agree within 2.3 kcal/mol with our best CCSD(T) estimates.

4.3.3. Performance of DFT: Mean Absolute Error

Next, we examine the relative energies of stationary points computed with: (i) the LDA functional VWN; (ii) the GGA functionals BP86, BLYP, PW91, PBE, RPBE, revPBE, FT97, HCTH/93, HCTH/120, HCTH/147, HCTH/407, BOP, OPBE and OLYP; (iii) the meta-GGA functionals PKZB, VS98, BLAP3, OLAP3, TPSS and M06-L; and (iv) the hybrid functionals B3LYP, O3LYP, KMLYP, BHandH, mPBE0KCIS, mPW1K, M05, M05-2X, M06 and MO6-2X using the following procedure: (i) all functionals except OLYP are evaluated using the OLYP/ae-TZ2P density computed at the OLYP/TZ2P geometries; (ii) the OLYP functional is evaluated using the OLYP/TZ2P density computed at the OLYP/TZ2P geometries (see methodological section). Extensive previous validation studies have shown that the use of the all-electron ae-TZ2P versus the frozen core TZ2P basis set leads to differences in relative energies of less than half a kcal/mol.⁴⁷ The DFT relative energies for reactions 1 and 2 are collected in Tables 4.3 and 4.4, respectively.

Here, we focus on the overall barrier, that is, the difference in energy between the TS and the separate reactants (R) and the central barrier, that is, the difference in energy between the TS and the reactant complex (RC). The overall barrier is decisive for the rate of chemical reactions in the gas phase, in particular, if they occur under low-pressure conditions,^{3,10} whereas the central barrier becomes decisive in the high-pressure regime, when termolecular collisions are sufficiently efficient to cool the otherwise rovibrationally hot reactant complex, causing it to be in thermal equilibrium with the environment.^{3,10}

The performance of the various density functional approaches is assessed by a systematic comparison of the resulting PESes with our CCSD(T)/aug-cc-pVQZ benchmark in the case of reaction 1 (Table 4.1) and CCSD(T)/aug-cc-pV(T + *d*)Z benchmark in the case of reaction 2 (Table 4.2). Note that our best CCSD(T) results do not differ much from the CBS extrapolated CCSD(T) values. Thus, they were used (instead of the CBS values) as our benchmark since we prefer to have as little as possible empirical extrapolations in the benchmark reference values. For all 31 functionals, we have computed the errors in the overall and central barriers (see Table 4.5) and the corresponding mean absolute errors (MAE) relative to the CCSD(T) benchmarks for all

Table 4.3. Energies relative to reactants (in kcal/mol) of stationary points along the reaction coordinate for the anti-E2, syn-E2 and S_N2 reactions of F⁻ + CH₃CH₂F, computed at several levels of the density functional theory.

| Method | anti-E2 | | | | syn-E2 | | | | S _N 2 | |
|---------------------------|---------|--------|--------|-------|--------|--------|--------|--------|------------------|--------|
| | 1aRC | 1aTS | 1aPC | 1aP | 1bRC | 1bTS | 1bPC | 1bP | 1cRC | 1cTS |
| <i>LDA</i> | | | | | | | | | | |
| VWN | -28.23 | -8.54 | -13.84 | 26.01 | -22.02 | -12.50 | -42.70 | -35.13 | -28.23 | -13.67 |
| <i>GGA's</i> | | | | | | | | | | |
| BP86 | -22.19 | -8.27 | -12.55 | 16.97 | -16.77 | -7.51 | -40.68 | -35.87 | -22.19 | -9.33 |
| BLYP | -22.23 | -11.55 | -15.08 | 13.55 | -17.02 | -8.66 | -43.95 | -38.71 | -22.23 | -11.27 |
| PW91 | -24.12 | -9.58 | -13.67 | 18.85 | -18.66 | -9.29 | -42.15 | -35.61 | -24.12 | -11.39 |
| PBE | -23.79 | -9.36 | -13.49 | 18.48 | -18.37 | -8.98 | -41.73 | -35.43 | -23.79 | -10.73 |
| RPBE | -21.79 | -9.61 | -13.49 | 14.89 | -16.74 | -7.39 | -41.71 | -35.87 | -21.79 | -8.56 |
| revPBE | -21.37 | -8.83 | -12.85 | 15.00 | -16.26 | -6.85 | -40.94 | -35.73 | -21.37 | -7.91 |
| FT97 | -19.78 | -6.54 | -11.07 | 13.27 | -14.08 | -4.80 | -37.86 | -35.53 | -19.78 | -7.19 |
| HCTH/93 | -18.75 | -7.32 | -11.79 | 12.26 | -13.98 | -3.73 | -40.42 | -36.26 | -18.75 | -2.52 |
| HCTH/120 | -21.90 | -9.85 | -14.05 | 15.07 | -16.92 | -7.17 | -42.93 | -36.60 | -21.90 | -7.37 |
| HCTH/147 | -21.07 | -8.93 | -13.26 | 14.58 | -16.10 | -6.23 | -42.13 | -36.45 | -21.07 | -6.14 |
| HCTH/407 | -21.52 | -10.56 | -14.71 | 13.39 | -16.74 | -6.60 | -44.06 | -37.30 | -21.52 | -5.78 |
| BOP | -19.67 | -9.98 | -13.56 | 11.28 | -14.68 | -6.01 | -42.21 | -38.16 | -19.67 | -7.66 |
| OPBE | -18.68 | -3.26 | -8.45 | 15.78 | -13.79 | -2.07 | -36.62 | -32.69 | -18.68 | -0.22 |
| OLYP | -20.01 | -7.95 | -12.49 | 12.85 | -15.20 | -4.93 | -41.40 | -36.41 | -20.01 | -4.16 |
| <i>Meta-GGA's</i> | | | | | | | | | | |
| PKZB | -19.16 | -6.56 | -9.65 | 14.74 | -14.55 | -3.93 | -38.36 | -32.85 | -19.16 | -7.27 |
| VS98 | -20.80 | -13.42 | -15.04 | 11.99 | -16.25 | -7.04 | -43.88 | -35.97 | -20.80 | -14.06 |
| BLAP3 | -18.54 | -8.58 | -12.38 | 12.58 | -14.01 | -2.47 | -41.65 | -36.58 | -18.54 | -4.88 |
| OLAP3 | -16.23 | -4.62 | -9.31 | 12.24 | -12.13 | 1.57 | -38.65 | -33.88 | -16.23 | 2.25 |
| TPSS | -21.38 | -5.26 | -8.94 | 19.81 | -16.28 | -4.16 | -37.83 | -32.52 | -21.38 | -10.03 |
| M06-L | -20.04 | -1.23 | -5.44 | 20.54 | -15.33 | 1.68 | -32.57 | -27.78 | -20.04 | -2.95 |
| <i>Hybrid functionals</i> | | | | | | | | | | |
| B3LYP | -19.30 | -5.38 | -10.66 | 15.90 | -14.50 | -2.00 | -40.32 | -35.34 | -19.30 | -4.01 |
| O3LYP | -18.12 | -2.55 | -7.97 | 16.52 | -13.46 | 0.40 | -38.06 | -33.35 | -18.12 | 0.24 |
| KMLYP | -16.14 | 6.09 | -2.78 | 23.69 | -11.77 | 8.28 | -33.82 | -28.53 | -16.14 | 7.54 |
| BHandH | -19.68 | 3.90 | -4.81 | 26.52 | -14.87 | 3.86 | -35.53 | -29.15 | -19.68 | 2.76 |
| mPBE0KCIS | -19.57 | -4.44 | -10.63 | 16.89 | -14.77 | -1.77 | -39.63 | -33.94 | -19.57 | -1.15 |
| mPW1K | -15.32 | 4.26 | -3.38 | 20.37 | -10.96 | 7.06 | -33.31 | -29.07 | -15.32 | 6.24 |
| M05 | -18.68 | -3.51 | -8.73 | 18.54 | -14.64 | 0.81 | -38.03 | -32.01 | -18.68 | -0.81 |
| M05-2X | -14.53 | 0.99 | -5.72 | 18.33 | -10.30 | 3.85 | -39.28 | -34.27 | -14.53 | 3.97 |
| M06 | -18.21 | -2.21 | -7.47 | 17.88 | -13.96 | 1.14 | -35.19 | -30.59 | -18.21 | -0.35 |
| M06-2X | -15.67 | 1.49 | -5.62 | 18.37 | -11.47 | 4.03 | -37.77 | -32.90 | -15.67 | 5.82 |

model reactions together as well as for certain categories thereof (see Table 4.6).

It is clear from Tables 4.5 and 4.6 that LDA suffers from its notorious overbinding: it yields too low barriers and too exothermic complexation and reaction energies (see also Tables 4.3 and 4.4). But also many of the GGA (e.g., BLYP, BOP, BP86, PW91, PBE)

Table 4.4. Energies relative to reactants (in kcal/mol) of stationary points along the reaction coordinate for the anti-E2, syn-E2 and S_N2 reactions of Cl[−] + CH₃CH₂Cl, computed at several levels of the density functional theory.

| Method | anti-E2 | | | | syn-E2 | | | | S _N 2 | |
|---------------------------|---------|-------|-------|-------|--------|-------|--------|--------|------------------|-------|
| | 2aRC | 2aTS | 2aPC | 2aP | 2bRC | 2bTS | 2bPC | 2bP | 2cRC | 2cTS |
| <i>LDA</i> | | | | | | | | | | |
| VWN | −13.32 | 5.00 | 12.19 | 29.51 | −13.32 | 11.45 | −10.74 | −7.11 | −13.32 | −4.64 |
| <i>GGA</i> s | | | | | | | | | | |
| BP86 | −10.66 | 7.21 | 8.80 | 20.08 | −10.66 | 15.35 | −11.23 | −9.24 | −10.66 | −1.92 |
| BLYP | −11.08 | 5.28 | 4.43 | 15.33 | −11.08 | 14.04 | −14.17 | −11.93 | −11.08 | −3.69 |
| PW91 | −12.23 | 6.38 | 8.42 | 22.36 | −12.23 | 14.22 | −11.98 | −8.56 | −12.23 | −3.24 |
| PBE | −11.91 | 6.85 | 8.62 | 22.10 | −11.91 | 14.75 | −11.62 | −8.49 | −11.91 | −2.43 |
| RPBE | −11.20 | 7.78 | 6.85 | 18.45 | −11.20 | 16.27 | −12.47 | −9.38 | −11.20 | −0.67 |
| revPBE | −10.69 | 8.13 | 7.59 | 18.55 | −10.69 | 16.59 | −11.89 | −9.29 | −10.69 | −0.20 |
| FT97 | −7.86 | 10.09 | 11.41 | 17.68 | −7.86 | 19.37 | −7.85 | −6.76 | −7.86 | −0.04 |
| HCTH/93 | −9.37 | 10.25 | 6.99 | 15.53 | −9.37 | 19.56 | −11.80 | −9.74 | −9.37 | 3.82 |
| HCTH/120 | −11.60 | 7.46 | 6.03 | 18.16 | −11.60 | 16.42 | −13.03 | −9.56 | −11.60 | −0.49 |
| HCTH/147 | −10.89 | 8.14 | 6.62 | 17.62 | −10.89 | 17.15 | −12.62 | −9.54 | −10.89 | 0.50 |
| HCTH/407 | −11.71 | 8.19 | 4.55 | 16.45 | −11.71 | 17.82 | −13.88 | −9.93 | −11.71 | 1.99 |
| BOP | −9.91 | 6.83 | 4.60 | 13.45 | −9.91 | 15.96 | −13.74 | −12.01 | −9.91 | −1.20 |
| OPBE | −8.64 | 13.99 | 12.33 | 20.78 | −8.64 | 22.32 | −8.34 | −6.24 | −8.64 | 7.56 |
| OLYP | −9.66 | 10.68 | 7.45 | 16.33 | −9.66 | 19.58 | −11.81 | −9.28 | −9.66 | 4.04 |
| <i>Meta-GGA</i> s | | | | | | | | | | |
| PKZB | −10.93 | 11.36 | 8.73 | 17.81 | −10.93 | 20.17 | −10.07 | −7.06 | −10.93 | 1.23 |
| VS98 | −14.96 | 8.52 | 2.10 | 14.62 | −14.96 | 17.05 | −12.73 | −8.46 | −14.96 | −6.44 |
| BLAP3 | −11.24 | 8.51 | 3.28 | 14.65 | −11.24 | 18.94 | −13.92 | −10.77 | −11.24 | 0.08 |
| OLAP3 | −9.92 | 14.00 | 6.20 | 15.82 | −9.92 | 24.53 | −11.55 | −8.08 | −9.92 | 7.72 |
| TPSS | −10.99 | 9.34 | 8.95 | 20.88 | −10.99 | 17.58 | −9.89 | −7.01 | −10.99 | −3.22 |
| M06-L | −14.02 | 12.92 | 8.99 | 25.92 | −14.02 | 22.77 | −4.73 | −2.25 | −14.02 | 2.63 |
| <i>Hybrid functionals</i> | | | | | | | | | | |
| B3LYP | −10.60 | 11.00 | 7.03 | 17.83 | −10.60 | 21.22 | −10.78 | −8.53 | −10.60 | 0.92 |
| O3LYP | −9.63 | 14.78 | 10.26 | 19.98 | −9.63 | 24.43 | −8.70 | −6.19 | −9.63 | 6.39 |
| KMLYP | −10.49 | 20.85 | 13.68 | 26.27 | −10.49 | 32.97 | −3.27 | −1.21 | −10.49 | 8.45 |
| BHandH | −11.59 | 18.31 | 14.43 | 29.18 | −11.59 | 29.33 | −4.38 | −1.25 | −11.59 | 5.60 |
| mPBE0KCIS | −10.94 | 13.10 | 8.92 | 21.03 | −10.94 | 23.21 | −9.44 | −6.45 | −10.94 | 4.26 |
| mPW1K | −9.55 | 19.65 | 13.23 | 23.78 | −9.55 | 31.18 | −4.58 | −2.41 | −9.55 | 8.20 |
| M05 | −11.99 | 19.83 | 3.73 | 21.95 | −11.99 | 23.34 | −8.86 | −3.70 | −11.99 | 4.64 |
| M05-2X | −8.93 | 12.58 | 16.60 | 18.97 | −8.93 | 28.46 | −7.75 | −5.67 | −8.93 | 6.84 |
| M06 | −12.68 | 17.33 | 6.17 | 22.96 | −12.68 | 23.67 | −6.49 | −2.92 | −12.68 | 3.36 |
| M06-2X | −12.49 | 10.65 | 14.98 | 22.49 | −12.49 | 30.29 | −5.85 | −4.74 | −12.49 | 10.73 |

and some meta-GGA functionals (VS98, TPSS) perform more or less equally poorly as LDA: together, these poorly performing functionals have MAE values, for all reactions together, in the range of 7 – 9 kcal/mol for central and 9 – 14 kcal/mol for overall barriers (see Table 4.6).

Table 4.5. Errors in overall and central barriers (in kcal/mol) for various density functionals for the anti-E2, syn-E2 and S_N2 reactions of X⁻ + CH₃CH₂X (X = F, Cl) compared to CCSD(T).^a

| Method | anti-E2 | | | | syn-E2 | | | | S _N 2 | | | |
|---------------------------|-------------------------|--------|--------------------------|--------|-------------------------|--------|--------------------------|--------|-------------------------|--------|--------------------------|-------|
| | Err. in barr. rel. to R | | Err. in barr. rel. to RC | | Err. in barr. rel. to R | | Err. in barr. rel. to RC | | Err. in barr. rel. to R | | Err. in barr. rel. to RC | |
| | F | Cl | F | Cl | F | Cl | F | Cl | F | Cl | F | Cl |
| <i>LDA</i> | | | | | | | | | | | | |
| VWN | -7.21 | -12.92 | 6.03 | -10.70 | -18.04 | -19.37 | -7.14 | -17.15 | -15.66 | -10.34 | -2.42 | -8.12 |
| <i>GGA's</i> | | | | | | | | | | | | |
| BP86 | -6.94 | -10.71 | 0.26 | -11.15 | -13.05 | -15.47 | -7.40 | -15.91 | -11.32 | -7.62 | -4.12 | -8.06 |
| BLYP | -10.22 | -12.64 | -2.98 | -12.66 | -14.20 | -16.78 | -8.30 | -16.80 | -13.26 | -9.39 | -6.02 | -9.41 |
| PW91 | -8.25 | -11.54 | 0.88 | -10.41 | -14.83 | -16.60 | -7.29 | -15.47 | -13.38 | -8.94 | -4.25 | -7.81 |
| PBE | -8.03 | -11.07 | 0.77 | -10.26 | -14.52 | -16.07 | -7.27 | -15.26 | -12.72 | -8.13 | -3.92 | -7.32 |
| RPBE | -8.28 | -10.14 | -1.48 | -10.04 | -12.93 | -14.55 | -7.31 | -14.45 | -10.55 | -6.37 | -3.75 | -6.27 |
| revPBE | -7.50 | -9.79 | -1.12 | -10.20 | -12.39 | -14.23 | -7.25 | -14.64 | -9.90 | -5.90 | -3.52 | -6.31 |
| FT97 | -5.21 | -7.83 | -0.42 | -11.07 | -10.34 | -11.45 | -7.38 | -14.69 | -9.18 | -5.74 | -4.39 | -8.98 |
| HCTH/93 | -5.99 | -7.67 | -2.23 | -9.40 | -9.27 | -11.26 | -6.41 | -12.99 | -4.51 | -1.88 | -0.75 | -3.61 |
| HCTH/120 | -8.52 | -10.46 | -1.61 | -9.96 | -12.71 | -14.40 | -6.91 | -13.90 | -9.36 | -6.19 | -2.45 | -5.69 |
| HCTH/147 | -7.60 | -9.78 | -1.52 | -9.99 | -11.77 | -13.67 | -6.79 | -13.88 | -8.13 | -5.20 | -2.05 | -5.41 |
| HCTH/407 | -9.23 | -9.73 | -2.70 | -9.12 | -12.14 | -13.00 | -6.52 | -12.39 | -7.77 | -3.71 | -1.24 | -3.10 |
| BOP | -8.65 | -11.09 | -3.97 | -12.28 | -11.55 | -14.86 | -7.99 | -16.05 | -9.65 | -6.90 | -4.97 | -8.09 |
| OPBE | -1.93 | -3.93 | 1.76 | -6.39 | -7.61 | -8.50 | -4.94 | -10.96 | -2.40 | 1.86 | 1.29 | -0.60 |
| OLYP | -6.62 | -7.24 | -1.60 | -8.68 | -10.47 | -11.24 | -6.39 | -12.68 | -6.15 | -1.66 | -1.13 | -3.10 |
| <i>Meta-GGA's</i> | | | | | | | | | | | | |
| PKZB | -5.23 | -6.56 | -1.06 | -6.73 | -9.47 | -10.65 | -6.04 | -10.82 | -9.26 | -4.47 | -5.09 | -4.64 |
| VS98 | -12.09 | -9.40 | -6.28 | -5.54 | -12.58 | -13.77 | -7.45 | -9.91 | -16.05 | -12.14 | -10.24 | -8.28 |
| BLAP3 | -7.25 | -9.41 | -3.70 | -9.27 | -8.01 | -11.88 | -5.12 | -11.74 | -6.87 | -5.62 | -3.32 | -5.48 |
| OLAP3 | -3.29 | -3.92 | -2.05 | -5.10 | -3.97 | -6.29 | -2.96 | -7.47 | 0.26 | 2.02 | 1.50 | 0.84 |
| TPSS | -3.93 | -8.58 | 2.46 | -8.69 | -9.70 | -13.24 | -4.54 | -13.35 | -12.02 | -8.92 | -5.63 | -9.03 |
| M06-L | 0.10 | -5.00 | 5.15 | -2.08 | -3.86 | -8.05 | 0.35 | -5.13 | -4.94 | -3.07 | 0.11 | -0.15 |
| <i>Hybrid Functionals</i> | | | | | | | | | | | | |
| B3LYP | -4.05 | -6.92 | 0.26 | -7.42 | -7.54 | -9.60 | -4.16 | -10.10 | -6.00 | -4.78 | -1.69 | -5.28 |
| O3LYP | -1.22 | -3.14 | 1.91 | -4.61 | -5.14 | -6.39 | -2.80 | -7.86 | -1.75 | 0.69 | 1.38 | -0.78 |
| KMLYP | 7.42 | 2.93 | 8.57 | 2.32 | 2.74 | 2.15 | 3.39 | 1.54 | 5.55 | 2.75 | 6.70 | 2.14 |
| BHandH | 5.23 | 0.39 | 9.92 | 0.88 | -1.68 | -1.49 | 2.07 | -1.00 | 0.77 | -0.10 | 5.46 | 0.39 |
| mPBE0KCIS | -3.11 | -4.82 | 1.47 | -4.98 | -7.31 | -7.61 | -3.66 | -7.77 | -3.14 | -1.44 | 1.44 | -1.60 |
| mPW1K | 5.59 | 1.73 | 5.92 | 0.18 | 1.52 | 0.36 | 1.36 | -1.19 | 4.25 | 2.50 | 4.58 | 0.95 |
| M05 | -2.18 | 1.91 | 1.51 | 2.71 | -4.73 | -7.48 | -1.21 | -6.68 | -2.80 | -1.06 | 0.89 | -0.26 |
| M05-2X | 2.32 | -5.34 | 1.86 | -7.51 | -1.69 | -2.36 | -2.51 | -4.53 | 1.98 | 1.14 | 1.52 | -1.03 |
| M06 | -0.88 | -0.59 | 2.34 | 0.99 | -4.40 | -7.15 | -1.56 | -5.57 | -2.34 | -2.34 | 0.88 | -0.76 |
| M06-2X | 2.82 | -7.27 | 3.50 | -5.88 | -1.51 | -0.53 | -1.16 | 0.86 | 3.83 | 5.03 | 4.51 | 6.42 |

^aRelative to CCSD(T)/aug-cc-pVQZ benchmark for reactions involving F and relative to CCSD(T)/aug-cc-pV(T + d)Z benchmark for reactions involving Cl. R = reactants, RC = reactant complex.

Best overall agreement with our *ab initio* benchmark barriers is obtained by representatives from each of the three categories of functionals, GGA, meta-GGA and hybrid DFT, with MAEs in central barriers of 4.3 (OPBE), 2.2 (M06-L) and 2.0 kcal/mol (M06), respectively, and MAEs in overall barriers of 4.4 (OPBE), 3.3 (OLAP3) and 1.6 kcal/mol (BHandH), respectively (see Table 4.6). The top 3 of best functionals is constituted for the central barriers by M06, M06-L and M05 with MAE values, for all reactions together, of 2.0, 2.2 and 2.2 kcal/mol, respectively, and for the overall barriers by BHandH, M05-2X and mPW1K with MAE values, for all reactions together, of 1.6,

Table 4.6. Mean absolute errors (MAE) in overall and central barriers (in kcal/mol) for various density functionals for the anti-E2, syn-E2 and S_N2 reactions of $X^- + CH_3CH_2X$ ($X = F, Cl$) compared to CCSD(T).^a

| Method | MAE in anti-E2 barr. | | MAE in syn-E2 barr. | | MAE in S_N2 barr. | | MAE in barr. X = F | | MAE in barr. X = Cl | | MAE | |
|---------------------------|----------------------|---------|---------------------|---------|---------------------|---------|--------------------|---------|---------------------|---------|---------|---------|
| | rel. to | rel. to | rel. to | rel. to | rel. to | rel. to | rel. to | rel. to | rel. to | rel. to | rel. to | rel. to |
| | R | RC | R | RC | R | RC | R | RC | R | RC | R | RC |
| <i>LDA</i> | | | | | | | | | | | | |
| VWN | 10.07 | 8.37 | 18.71 | 12.15 | 13.00 | 5.27 | 13.64 | 5.20 | 14.21 | 11.99 | 13.92 | 8.59 |
| <i>GGA's</i> | | | | | | | | | | | | |
| BP86 | 8.83 | 5.71 | 14.26 | 11.66 | 9.47 | 6.09 | 10.44 | 3.93 | 11.27 | 11.71 | 10.85 | 7.82 |
| BLYP | 11.43 | 7.82 | 15.49 | 12.55 | 11.33 | 7.72 | 12.56 | 5.77 | 12.94 | 12.96 | 12.75 | 9.36 |
| PW91 | 9.90 | 5.65 | 15.72 | 11.38 | 11.16 | 6.03 | 12.15 | 4.14 | 12.36 | 11.23 | 12.26 | 7.69 |
| PBE | 9.55 | 5.52 | 15.30 | 11.27 | 10.43 | 5.62 | 11.76 | 3.99 | 11.76 | 10.95 | 11.76 | 7.47 |
| RPBE | 9.21 | 5.76 | 13.74 | 10.88 | 8.46 | 5.01 | 10.59 | 4.18 | 10.35 | 10.25 | 10.47 | 7.22 |
| revPBE | 8.65 | 5.66 | 13.31 | 10.95 | 7.90 | 4.92 | 9.93 | 3.96 | 9.97 | 10.38 | 9.95 | 7.17 |
| FT97 | 6.52 | 5.75 | 10.90 | 11.04 | 7.46 | 6.69 | 8.24 | 4.06 | 8.34 | 11.58 | 8.29 | 7.82 |
| HCTH/93 | 6.83 | 5.82 | 10.27 | 9.70 | 3.20 | 2.18 | 6.59 | 3.13 | 6.94 | 8.67 | 6.76 | 5.90 |
| HCTH/120 | 9.49 | 5.79 | 13.56 | 10.41 | 7.78 | 4.07 | 10.20 | 3.66 | 10.35 | 9.85 | 10.27 | 6.75 |
| HCTH/147 | 8.69 | 5.76 | 12.72 | 10.34 | 6.67 | 3.73 | 9.17 | 3.45 | 9.55 | 9.76 | 9.36 | 6.61 |
| HCTH/407 | 9.48 | 5.91 | 12.57 | 9.46 | 5.74 | 2.17 | 9.71 | 3.49 | 8.81 | 8.20 | 9.26 | 5.85 |
| BOP | 9.87 | 8.13 | 13.21 | 12.02 | 8.28 | 6.53 | 9.95 | 5.64 | 10.95 | 12.14 | 10.45 | 8.89 |
| OPBE | 2.93 | 4.08 | 8.06 | 7.95 | 2.13 | 0.95 | 3.98 | 2.66 | 4.76 | 5.98 | 4.37 | 4.32 |
| OLYP | 6.93 | 5.14 | 10.86 | 9.54 | 3.91 | 2.12 | 7.75 | 3.04 | 6.71 | 8.15 | 7.23 | 5.60 |
| <i>Meta-GGAs</i> | | | | | | | | | | | | |
| PKZB | 5.90 | 3.90 | 10.06 | 8.43 | 6.87 | 4.87 | 7.99 | 4.06 | 7.23 | 7.40 | 7.61 | 5.73 |
| VS98 | 10.75 | 5.91 | 13.18 | 8.68 | 14.10 | 9.26 | 13.57 | 7.99 | 11.77 | 7.91 | 12.67 | 7.95 |
| BLAP3 | 8.33 | 6.49 | 9.95 | 8.43 | 6.25 | 4.40 | 7.38 | 4.05 | 8.97 | 8.83 | 8.17 | 6.44 |
| OLAP3 | 3.61 | 3.58 | 5.13 | 5.22 | 1.14 | 1.17 | 2.51 | 2.17 | 4.08 | 4.47 | 3.29 | 3.32 |
| TPSS | 6.26 | 5.58 | 11.47 | 8.95 | 10.47 | 7.33 | 8.55 | 4.21 | 10.25 | 10.36 | 9.40 | 7.28 |
| M06-L | 2.55 | 3.62 | 5.96 | 2.74 | 4.01 | 0.13 | 2.97 | 1.87 | 5.37 | 2.45 | 4.17 | 2.16 |
| <i>Hybrid Functionals</i> | | | | | | | | | | | | |
| B3LYP | 5.49 | 3.84 | 8.57 | 7.13 | 5.39 | 3.49 | 5.86 | 2.04 | 7.10 | 7.60 | 6.48 | 4.82 |
| O3LYP | 2.18 | 3.26 | 5.77 | 5.33 | 1.22 | 1.08 | 2.70 | 2.03 | 3.41 | 4.42 | 3.06 | 3.22 |
| KMLYP | 5.18 | 5.45 | 2.45 | 2.47 | 4.15 | 4.42 | 5.24 | 6.22 | 2.61 | 2.00 | 3.92 | 4.11 |
| BHandH | 2.81 | 5.40 | 1.59 | 1.54 | 0.44 | 2.93 | 2.56 | 5.82 | 0.66 | 0.76 | 1.61 | 3.29 |
| mPBE0KCIS | 3.97 | 3.23 | 7.46 | 5.72 | 2.29 | 1.52 | 4.52 | 2.19 | 4.62 | 4.78 | 4.57 | 3.49 |
| mPW1K | 3.66 | 3.05 | 0.94 | 1.28 | 3.38 | 2.77 | 3.79 | 3.95 | 1.53 | 0.77 | 2.66 | 2.36 |
| M05 | 2.05 | 2.11 | 6.11 | 3.95 | 1.93 | 0.58 | 3.24 | 1.20 | 3.48 | 3.22 | 3.36 | 2.21 |
| M05-2X | 3.83 | 4.69 | 2.03 | 3.52 | 1.56 | 1.28 | 2.00 | 1.96 | 2.95 | 4.36 | 2.47 | 3.16 |
| M06 | 0.74 | 1.67 | 5.78 | 3.57 | 2.34 | 0.82 | 2.54 | 1.59 | 3.36 | 2.44 | 2.95 | 2.02 |
| M06-2X | 5.05 | 4.69 | 1.02 | 1.01 | 4.43 | 5.47 | 2.72 | 3.06 | 4.28 | 4.39 | 3.50 | 3.72 |

^aRelative to CCSD(T)/aug-cc-pVQZ benchmark for reactions involving F and relative to CCSD(T)/aug-cc-pV(T + d)Z benchmark for reactions involving Cl. R = reactants, RC = reactant complex.

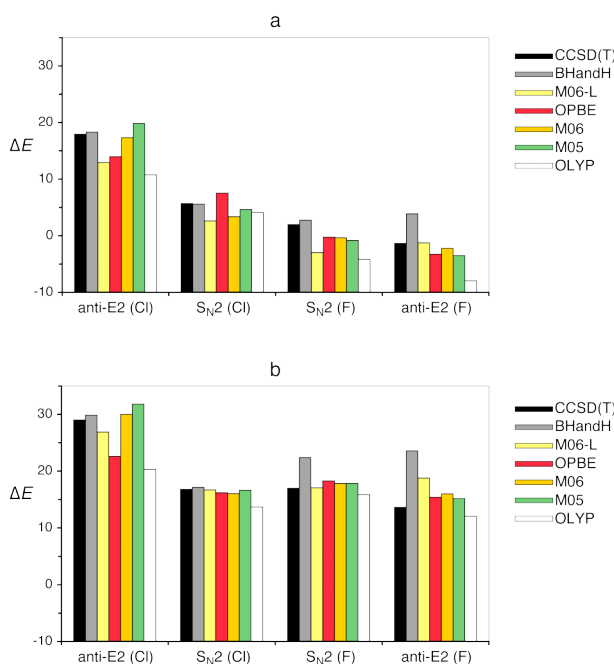
2.5 and 2.7 kcal/mol, respectively (see Table 4.6). An important point to note is that the OPBE functional is, not only for all reactions together but also for each individual category of reactions (e.g., anti-E2 reactions or reactions with $X = F$, etc.), in the top regions of performance (MAE in a category typically 1 – 6 kcal/mol, only for syn-E2 it reaches 8.1 kcal/mol) of all functionals studied, and it is the best of all *GGA* functionals. OLYP (7.2 and 5.6 kcal/mol relative to R and RC) and B3LYP (6.5 and 4.8 kcal/mol relative to R and RC) are of comparable quality, and both have somewhat larger MAE values for all reactions together than OPBE (4.4 and 4.3 kcal/mol relative to R and RC;

see Table 4.6). OLYP (MAE for S_N2 : 3.9 and 2.1 kcal/mol relative to R and RC) is however slightly better than B3LYP (MAE for S_N2 : 5.4 and 3.5 kcal/mol relative to R and RC) for the category of S_N2 reactions (see Table 4.6), in agreement with previous work.¹¹

Finally, complexation energies of the reactant complexes relative to reactants as well as reaction energies of our model reactions appear to be in general somewhat less dependent on the level of both *ab initio* (see Tables 4.1 and 4.2) and density functional theory (see Tables 4.3 - 4.6) if compared with the relative energies of the transition states discussed above. The density functionals that perform best for reaction barriers in terms of MAE, namely BHandH, M06, M06-L, M05, M05-2X and mPW1K, also show satisfactory agreement with the CCSD(T) benchmark regarding these complexation and reaction energies, with MAEs in the range of 0.7 – 4.8 kcal/mol (values not shown in Table 4.6). OPBE and B3LYP also achieve MAE values within this range whereas OLYP has MAE values of 3.5 and 6.0 kcal/mol for complexation and reaction energies respectively.

4.3.4. Performance of DFT: Trends

So far, we have concentrated on the mean average error (MAE) which leads to a certain ranking of density functionals regarding their performance in computing overall or central barriers for the six model reaction pathways (see Scheme 4.2). Interestingly (and



importantly), such an MAE-based ranking does not necessarily say something about the performance for reproducing the right trends in reactivity.

For example, according to the MAE criterion, BHandH and M06-L belong to the best functionals. Yet, they erroneously predict that for $F^- + CH_3CH_2F$,

Figure 4.3. Overall (a) and central (b) barriers (in kcal/mol) for the anti-E2 and S_N2 reactions of $X^- + CH_3CH_2X$ ($X = F, Cl$), computed with CCSD(T) and selected density functionals.

the anti-E2 reaction has both a higher overall and central barrier than the S_N2 reaction, as can be seen in Figures 4.3a and 4.3b, respectively (see also Tables 4.3 and 4.4). For comparison, both OPBE and OLYP do reproduce the correct trend (see Figure 4.3), in spite of the fact that the MAE is larger than for BHandH or M06-L (see Table 4.6). In the latter two functionals, the error is apparently somewhat less uniformly distributed. This is an interesting phenomenon but it should also not be overrated because the energy differences concerned are rather small.

M06 and M05 are good both in terms of one of the smallest MAE values (see Table 4.6) and a correct trend in reactivity (see Figure 4.3 and Tables 4.3 and 4.4). On the other hand, they are computationally somewhat more expensive than OPBE and OLYP. And, at variance with the latter, M06 and M05 are (in ADF) evaluated post-SCF with the density of another potential (e.g., OPBE or OLYP).

4.4. Conclusions

We have computed *ab initio* benchmarks for the archetypal competing E2 and S_N2 reactions of fluoride + fluoroethane and chloride + chloroethane. These benchmarks derive from hierarchical series of methods up to CCSD(T)/aug-cc-pVQZ [up to CCSD(T)/aug-cc-pV(T + *d*)Z for chloride + chloroethane], which are converged with respect to the basis-set size within less than half a kcal/mol. The resulting reaction profiles show that anti-E2 dominates for $F^- + CH_3CH_2F$ while S_N2 dominates for $Cl^- + CH_3CH_2Cl$. This change in preference is reflected by both overall and central barriers. On the other hand, syn-E2 is in both reaction systems the least favorable pathway.

Our *ab initio* benchmark is used to evaluate the performance of 31 density functionals for describing the above anti-E2, syn-E2 and S_N2 reactions. Best overall agreement regarding central reaction barriers with our *ab initio* benchmark is obtained by representatives from each of the three categories of functionals, GGA, meta-GGA and hybrid DFT, with mean absolute errors of 4.3 (OPBE), 2.2 (M06-L) and 2.0 kcal/mol (M06), respectively.

Importantly, the hybrid functional BHandH and the meta-GGA M06-L yield incorrect trends and qualitative features of the PESes (in particular, an erroneous preference for S_N2 over the anti-E2 in the case of $F^- + CH_3CH_2F$) even though they are among the best functionals as measured by their small mean absolute errors of 3.3 and 2.2 kcal/mol in reaction barriers. OLYP and B3LYP have somewhat higher mean absolute errors in central barriers (5.6 and 4.8 kcal/mol, respectively) but the error distribution is somewhat more uniform and, as a consequence, the correct trends are reproduced.

References

- 1 Smith, M. B.; March, J. *March's Advanced Organic Chemistry: Reactions, Mechanisms, and Structure*; Wiley: New York, 2007; Carey, F. A.; Sundberg, R. J. *Advanced Organic Chemistry, Part A*; 5th ed.; Springer: New York, 2007; Ingold, C. *Structure and Mechanism in Organic Chemistry*; 2nd ed.; Cornell University Press: Ithaca, NY, 1969; Lowry, T. H.; Richardson, K. S. *Mechanism and Theory in Organic Chemistry*; Harper and Row: New York, 1987.
- 2 Gronert, S. *Chem. Rev.* **2001**, *101*, 329; Gronert, S.; Pratt, L. M.; Mogali, S. *J. Am. Chem. Soc.* **2001**, *123*, 3081; Gronert, S. *Acc. Chem. Res.* **2003**, *36*, 848; Bickelhaupt, F. M.; de Koning, L. J.; Nibbering, N. M. M. *J. Org. Chem.* **1993**, *58*, 2436; Uggerud, E.; Bache-Andreassen, L. *Chem. Eur. J* **1999**, *5*, 1917; Gronert, S.; Fagin, A. E.; Okamoto, K.; Mogali, S.; Pratt, L. M. *J. Am. Chem. Soc.* **2004**, *126*, 12977; Villano, S. M.; Kato, S.; Bierbaum, V. M. *J. Am. Chem. Soc.* **2006**, *128*, 736; Bickelhaupt, F. M.; Buisman, G. J. H.; de Koning, L. J.; Nibbering, N. M. M.; Baerends, E. J. *J. Am. Chem. Soc.* **1995**, *117*, 9889; Flores, A. E.; Gronert, S. *J. Am. Chem. Soc.* **1999**, *121*, 2627; DePuy, C. H.; Gronert, S.; Mulin, A.; Bierbaum, V. M. *J. Am. Chem. Soc.* **1990**, *112*, 8650.
- 3 Bickelhaupt, F. M. *Mass Spectrom. Rev.* **2001**, *20*, 347.
- 4 Orita, A.; Otera, J. *Chem. Rev.* **2006**, *106*, 5387; Alunni, S.; De Angelis, F.; Ottavi, L.; Papavasileiou, M.; Tarantelli, F. *J. Am. Chem. Soc.* **2005**, *127*, 15151; Meng, Q.; Thibblin, A. *J. Am. Chem. Soc.* **1995**, *117*, 9399; Pirinccioglu, N.; Thibblin, A. *J. Am. Chem. Soc.* **1998**, *120*, 6512.
- 5 Bickelhaupt, F. M. *J. Comput. Chem.* **1999**, *20*, 114; Ensing, B.; Laio, A.; Gervasio, F. L.; Parrinello, M.; Klein, M. L. *J. Am. Chem. Soc.* **2004**, *126*, 9492; De Angelis, F.; Tarantelli, F.; Alunni, S. *J. Phys. Chem. B* **2006**, *110*, 11014; Almerindo, G. I.; Jr., J. R. P. *Org. Lett.* **2005**, *7*, 1821; Ensing, B.; Klein, M. L. *Proc. Natl. Acad. Sci.* **2005**, *102*, 6755; Chung, D. S.; Kim, C. K.; Lee, B.; Lee, I. *J. Phys. Chem. A* **1997**, *101*, 9097; Minato, T.; Yamabe, S. *J. Am. Chem. Soc.* **1985**, *107*, 4621; Minato, T.; Yamabe, S. *J. Am. Chem. Soc.* **1988**, *110*, 4586; Gronert, S. *J. Am. Chem. Soc.* **1993**, *115*, 652; Gronert, S. *J. Am. Chem. Soc.* **1991**, *113*, 6041.
- 6 Merrill, G. N.; Gronert, S.; Kass, S. R. *J. Phys. Chem. A* **1997**, *101*, 208.
- 7 Gronert, S. *J. Org. Chem.* **1995**, *60*, 488.
- 8 Bach, R. D.; Glukhovtsev, M. N.; Gonzalez, C. *J. Am. Chem. Soc.* **1998**, *120*, 9902; Baker, J.; Muir, M.; Andzelm, J. *J. Chem. Phys.* **1995**, *102*, 2063; Barone, V.; Adamo, C. *J. Chem. Phys.* **1996**, *105*, 11007; Gritsenko, O. V.; Ensing, B.; Schipper, P. R. T.; Baerends, E. J. *J. Phys. Chem. A* **2000**, *104*, 8558; Poater, J.; Solà, M.; Duran, M.; Robles, J. *Phys. Chem. Chem. Phys.* **2002**, *4*, 722; Thümmel, H. T.;

- Bauschlicher, C. W. *J. Phys. Chem. A* **1997**, *101*, 1188; Diefenbach, A.; Bickelhaupt, F. M. *J. Chem. Phys.* **2001**, *115*, 4030; Gonzales, J. M.; Cox III, S.; Brown, S. T.; Allen, W. D.; Schaefer III, H. F. *J. Phys. Chem. A* **2001**, *105*, 11327.
- 9 Baker, J.; Pulay, P. *J. Chem. Phys.* **2002**, *117*, 1441.
- 10 Nibbering, N. M. M. *Adv. Phys. Org. Chem.* **1988**, *24*, 1; Nibbering, N. M. M. *Acc. Chem. Res.* **1990**, *23*, 279.
- 11 Bento, A. P.; Solà, M.; Bickelhaupt, F. M. *J. Comput. Chem.* **2005**, *26*, 1497.
- 12 Swart, M.; Solà, M.; Bickelhaupt, F. M. *J. Comput. Chem.* **2007**, *28*, 1551; Swart, M.; Ehlers, A. W.; Lammertsma, K. *Mol. Phys.* **2004**, *102*, 2467; Xu, X.; Goddard III, W. A. *J. Phys. Chem. A* **2004**, *108*, 8495; Gonzales, J. M.; Allen, W. D.; Schaefer III, H. F. *J. Phys. Chem. A* **2005**, *109*, 10613; Gonzales, J. M.; Pak, C.; Cox, R. S.; Allen, W. D.; Schaefer III, H. F.; Császár, A. G.; Tarczay, G. *Chem. Eur. J.* **2003**, *9*, 2173; Galabov, B.; Nikolova, V.; Wilke, J. J.; Schaefer III, H. F.; Allen, W. D. *J. Am. Chem. Soc.* **2008**, *130*, 9887.
- 13 Guner, V. A.; Khuong, K. S.; Houk, K. N.; Chuma, A.; Pulay, P. *J. Phys. Chem. A* **2004**, *108*, 2959.
- 14 Zhao, Y.; Truhlar, D. G. *Acc. Chem. Res.* **2008**, *41*, 157.
- 15 Baerends, E. J.; Autschbach, J.; Bérces, A.; Berger, J. A.; Bickelhaupt, F. M.; Bo, C.; de Boeij, P. L.; Boerrigter, P. M.; Cavallo, L.; Chong, D. P.; Deng, L.; Dickson, R. M.; Ellis, D. E.; van Faassen, M.; Fan, L.; Fischer, T. H.; Fonseca Guerra, C.; van Gisbergen, S. J. A.; Groeneveld, J. A.; Gritsenko, O. V.; Grüning, M.; Harris, F. E.; van den Hoek, P.; Jacob, C. R.; Jacobsen, H.; Jensen, L.; Kadantsev, E. S.; van Kessel, G.; Klooster, R.; Kootstra, F.; van Lenthe, E.; McCormack, D. A.; Michalak, A.; Neugebauer, J.; Nicu, V. P.; Osinga, V. P.; Patchkovskii, S.; Philipsen, P. H. T.; Post, D.; Pye, C. C.; Ravenek, W.; Romaniello, P.; Ros, P.; Schipper, P. R. T.; Schreckenbach, G.; Snijders, J.; Solà, M.; Swart, M.; Swerhone, D.; te Velde, G.; Vernooijs, P.; Versluis, L.; Visscher, L.; Visser, O.; Wang, F.; Wesolowski, T. A.; Van Wezenbeek, E. M.; Wiesenekker, G.; Wolff, S. K.; Woo, T. K.; Yakovlev, A. L.; Ziegler, T.; *ADF2007.01*; SCM: Amsterdam, The Netherlands; Fonseca Guerra, C.; Snijders, J. G.; te Velde, G.; Baerends, E. J. *Theor. Chem. Acc.* **1998**, *99*, 391.
- 16 te Velde, G.; Bickelhaupt, F. M.; Baerends, E. J.; Fonseca Guerra, C.; van Gisbergen, S. J. A.; Snijders, J. G.; Ziegler, T. *J. Comput. Chem.* **2001**, *22*, 931; Baerends, E. J.; Ellis, D. E.; Ros, P. *Chem. Phys.* **1973**, *2*, 41.
- 17 Handy, N. C.; Cohen, A. J. *Mol. Phys.* **2001**, *99*, 403.
- 18 Lee, C.; Yang, W.; Parr, R. G. *Phys. Rev. B* **1988**, *37*, 785.
- 19 Fan, L.; Ziegler, T. *J. Chem. Phys.* **1990**, *92*, 3645.
- 20 Fan, L.; Versluis, L.; Ziegler, T.; Baerends, E. J.; Ravenek, W. *Int. J. Quantum Chem. Quantum Chem. Symp.* **1988**, *S22*, 173.

- 21 Vosko, S. H.; Wilk, L.; Nusair, M. *Can. J. Phys.* **1980**, *58*, 1200.
- 22 Becke, A. D. *Phys. Rev. A* **1988**, *38*, 3098.
- 23 Perdew, J. P. *Phys. Rev. B* **1986**, *33*, 8822.
- 24 Perdew, J. P. In *Electronic Structure of Solids '91*; Ziesche, P., Eschrig, H., Eds.; Akademie Verlag: Berlin, 1991; Perdew, J. P.; Chevary, J. A.; Vosko, S. H.; Jackson, K. A.; Pederson, M. R.; Singh, D. J.; Fiolhais, C. *Phys. Rev. B* **1992**, *46*, 6671 (Erratum: *Ibid.* **1993**, *48*, 4978).
- 25 Perdew, J. P.; Burke, K.; Ernzerhof, M. *Phys. Rev. Lett.* **1996**, *77*, 3865 (Erratum: *Ibid.* **1997**, *78*, 1396).
- 26 Hammer, B.; Hansen, L. B.; Nørskov, J. K. *Phys. Rev. B* **1999**, *59*, 7413.
- 27 Zhang, Y.; Yang, W. *Phys. Rev. Lett.* **1998**, *80*, 890.
- 28 Filatov, M.; Thiel, W. *Mol. Phys.* **1997**, *91*, 847.
- 29 Hamprecht, F. A.; Cohen, A. J.; Tozer, D. J.; Handy, N. C. *J. Chem. Phys.* **1998**, *109*, 6264.
- 30 Boese, A. D.; Doltsinis, N. L.; Handy, N. C.; Sprik, M. *J. Chem. Phys.* **2000**, *112*, 1670.
- 31 Boese, A. D.; Handy, N. C. *J. Chem. Phys.* **2001**, *114*, 5497.
- 32 Tsuneda, T.; Suzumura, T.; Hirao, K. *J. Chem. Phys.* **1999**, *110*, 10664.
- 33 Perdew, J. P.; Kurth, S.; Zupan, A.; Blaha, P. *Phys. Rev. Lett.* **1999**, *82*, 2544 (Erratum: *Ibid.* **1999**, *82*, 5179).
- 34 Van Voorhis, T.; Scuseria, G. E. *J. Chem. Phys.* **1998**, *109*, 400.
- 35 Proynov, E. I.; Sirois, S.; Salahub, D. R. *Int. J. Quantum Chem.* **1997**, *64*, 427.
- 36 Tao, J.; Perdew, J. P. *Phys. Rev. Lett.* **2003**, *91*, 146401; Staroverov, V. N.; Scuseria, G. E.; Tao, J.; Perdew, J. P. *J. Chem. Phys.* **2003**, *119*, 12129 (Erratum: *Ibid.* **2004**, *121*, 11507).
- 37 Zhao, Y.; Truhlar, D. G. *J. Chem. Phys.* **2006**, *125*, 194101.
- 38 Becke, A. D. *J. Chem. Phys.* **1993**, *98*, 5648.
- 39 Cohen, A. J.; Handy, N. C. *Mol. Phys.* **2001**, *99*, 607.
- 40 Kang, J. K.; Musgrave, C. B. *J. Chem. Phys.* **2001**, *115*, 11040.
- 41 Becke, A. D. *J. Chem. Phys.* **1993**, *98*, 1372.
- 42 Toulouse, J.; Adamo, C. *Chem. Phys. Lett.* **2002**, *362*, 72.
- 43 Lynch, B. J.; Fast, P. L.; Harris, M.; Truhlar, D. G. *J. Phys. Chem. A* **2000**, *104*, 4811.
- 44 Zhao, Y.; Schultz, N. E.; Truhlar, D. G. *J. Chem. Phys.* **2005**, *123*, 161103.
- 45 Zhao, Y.; Schultz, N. E.; Truhlar, D. G. *J. Chem. Theory Comput.* **2006**, *2*, 364.
- 46 Zhao, Y.; Truhlar, D. G. *Theor. Chem. Acc.* **2008**, *120*, 215 (Erratum: *Ibid.* **2008**, *119*, 525).

- 47 Swart, M.; Groenhof, A. R.; Ehlers, A. W.; Lammertsma, K. *J. Phys. Chem. A* **2004**, *108*, 5479; de Jong, G. Th.; Bickelhaupt, F. M. *J. Chem. Theory Comput.* **2006**, *2*, 322; de Jong, G. Th.; Bickelhaupt, F. M. *J. Phys. Chem. A* **2005**, *109*, 9685; de Jong, G. Th.; Geerke, D. P.; Diefenbach, A.; Solà, M.; Bickelhaupt, F. M. *J. Comput. Chem.* **2005**, *26*, 1006; de Jong, G. Th.; Geerke, D. P.; Diefenbach, A.; Bickelhaupt, F. M. *Chem. Phys.* **2005**, *313*, 261.
- 48 Frisch, M. J.; Trucks, G. W.; Schlegel, H. B.; Scuseria, G. E.; Robb, M. A.; Cheeseman, J. R.; Montgomery Jr., J. A.; Vreven, T.; Kudin, K. N.; Burant, J. C.; Millam, J. M.; Iyengar, S. S.; Tomasi, J.; Barone, V.; Mennucci, B.; Cossi, M.; Scalmani, G.; Rega, N.; Petersson, G. A.; Nakatsuji, H.; Hada, M.; Ehara, M.; Toyota, K.; Fukuda, R.; Hasegawa, J.; Ishida, M.; Nakajima, T.; Honda, Y.; Kitao, O.; Nakai, H.; Klene, M.; Li, X.; Knox, J. E.; Hratchian, H. P.; Cross, J. B.; Bakken, V.; Adamo, C.; Jaramillo, J.; Gomperts, R.; Stratmann, R. E.; Yazyev, O.; Austin, A. J.; Cammi, R.; Pomelli, C.; Ochterski, J. W.; Ayala, P. Y.; Morokuma, K.; Voth, G. A.; Salvador, P.; Dannenberg, J. J.; Zakrzewski, G.; Dapprich, S.; Daniels, A. D.; Strain, M. C.; Farkas, O.; Malick, D. K.; Rabuck, A. D.; Raghavachari, K.; Foresman, J. B.; Ortiz, J. V.; Cui, Q.; Baboul, A. G.; Clifford, S.; Cioslowski, J.; Stefanov, B. B.; Liu, G.; Liashenko, A.; Piskorz, P.; Komaromi, I.; Martin, R. L.; Fox, D. J.; Keith, T.; Al-Laham, M. A.; Peng, C. Y.; Nanayakkara, A.; Challacombe, M.; Gill, P. M. W.; Johnson, B.; Cheng, W.; Wong, M. W.; Gonzalez, C.; Pople, J. A.; *Gaussian 03*. Gaussian Inc.: Pittsburgh, PA, 2003.
- 49 Møller, C.; Plesset, M. S. *Phys. Rev.* **1934**, *46*, 618.
- 50 Krishnan, R.; Pople, J. A. *Int. J. Quantum Chem.* **1978**, *14*, 91; Krishnan, R.; Frisch, M. J.; Pople, J. A. *J. Chem. Phys.* **1980**, *72*, 4244.
- 51 Cizek, J. *J. Chem. Phys.* **1966**, *45*, 4256.
- 52 Purvis III, G. D.; Barlett, R. J. *J. Chem. Phys.* **1982**, *76*, 1910.
- 53 Raghavachari, K.; Trucks, G. W.; Pople, J. A.; Head-Gordon, M. *Chem. Phys. Lett.* **1989**, *157*, 479.
- 54 Dunning Jr., T. H. *J. Chem. Phys.* **1989**, *90*, 1007; Kendall, R. A.; Dunning Jr., T. H.; Harrison, R. J. *J. Chem. Phys.* **1992**, *96*, 6796; Dunning Jr., T. H.; Peterson, K. A.; Wilson, A. K. *J. Chem. Phys.* **2001**, *114*, 9244; The aug-cc-V(n + d)Z basis set was obtained from the Extensible Computational Chemistry Environment Basis Set Database, Version 02/02/06, as developed and distributed by the Molecular Science Computing Facility, Environmental and Molecular Sciences Laboratory which is part of the Pacific Northwest Laboratory, P.O. Box 999, Richland, Washington 99352, USA, and funded by the U.S. Department of Energy.
- 55 Halkier, A.; Helgaker, T.; Jørgensen, P.; Klopper, W.; Koch, H.; Olsen, J.; Wilson, A. K. *Chem. Phys. Lett.* **1998**, *286*, 243.

5 *Nucleophilic Substitution at Silicon via a Central Reaction Barrier*

Adapted from

Bento, A. P.; Bickelhaupt, F. M. *J. Org. Chem.* **2007**, 72, 2201

Abstract

It is textbook knowledge that nucleophilic substitution at carbon ($S_N2@C$) proceeds via a central reaction barrier, which disappears in the corresponding nucleophilic substitution reaction at silicon ($S_N2@Si$). Here, we address the question why the central barrier disappears from $S_N2@C$ to $S_N2@Si$ despite the fact that these processes are isostructural and isoelectronic. To this end, we have explored and analyzed the potential energy surfaces (PES) of various $Cl^- + CR_3Cl$ ($R = H, CH_3$) and $Cl^- + SiR_3Cl$ model reactions ($R = H, CH_3, C_2H_5$ and OCH_3). Our results show that the nature of the S_N2 reaction barrier is in essence steric, but that it can be modulated by electronic factors. Thus, simply by increasing the steric demand of the substituents R around the silicon atom, the $S_N2@Si$ mechanism changes from its regular single-well PES (with a stable intermediate transition complex, TC), via a triple-well PES (with a pre- and a post-TS before and after the central TC), to a double-well PES (with a TS; $R = OCH_3$), which is normally encountered for $S_N2@C$ reactions.

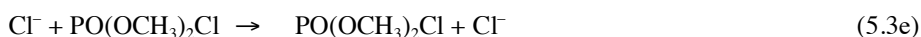
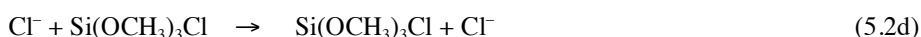
5.1. Introduction

Bimolecular nucleophilic substitution (S_N2) occurs in many synthetic organic approaches¹ and various experimental and theoretical studies have been conducted to explore the potential energy surface (PES) and to understand the nature of this process.² The symmetric, thermoneutral S_N2 reaction between the chloride anion and chloromethane, $Cl^- + CH_3Cl$, in the gas phase is generally employed as the archetypal model for nucleophilic substitution. This reaction proceeds preferentially through a backside nucleophilic attack of the chloride anion at the carbon atom ($S_N2@C$) which goes with concerted expulsion of the leaving group. A well-known feature of gas-phase $S_N2@C$ reactions is their double-well potential energy surface (PES) along the reaction coordinate which is characterized by a central barrier, provided by a trigonal bipyramidal transition state (TS), that separates two pronounced minima, associated with the reactant and product ion–molecule complexes (RC and PC).

The central reaction barrier disappears if we go to nucleophilic substitution at silicon ($S_N2@Si$),³⁻⁷ or other third-period atoms.^{8,9} This is often illustrated with the reactions of $Cl^- + CH_3Cl$ and $Cl^- + SiH_3Cl$: going from the former to the latter the reaction profile changes from a double-well PES, involving a central TS, for substitution at a second-period atom ($S_N2@C$) to a single-well PES associated with a stable trigonal bipyramidal transition *complex* (TC) for substitution at the third-period congener ($S_N2@Si$). In certain instances, the formation of the stable trigonal bipyramidal TC has been found in early *ab initio* computations to proceed via a pre-transition state (pre-TS), for example, in the reactions of $RO^- + SiH_3CH_3$ with $R = H$ and CH_3 .⁶ However, these reaction barriers are not associated with the nucleophilic approach of RO^- toward Si. They rather originate from the energy-demanding return of a proton to the carbanion in the encounter complex $[ROH\cdots CH_2SiH_3]$ which is formed, at first, after spontaneous proton transfer from the methyl substituent in the substrate to the nucleophile.⁶

Thus, nucleophilic substitution at carbon ($S_N2@C$) proceeds via a central reaction barrier which disappears in the corresponding nucleophilic substitution reaction at silicon ($S_N2@Si$). While this phenomenon as such is well known, it is still not fully understood. The above $S_N2@C$ and $S_N2@Si$ substitutions are structurally equivalent and isoelectronic. *Why*, then, does the central reaction barrier disappear if we go from $S_N2@C$ to the corresponding $S_N2@Si$ process? And what causes the existence of a central barrier for $S_N2@C$ in the first place? Is there an electronic factor responsible for the barrier in the case of $S_N2@C$ (e.g., less favorable bonding capability of carbon as compared to silicon) or is this barrier, as hypothesized by Dewar and Healy,⁵ steric in origin, i.e., caused by repulsion between substituents around the smaller carbon atom?

To answer these questions, we have systematically analyzed and compared a series of archetypal $S_N2@C$ and $S_N2@Si$ reactions using the ADF program at OLYP/TZ2P.^{10,11} This level of theory was previously shown to agree within a few kcal/mol with highly correlated *ab initio* benchmarks.⁴ Our model systems cover nucleophilic substitutions at carbon in CR_3Cl (eqs 5.1) and silicon in SiR_3Cl (eqs 5.2) with various substituents $R = H, CH_3, C_2H_5$ and OCH_3 that range from small to sterically more demanding. For comparison, we include into our discussion the nucleophilic substitutions at phosphorus ($S_N2@P$) shown in eqs 5.3, previously studied by van Bochove *et al.*⁸



Our analyses reveal that steric congestion around carbon is indeed the origin of the barrier of $S_N2@C$ reactions and that reduced steric repulsion around the larger silicon atom of a corresponding $S_N2@Si$ reaction is the main reason for the disappearance of this central S_N2 barrier. Prompted by this finding, we have attempted to let the central reaction barrier reappear in the $S_N2@Si$ reaction. As will become clear, later on, this attempt has been successful. We show how simply increasing the steric congestion at silicon shifts the $S_N2@Si$ mechanism stepwise back from a single-well potential (with a stable central TC) that is common for substitution at third-period atoms, via a triple-well potential (featuring a pre- and post-TS before and after the central TC), back to the double-well potential (with a central TS!) that is well-known for substitution at carbon but unprecedented for substitution at silicon.

5.2. Methods

5.2.1. Computational Details

All calculations were carried out with the Amsterdam Density Functional (ADF) program developed by Baerends and others.^{10,11} The molecular orbitals (MOs) were expanded in a large uncontracted set of Slater-type orbitals (STOs) containing diffuse functions, TZ2P. The TZ2P basis set is of triple- ζ quality and has been augmented with two sets of polarization functions: $2p$ and $3d$ on hydrogen, $3d$ and $4f$ on carbon, silicon, chlorine and oxygen. The core shells of carbon ($1s$), silicon ($1s2s2p$), chlorine ($1s2s2p$) and oxygen ($1s$) were treated by the frozen-core approximation.¹¹ An auxiliary set of s , p , d , f and g STOs was used to fit the molecular density and to represent the Coulomb and exchange potentials accurately in each SCF cycle.

Energies and geometries were computed with the OLYP¹² density functional which involves Handy's optimized exchange, OPTX. Previous studies have shown that OLYP reaction profiles agree satisfactorily with highly correlated *ab initio* benchmarks.^{4,13} All stationary points were confirmed to be equilibrium structures (no imaginary frequencies) or a transition state¹⁴ (one imaginary frequency) through vibrational analysis.¹⁵ Furthermore, transition states were verified to connect the supposed reactant and product minima by carrying out intrinsic reaction coordinate (IRC) calculations.¹⁶

5.2.2. Analysis of the Potential Energy Surfaces

Insight into how the activation barriers arise was obtained using the Activation Strain model of chemical reactivity (see Chapter 2). In this model, the potential energy surface $\Delta E(\zeta)$ is decomposed, along the reaction coordinate ζ , into the strain $\Delta E_{\text{strain}}(\zeta)$ associated with deforming the individual reactants, plus the actual interaction $\Delta E_{\text{int}}(\zeta)$ between the deformed reactants:

$$\Delta E(\zeta) = \Delta E_{\text{strain}}(\zeta) + \Delta E_{\text{int}}(\zeta) \quad (5.4)$$

The strain $\Delta E_{\text{strain}}(\zeta)$ is determined by the rigidity of the reactants and on the extent to which groups must reorganize in a particular reaction mechanism, whereas the interaction $\Delta E_{\text{int}}(\zeta)$ between the reactants depends on their electronic structure and on how they are mutually oriented as they approach each other. In the present study, the reactants are the nucleophile Cl^- and either one of the substrates CR_3Cl or SiR_3Cl .

5.3. Results and Discussion

5.3.1. Potential Energy Surfaces

The results of our OLYP/TZ2P computations are collected in Figure 5.1 (geometries) and Table 5.1 (energies). In the case of $R = H$, we recover the well-known change from a double-well PES with a central barrier and TS for $S_N2@C$ (eq 5.1a) to a single-well PES for $S_N2@Si$ (eq 5.2a) in which the pentavalent transition species has turned from a TS into a stable TC. The reactant complex (RC) of the $S_N2@C$ reaction is bound by 9.0 kcal/mol, and it is separated from the product complex (PC) by a central barrier of 8.9 kcal/mol. The $S_N2@Si$ reaction features only a stable pentacoordinate TC (no TS, RC, PC) at -24.4 kcal/mol. Previously, van Bochove *et al.*⁸ have shown that the PES of the $S_N2@P$ reaction can be turned back from single-well (with a stable transition complex, TC) to double-well (with central transition state, TS) by increasing the steric demand of the substituents (see, for example, eqs 5.3 and the PES data in Table 5.1). This suggests that also $S_N2@Si$ reactions may proceed via a double-well PES provided that substituents at silicon are sufficiently bulky.

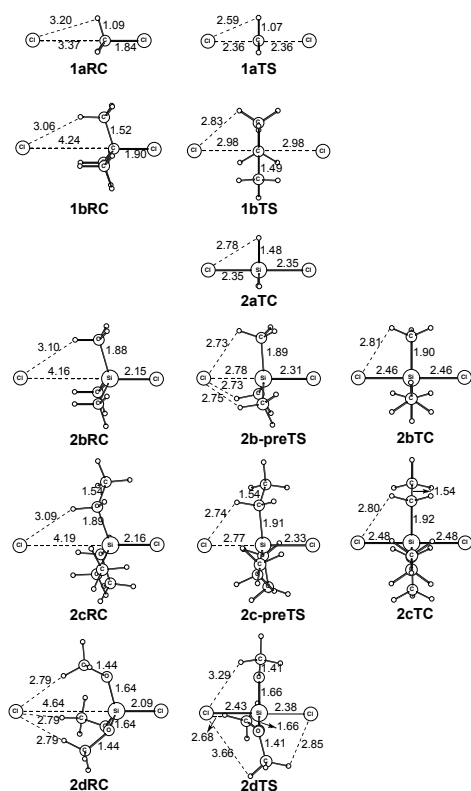


Figure 5.1. Structures (in Å; at OLYP/TZ2P) of selected stationary points for $S_N2@C$ and $S_N2@Si$ reactions.

Thus, we have probed the effect of replacing hydrogen by methyl or larger substituents R in the $S_N2@Si$ (eqs 5.2) and, for comparison, the $S_N2@C$ reactions (eqs 5.1). In the case of the latter, increasing the steric congestion at carbon causes an enormous increase of the central barrier: going from hydrogen (eq 5.1a) to methyl substituents (eq 5.1b) pushes the central barrier up from 8.9 to 26.0 kcal/mol (see Table 5.1). The PES of the more bulky $S_N2@C$ reaction (eq 5.1b) remains double-well, with pronounced minima for RC and PC which are even slightly more stable (-11.6 kcal/mol) than those of the simple $Cl^- + CH_3Cl$ reaction (-9.0 kcal/mol; see Table 5.1 and Figure 5.1).

Table 5.1. Energies (in kcal/mol) relative to reactants of stationary points occurring in $S_N2@C$, $S_N2@Si$ and $S_N2@P$ reactions.^a

| no. | Reaction | shape of PES ^b | RC | preTS | TS/TC |
|-------------------|-------------------------|---------------------------|-------|-------|-------|
| 5.1a | $Cl^- + CH_3Cl$ | double well | -9.0 | - | -0.1 |
| 5.1b | $Cl^- + C(CH_3)_3Cl$ | double well | -11.6 | - | 14.4 |
| 5.2a | $Cl^- + SiH_3Cl$ | single well | - | - | -24.4 |
| 5.2b | $Cl^- + Si(CH_3)_3Cl$ | triple well | -12.3 | -9.1 | -9.5 |
| 5.2c | $Cl^- + Si(C_2H_5)_3Cl$ | triple well | -12.8 | -10.0 | -10.7 |
| 5.2d | $Cl^- + Si(OCH_3)_3Cl$ | double well | -12.0 | - | -1.2 |
| 5.3a ^c | $Cl^- + PH_2Cl$ | single well | - | - | -26.2 |
| 5.3b ^c | $Cl^- + P(CH_3)_2Cl$ | triple well | -13.0 | -12.7 | -15.6 |
| 5.3c ^c | $Cl^- + POH_2Cl$ | single well | - | - | -22.3 |
| 5.3d ^c | $Cl^- + PO(CH_3)_2Cl$ | double well | -16.2 | - | -5.7 |
| 5.3e ^c | $Cl^- + PO(OCH_3)_2Cl$ | double well | -14.1 | - | 2.5 |

^aComputed at OLYP/TZ2P; see Figure 5.1 for selected structures. ^bShape of potential energy surface: either single-well (no TS), triple-well (two TSs), or double-well (one central TS). ^cFrom Ref. 8

In the case of the corresponding $S_N2@Si$ reactions, the introduction of the more bulky methyl substituents from reaction 5.2a to 5.2b causes the occurrence of a new feature on the PES, namely, pre- and post-transition states that surround the central, pentavalent transition species **2bTC** (see Table 5.1 and Figure 5.1). The latter is again destabilized with respect to the transition complex **2aTC** in the corresponding reaction involving hydrogen substituents (eq 5.2a). However, **2bTC** is still a stable, intermediate complex, that is, it does not turn into a transition state. This finding is consistent with the results of Damrauer and coworkers⁷ who also found the $[ClSi(CH_3)_3Cl]^-$ species to be a stable siliconate intermediate. Note that in this respect, the $S_N2@Si$ reactions of $Cl^- + SiR_3Cl$ differ from the corresponding $S_N2@P$ reactions of $Cl^- + POR_3Cl$ which show already a double-well PES with a central TS for $R = CH_3$ (see Table 5.1).⁸ Note however also that the pre- and post-barriers separating the stable **2bTC** from reactant and product complexes of reaction 2b are relatively small, only 0.4 kcal/mol (Table 5.1).

Interestingly, this suggests that further increasing the steric bulk of the substituents R in SiR_3Cl may eventually lead to a merging of the pre- and post-TS and a change from a triple-well to a double-well PES with a central, trigonal bipyramidal TS, also in the case of the $S_N2@Si$ reactions. The change from triple- to double-well PES does not yet occur if we go from methyl (eq 5.2b) to ethyl substituents (eq 5.2c). Thus, in the reaction of $Cl^- + Si(C_2H_5)_3Cl$ (eq 5.2c), the RC, the preTS as well as the TC are only slightly stabilized by 0.5 kcal/mol, 0.9 kcal/mol and 1.2 kcal/mol, respectively (Table 5.1).

The introduction of methoxy substituents (eq 5.2d) finally causes the pre- and post-TS to merge into one central TS that occurs at the trigonal bipyramidal transition structure **2dTS** (see Table 5.1 and Figure 5.1). Our analyses reveal that this originates from a further increase of steric repulsion around the congested pentacoordinate silicon (vide infra). Thus, we arrive at a RC and PC that are each bound by -12.0 kcal/mol and

separated by a central barrier of +10.8 kcal/mol. In **2dTS**, one methoxy group is within the numerical precision symmetrically oriented between nucleophile and leaving group whereas the other two methoxy groups point either slightly to the nucleophile or the leaving group, respectively (see Figure 5.1). A full IRC analysis without any symmetry restriction confirms that **2dTS** is indeed the first-order saddle point that connects **2dRC** and **2dPC** on the multidimensional PES.

To the best of our knowledge, this is the first example of an $S_N2@Si$ reaction that proceeds via the classical double-well potential. Figure 5.2 illustrates how the increasing steric demand of the substituents R in the substrate SiR_3Cl , along $R = H, CH_3, C_2H_5$ and OCH_3 in reactions 5.2a-d, first causes the occurrence of steric pre- and post-barriers ($R = CH_3$ and C_2H_5) which eventually merge into one central barrier ($R = OCH_3$).

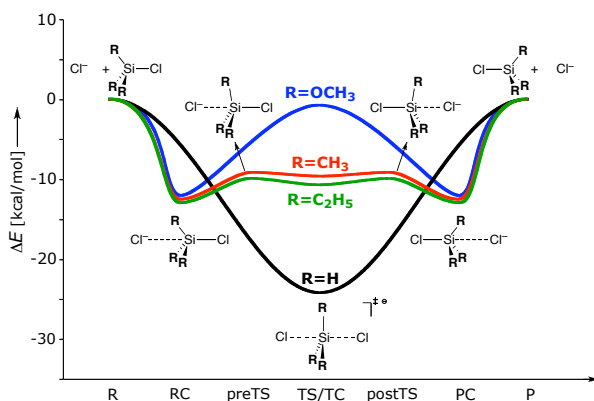


Figure 5.2. Potential energy surfaces ΔE along the reaction coordinate of the $S_N2@Si$ reactions of $Cl^- + SiR_3Cl$ for $R = H, CH_3, C_2H_5$ and OCH_3 , computed at OLYP/TZ2P.

5.3.2. Activation Strain Analyses of the Model Reactions

Next, we address the steric nature of the various S_N2 reaction barriers that was already mentioned in the discussion above. The insight that these barriers are in most cases steric, emerges from our Activation Strain analyses (see Chapter 2) in which the potential energy surface $\Delta E(\xi)$ of the model reactions is decomposed, along the reaction coordinate ξ , into the strain $\Delta E_{\text{strain}}(\xi)$ associated with deforming the individual reactants plus the actual interaction $\Delta E_{\text{int}}(\xi)$ between the deformed reactants (eq 5.4; for details, see also Chapter 2). The results of the Activation Strain analyses are collected in Figure 5.3 in which we show the S_N2 potential energy surface $\Delta E(\xi)$ (left panel), its decomposition into $\Delta E_{\text{strain}}(\xi) + \Delta E_{\text{int}}(\xi)$ (middle panel), and the decomposition of the nucleophile–substrate interactions $\Delta E_{\text{int}}(\xi)$ (right panel) of $Cl^- + CH_3Cl$ (5.1a), SiH_3Cl (5.2a), $Si(CH_3)_3Cl$ (5.2b), $Si(C_2H_5)_3Cl$ (5.2c) and $Si(OCH_3)_3Cl$ (5.2d).

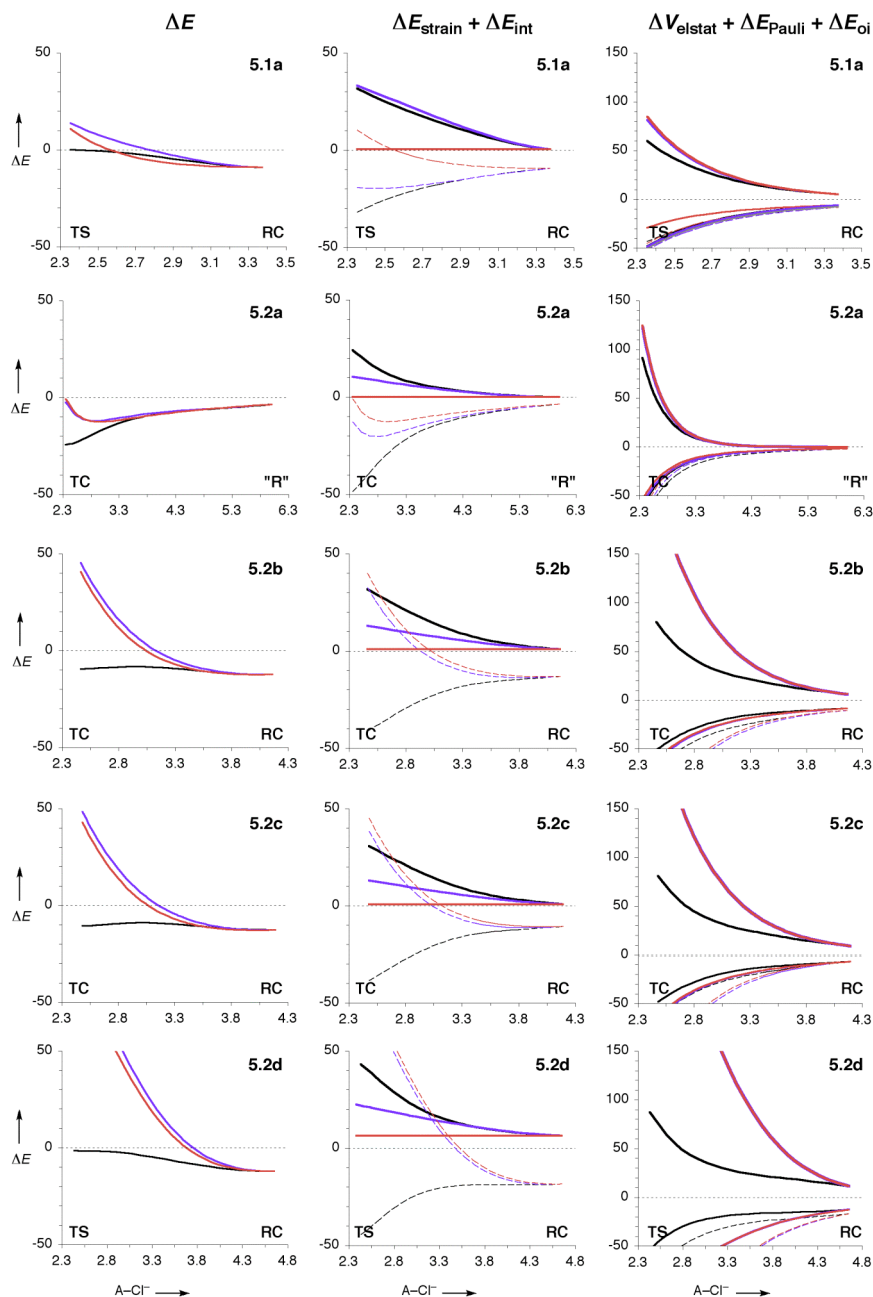


Figure 5.3. Analysis of the potential energy surfaces ΔE (in kcal/mol) of the S_N2 reactions of $Cl^- + CH_3Cl$ (eq 5.1a) and $Cl^- + SiR_3Cl$ for $R = H$ (5.2a), CH_3 (5.2b), C_2H_5 (5.2c) and $OCCH_3$ (5.2d) along the reaction coordinate projected onto the Cl^- -Si (or Cl^- -C) distance (in Å). Left panel: Potential energy surfaces ΔE . Middle panel: Activation Strain analysis of the potential energy surfaces $\Delta E = \Delta E_{\text{strain}}$ (bold lines) + ΔE_{int} (dashed lines). Right panel: energy decomposition of the nucleophile-substrate interaction $\Delta E_{\text{int}} = \Delta V_{\text{elstat}}$ (dashed lines) + ΔE_{Pauli} (bold lines) + ΔE_{oi} (plain lines). **Black lines:** model of the regular internal reaction coordinate (IRC). **Blue lines:** model IRC with geometry of $[CH_3]$ or $[SiR_3]$ unit in substrate frozen to that in the reactant complex (RC) or reactants ("R"). **Red lines:** model IRC with geometry of entire substrate frozen to that in the RC or "R".

For each reaction, three situations are analyzed, which are distinguished in the illustrations by a color code: black, blue and red curves. The black lines refer to the regular internal reaction coordinate (IRC). Here, the IRC is modeled by a linear transit in which the nucleophile–central-atom distance and the central-atom–leaving-group distance run synchronously from their value in the RC to that in the central transition structure, TS or TC, in 50 steps. All other geometrical degrees of freedom are fully optimized at each step. This approach was used because it can be applied to both, reactions with and without central barrier. Moreover, we have verified for $\text{Cl}^- + \text{CH}_3\text{Cl}$ that this model IRC yields a reaction profile that is essentially indistinguishable from that of a full IRC calculation. In those instances, in which no RC exists, the model IRC runs from a geometry that closely resembles the separate reactants ("R") to the TC, where "R" is defined by a nucleophile–central-atom distance of 6 Å and the central-atom–leaving-group distance in the equilibrium structure of the substrate. Next, the analyses represented in blue lines refer to the situation in which the geometry of the substrate is kept frozen to its geometry in the RC (or "R"), except for the central-atom–leaving-group distance and relative orientation, i.e., the $[\text{CH}_3]$ or $[\text{SiR}_3]$ moiety is frozen but the leaving group still departs as the nucleophile approaches. The red lines, finally, refer to analyses in which the entire substrate is frozen to the geometry it adopts in the RC or to its equilibrium geometry ("R").

5.3.2.1. Nucleophilic Substitution at Carbon

First, we analyze the $\text{S}_{\text{N}}2@C$ of $\text{Cl}^- + \text{CH}_3\text{Cl}$ (eq 5.1a). As the reaction progresses from the RC to the TS, the energy ΔE rises from -9 to 0 kcal/mol (black line in Figure 5.3, left panel; see also Table 5.1). In terms of the Activation Strain model this is so because the stabilization from the nucleophile–substrate interaction ΔE_{int} is not sufficiently stabilizing to compensate the strain ΔE_{strain} that is building up in the substrate (bold black line in Figure 5.3, middle panel).

The origin of this build-up of strain turns out to be steric congestion around the carbon atom of the substrate. This congestion induces a structural deformation in the substrate that partially relieves the steric repulsion (see also Ref. 8). The nucleophile–substituent ($\text{Cl}-\text{H}$) distance in **1aTS** is only 2.59 Å, significantly shorter than the 3.20 Å in **1aRC** (see Figure 5.1). This distance would be even shorter if the H substituents would not bend away yielding a planar CH_3 moiety in the TS. Indeed, if we freeze the $[\text{CH}_3]$ moiety in its pyramidal geometry of the RC, the energy ΔE goes up by 14 kcal/mol at the TS (compare blue and black curves in Figure 5.3, left 5.1a). This is nearly entirely due to a reduction by 12 kcal/mol in the nucleophile–substrate interaction ΔE_{int} (compare blue and black dashed lines in Figure 5.3, middle 5.1a). The reason that ΔE_{int} is substantially weakened appears to be a substantial rise in Pauli repulsion between the Cl^-

3p AOs and C–H bonding orbitals on CH₃Cl (see rise from black to blue bold lines in Figure 5.3, right 5.1a). The bonding orbital interactions ΔE_{oi} as well as the electrostatic attraction ΔV_{elstat} are hardly affected.

The build-up of substrate strain can only be avoided by completely freezing the substrate to the geometry it adopts in the RC, in which case the carbon–leaving-group distance remains fixed at the short value of 1.84 Å (see **1aRC** in Figure 5.1). One might expect the barrier on the PES to collapse as the strain at the TS drops by some 30 kcal/mol to practically¹⁷ zero (see red bold line in Figure 5.3, middle 5.1a). But this is not the case. The barrier goes down by only 3 kcal/mol compared to the partially frozen situation! This is because the nucleophile–substrate interaction ΔE_{int} (which is now approximately equal to ΔE) is enormously destabilized and even becomes repulsive near the TS (compare red and blue dashed lines in Figure 5.3, middle 5.1a). The reason is not a further increase of the Pauli repulsion which remains practically unchanged (red and blue bold lines nearly coincide in Figure 5.3, right 5.1a). This is what one would expect as the steric appearance of the substrate, i.e., the frozen CH₃ moiety, is the same in both simulations. The destabilization in ΔE_{int} can be traced to a comparable loss in bonding orbital interactions ΔE_{oi} (compare red and blue plain lines in Figure 5.3, right 5.1a). The origin is that the donor–acceptor interaction between the Cl[−] 3p AO and the CH₃Cl σ^*_{C-Cl} LUMO normally (black but also blue lines) induces an elongation in the carbon–leaving group bond which amplifies this stabilizing interaction because it leads to a lowering of the σ^*_{C-Cl} orbital and thus a smaller, i.e., more favorable HOMO–LUMO gap. This effect has been switched off by not allowing the carbon–leaving-group bond to expand. The orbital interactions still increase as the nucleophile approaches because the $\langle 3p | \sigma^*_{C-Cl} \rangle$ overlap increases, but they do so much less efficiently than when the carbon–leaving-group bond is free to expand.

5.3.2.2. Nucleophilic Substitution at Silicon

The above results suggest that by decreasing the steric congestion at the central atom and by strengthening the nucleophile–substrate interaction, one can let the S_N2 central barrier disappear. And this is exactly what happens if we go from Cl[−] + CH₃Cl (5.1a) to the S_N2@Si reaction of Cl[−] + SiH₃Cl (5.2a). The TS turns into a stable pentacoordinate TC (vide supra) because both the strain and interaction curves are significantly stabilized: at the transition structure, ΔE_{strain} decreases from 32 to 24 kcal/mol and ΔE_{int} goes from −32 to −49 kcal/mol (Figure 5.3: compare black bold lines in 5.1a and 5.2a middle).

Despite these obvious differences, the strain and interaction curves of the S_N2@Si reaction of Cl[−] + SiH₃Cl (5.2a) have still the same origin as in the case of the S_N2@C reaction of Cl[−] + CH₃Cl (5.1a). The strain still originates from steric repulsion between the approaching nucleophile and the substituents around the silicon atom which is

partially relieved by structural deformation of the substrate. Thus, if we freeze the $[\text{SiH}_3]$ moiety in its pyramidal geometry in the reactants "R" (i.e., in free SiH_3Cl), the energy ΔE rises by 22 kcal/mol at the TC (Figure 5.3: compare blue and black curves in 5.2a left). This occurs despite a drop in strain that results from switching off the planarization of $[\text{SiH}_3]$ (Figure 5.3: compare black bold lines in 5.1a and 5.2a middle) and is exclusively caused by a weakening in the nucleophile–substrate interaction ΔE_{int} by 35 kcal/mol at the TC (Figure 5.3: compare blue and black dashed lines in 5.2a middle). The reason that ΔE_{int} is substantially weakened appears to be again the substantial rise in steric (Pauli) repulsion between the Cl^- $3p$ AOs and Si-H bonding orbitals on SiH_3Cl (Figure 5.3: see rise from black to blue bold lines in 5.1a right). The bonding orbital interactions ΔE_{oi} as well as the electrostatic attraction ΔV_{elstat} are much less affected by freezing the $[\text{SiH}_3]$ moiety.

Freezing the entire substrate SiH_3Cl in its equilibrium geometry has not much effect on the PES ΔE . This behavior as well as its origin is again similar to that for the $\text{S}_{\text{N}}2@C$ reaction 5.1a: on one hand, the strain ΔE_{strain} to collapse to zero but, at the same time, the nucleophile–substrate interaction ΔE_{int} is destabilized by a comparable amount (see Figure 5.3: compare red and blue lines in 5.2a middle). The origin of the weakening in ΔE_{int} is that the donor–acceptor interaction between the Cl^- $3p$ AO and the SiH_3Cl $\sigma^*_{\text{Si-Cl}}$ LUMO normally (Figure 5.3: black and blue plain lines in 5.2a right) benefits from the elongation in the silicon–leaving group bond which amplifies this stabilizing interaction because it leads to a lowering of the $\sigma^*_{\text{Si-Cl}}$ orbital and thus a smaller, i.e., more favorable HOMO–LUMO gap. This effect has been switched off by not allowing the silicon–leaving-group bond to expand.

5.3.2.3. Introducing Bulky Substituents

Thus, from $\text{S}_{\text{N}}2@C$ reaction 5.1a to $\text{S}_{\text{N}}2@Si$ reaction 5.2a, the central barrier disappears because the steric congestion at the larger silicon atom is reduced, and because the nucleophile–substrate interaction in the latter is more favorable. This suggests that, as observed above, $\text{S}_{\text{N}}2@Si$ substitution of $\text{Cl}^- + \text{SiR}_3\text{Cl}$ may be turned into a process that proceeds via a double-well PES with a central barrier, similar to $\text{S}_{\text{N}}2@C$ reactions, simply by sufficiently increasing the steric bulk of the substituents R.

The steric congestion at the central atom and, indeed, the similarity with the $\text{S}_{\text{N}}2@C$ reaction (5.1a) increase along the $\text{S}_{\text{N}}2@Si$ reactions of $\text{Cl}^- + \text{SiH}_3\text{Cl}$ (5.2a), $\text{Si}(\text{CH}_3)_3\text{Cl}$ (5.2b) and $\text{Si}(\text{C}_2\text{H}_5)_3\text{Cl}$ (5.2c). Introducing the more bulky methyl or ethyl substituents tremendously boosts the Pauli repulsion ΔE_{Pauli} in the fictitious process in which the $[\text{SiR}_3]$ moiety is kept frozen pyramidal in reactions 5.2b and 5.2c if compared to the corresponding process with a frozen $[\text{SiH}_3]$ unit in reaction 5.2a (Figure 5.3: compare blue bold lines in right 5.2b,c vs. 5.2a). Note that the differences between reactions 5.2b

and 5.2c are comparatively small. Apparently, methyl and ethyl substituents have a similar steric demand in the vicinity of the central atom to which our monoatomic nucleophile approaches. Pauli repulsion is converted into substrate strain in the real $S_N2@Si$ processes 5.2b and 5.2c, in which the substrate deformation is not suppressed (Figure 5.3: compare black and blue bold lines in middle and right 5.2b and 5.2c). Thus, from reaction 5.2a to reactions 5.2b and 5.2c, the strain at the TC increases strongly from 24 to some 32 kcal/mol. This destabilizing effect is further reinforced by a weakening in the nucleophile–substrate interaction ΔE_{int} from -49 kcal/mol for reaction 5.2a to ca. -40 kcal/mol for reactions 5.2b and 5.2c. The increased steric repulsion (converted into substrate strain) from reaction 5.2a to 5.2b and 5.2c causes the pre- and post-barriers mentioned above to lift off from the PES. The transition structure is also destabilized, from -24 to ca. -10 kcal/mol, but it still remains a stable TC (see Table 5.1). Thus, we arrive at a triple-well PES for reactions 5.2b and 5.2c featuring pre- and post-barriers that separate the stable pentavalent TC from reactant and product complexes.

In the case of $S_N2@P$ substitution at tetracoordinate phosphorus, going from hydrogen (reaction 5.3c) to methyl substituents (reaction 5.3d) is already sufficient to let the pre- and post-barrier merge into one central barrier and, thus, to arrive at a double-well PES (see Table 5.1). This is consistent with the fact that the phosphorus atom is slightly smaller and therefore more sensitive to steric congestion than the silicon atom. For example, in the TC of $Cl^- + POH_2Cl$ (5.3c), the Pauli repulsion between the reactants is 104 kcal/mol while in the TC of $Cl^- + SiH_3Cl$ (5.2a), this value is only 91 kcal/mol (compare Figure 5.3 with Figure 3 in Ref. 8).

Finally, going from methyl or ethyl substituents R in $Cl^- + SiR_3Cl$ (5.2b, 5.2c) to methoxy substituents in $Cl^- + Si(CH_3O)_3Cl$ (5.2d), the steric bulk becomes sufficiently large to outweigh the favorable nucleophile–substrate interaction and to bring back the double-well potential with a central S_N2 barrier. The Pauli repulsion ΔE_{Pauli} in the fictitious process in which the $[SiR_3]$ moieties are kept frozen pyramidal jumps from 214 (5.2b) or 229 (5.2c) to 411 kcal/mol (5.2d) at the transition structure. In fact, the ΔE_{Pauli} curve of the latter $S_N2@Si$ (5.2d) runs, already early, of the scale in the illustration: compare blue (behind red) bold lines in Figure 5.3, right 5.2d vs. 5.2c. The increased Pauli repulsion translates again into a higher strain energy in the real, unconstrained $S_N2@Si$ reaction 5.2d (Figure 5.3, middle 5.2d). The nucleophile–substrate interaction does not change that much from 5.2c to 5.2d. Thus, the increased steric bulk forces the central reaction barrier to reappear in this $S_N2@Si$ substitution.

5.4. Conclusions

The central barrier in S_N2 reactions is determined by the interplay of steric and electronic effects, such as, Pauli repulsion between the substituents (including nucleophile and leaving group) at the central atom and donor–acceptor orbital interactions between nucleophile and substrate. From $S_N2@C$ in $Cl^- + CH_3Cl$ to $S_N2@Si$ in $Cl^- + SiH_3Cl$, the central barrier disappears because there is less steric congestion and a more favorable interaction. But the central barrier reappears as the steric bulk around the silicon atom is raised along the model reactions $Cl^- + SiH_3Cl$, $Si(CH_3)_3Cl$ and $Si(OCH_3)_3Cl$. To the best of our knowledge, this is the first example of an $S_N2@Si$ reaction that proceeds via the classical double-well potential with a central reaction barrier. Our results highlight, once more,⁸ the steric nature of the S_N2 barrier in general.¹⁸

References

- 1 Smith, M. B.; March, J. *March's Advanced Organic Chemistry: Reactions, Mechanisms, and Structure*; Wiley: New York, 2007.
- 2 Vayner, G.; Houk, K. N.; Jorgensen, W. L.; Brauman, J. I. *J. Am. Chem. Soc.* **2004**, *126*, 9054; Gronert, S. *Acc. Chem. Res.* **2003**, *36*, 848; Laerdahl, J. K.; Uggerud, E. *Int. J. Mass Spectrom.* **2002**, *214*, 277; Chabinye, M. L.; Craig, S. L.; Regan, C. K.; Brauman, J. I. *Science* **1998**, *279*, 1882; Deng, L.; Branchadell, V.; Ziegler, T. *J. Am. Chem. Soc.* **1994**, *116*, 10645; Shaik, S. S.; Schlegel, H. B.; Wolfe, S. *Theoretical Aspects of Physical Organic Chemistry: The S_N2 Mechanism*; Wiley: New York, 1992; Olmstead, W. N.; Brauman, J. I. *J. Am. Chem. Soc.* **1977**, *99*, 4219; Glukhovtsev, M. N.; Pross, A.; Radom, L. *J. Am. Chem. Soc.* **1995**, *117*, 2024; Botschwina, P. *Theor. Chem. Acc.* **1998**, *99*, 426; Harder, S.; Streitwieser, A.; Petty, J. T.; Schleyer, P. v. R. *J. Am. Chem. Soc.* **1995**, *117*, 3253; Chandrasekhar, J.; Smith, S. F.; Jorgensen, W. L. *J. Am. Chem. Soc.* **1985**, *107*, 154; Lee, I.; Kim, C. K.; Sohn, C. K.; Li, H. G.; Lee, H. W. *J. Phys. Chem. A* **2002**, *106*, 1081; Bickelhaupt, F. M. *J. Comput. Chem.* **1999**, *20*, 114; Nibbering, N. M. M. *Acc. Chem. Res.* **1990**, *23*, 279; DePuy, C. H.; Gronert, S.; Mulin, A.; Bierbaum, V. M. *J. Am. Chem. Soc.* **1990**, *112*, 8650.
- 3 Elschenbroich, C. *Organometallics*; Wiley-VCH: Weinheim, Germany, 2006; Sommer, L. H. *Stereochemistry, Mechanism and Silicon*; McGraw-Hill: New York, 1965; Holmes, R. R. *Chem. Rev.* **1990**, *90*, 17; Damrauer, R.; Hankin, J. A. *Chem. Rev.* **1995**, *95*, 1137; Windus, T. L.; Gordon, M. S.; Davis, L. P.; Burggraf, L. W. *J. Am. Chem. Soc.* **1994**, *116*, 3568; Gronert, S.; Glaser, R.; Streitwieser, A. *J. Am.*

- Chem. Soc.* **1989**, *111*, 3111; DePuy, C. H.; Bierbaum, V. M.; Grabowski, J. J.; King, G. K.; Schmitt, R. J.; Sullivan, S. A. *J. Am. Chem. Soc.* **1980**, *102*, 5012; Méndez, F.; Romero, M. D. L.; Gazquez, J. L. *J. Chem. Sci.* **2005**, *117*, 525; Hilderbrandt, R. L.; Homer, G. D.; Boudjouk, P. *J. Am. Chem. Soc.* **1976**, *98*, 7476; Hao, C.; Kaspar, J. D.; Check, C. E.; Lobring, K. C.; Gilbert, T. M.; Sunderlin, L. S. *J. Phys. Chem. A* **2005**, *109*, 2026; Shi, Z.; Boyd, R. J. *J. Phys. Chem.* **1991**, *95*, 4698; Bowie, J. H. *Acc. Chem. Res.* **1980**, *13*, 76; van der Wel, H.; Nibbering, N. M. M.; Sheldon, J. C.; Hayes, R. N.; Bowie, J. H. *J. Am. Chem. Soc.* **1987**, *109*, 5823; Couzijn, E. P. A.; Ehlers, A. W.; Schakel, M.; Lammertsma, K. *J. Am. Chem. Soc.* **2006**, *128*, 13634.
- 4 Bento, A. P.; Solà, M.; Bickelhaupt, F. M. *J. Comput. Chem.* **2005**, *26*, 1497.
- 5 Dewar, M. J. S.; Healy, E. *Organometallics* **1982**, *1*, 1705.
- 6 Sheldon, J. C.; Hayes, R. N.; Bowie, J. H. *J. Am. Chem. Soc.* **1984**, *106*, 7711.
- 7 Damrauer, R.; Burggraf, L. W.; Davis, L. P.; Gordon, M. S. *J. Am. Chem. Soc.* **1988**, *110*, 6601.
- 8 van Bochove, M. A.; Swart, M.; Bickelhaupt, F. M. *J. Am. Chem. Soc.* **2006**, *128*, 10738.
- 9 Fish, C.; Green, M.; Kilby, R. J.; Lynam, J. M.; McGrady, J. E.; Pantazis, D. A.; Russell, C. A.; Whitwood, A. C.; Willans, C. E. *Angew. Chem.* **2006**, *118*, 3710; Lahiri, S. D.; Zhang, G.; Dunaway-Mariano, D.; Allen, K. N. *Science* **2003**, *299*, 2067; Sølling, T. I.; Pross, A.; Radom, L. *Int. J. Mass Spectrom.* **2001**, *210*, 1; Bachrach, S. M.; Mulhearn, D. C. *J. Phys. Chem.* **1996**, *100*, 3535; Bachrach, S. M.; Gailbreath, B. D. *J. Org. Chem.* **2001**, *66*, 2005; Mulhearn, D. C.; Bachrach, S. M. *J. Am. Chem. Soc.* **1996**, *118*, 9415.
- 10 Baerends, E. J.; Autschbach, J.; Bérces, A.; Berger, J. A.; Bickelhaupt, F. M.; Bo, C.; de Boeij, P. L.; Boerrigter, P. M.; Cavallo, L.; Chong, D. P.; Deng, L.; Dickson, R. M.; Ellis, D. E.; van Faassen, M.; Fan, L.; Fischer, T. H.; Fonseca Guerra, C.; van Gisbergen, S. J. A.; Groeneveld, J. A.; Gritsenko, O. V.; Grüning, M.; Harris, F. E.; van den Hoek, P.; Jacob, C. R.; Jacobsen, H.; Jensen, L.; Kadantsev, E. S.; van Kessel, G.; Klooster, R.; Kootstra, F.; van Lenthe, E.; McCormack, D. A.; Michalak, A.; Neugebauer, J.; Nicu, V. P.; Osinga, V. P.; Patchkovskii, S.; Philipsen, P. H. T.; Post, D.; Pye, C. C.; Ravenek, W.; Romaniello, P.; Ros, P.; Schipper, P. R. T.; Schreckenbach, G.; Snijders, J.; Solà, M.; Swart, M.; Swerhone, D.; te Velde, G.; Vernooijs, P.; Versluis, L.; Visscher, L.; Visser, O.; Wang, F.; Wesolowski, T. A.; Van Wezenbeek, E. M.; Wiesenekker, G.; Wolff, S. K.; Woo, T. K.; Yakovlev, A. L.; Ziegler, T.; *ADF2005.01*; SCM: Amsterdam, The Netherlands; Fonseca Guerra, C.; Snijders, J. G.; te Velde, G.; Baerends, E. J. *Theor. Chem. Acc.* **1998**, *99*, 391.

- 11 te Velde, G.; Bickelhaupt, F. M.; Baerends, E. J.; Fonseca Guerra, C.; van Gisbergen, S. J. A.; Snijders, J. G.; Ziegler, T. *J. Comput. Chem.* **2001**, *22*, 931; Baerends, E. J.; Ellis, D. E.; Ros, P. *Chem. Phys.* **1973**, *2*, 41.
- 12 Handy, N. C.; Cohen, A. J. *Mol. Phys.* **2001**, *99*, 403; Lee, C.; Yang, W.; Parr, R. G. *Phys. Rev. B* **1988**, *37*, 785.
- 13 Swart, M.; Ehlers, A. W.; Lammertsma, K. *Mol. Phys.* **2004**, *102*, 2467; Baker, J.; Pulay, P. *J. Chem. Phys.* **2002**, *117*, 1441; Xu, X.; Goddard III, W. A. *J. Phys. Chem. A* **2004**, *108*, 8495; Gonzales, J. M.; Allen, W. D.; Schaefer III, H. F. *J. Phys. Chem. A* **2005**, *109*, 10613; Grüning, M.; Gritsenko, O. V.; Baerends, E. J. *J. Phys. Chem. A* **2004**, *108*, 4459.
- 14 Fan, L.; Ziegler, T. *J. Chem. Phys.* **1990**, *92*, 3645.
- 15 Fan, L.; Versluis, L.; Ziegler, T.; Baerends, E. J.; Ravenek, W. *Int. J. Quantum Chem. Quantum Chem. Symp.* **1988**, *S22*, 173.
- 16 Fukui, K. *Acc. Chem. Res.* **1981**, *14*, 363.
- 17 ΔE_{strain} is +0.4 kcal/mol and not exactly 0.0 kcal/mol because the [CH₃Cl] moiety is kept frozen to its geometry in the RC, which is already slightly deformed with respect to the equilibrium geometry of isolated chloromethane because of the interaction with the chloride anion.
- 18 For the role of steric repulsion in determining equilibrium geometries, see also: Bickelhaupt, F. M.; Baerends, E. J. In *Reviews in Computational Chemistry*; Lipkowitz, K. B., Boyd, D. B., Eds.; Wiley-VCH: New York, 2000; Vol. 15, p 1-86; Bickelhaupt, F. M.; DeKock, R. L.; Baerends, E. J. *J. Am. Chem. Soc.* **2002**, *124*, 1500; Bickelhaupt, F. M.; Baerends, E. J. *Angew. Chem.* **2003**, *115*, 4315.

6 *Frontside versus Backside S_N2 Substitution at Group-14 Atoms: Origin of Reaction Barriers and Reasons for their Absence*

Adapted from

Bento, A. P.; Bickelhaupt, F. M. *Chem. Asian J.* **2008**, 3, online

Abstract

We have theoretically studied the gas-phase nucleophilic substitution at group-14 atoms (S_N2@A) in the model reactions of Cl⁻ + AH₃Cl (A = C, Si, Ge, Sn and Pb) using relativistic density functional theory (DFT) at ZORA-OLYP/TZ2P. In the first place, we wish to explore and understand how the reaction coordinate ζ and potential energy surfaces (PES) along ζ vary as the center of nucleophilic attack changes from carbon to the heavier group-14 atoms. Secondly, this is done not only for the more common backside reaction (S_N2-b) but also for the frontside pathway (S_N2-f). The S_N2-b reaction is found to have a central barrier for A = C but for none of the other group-14 atoms A = Si - Pb. At variance, the S_N2-f mechanism always has a central barrier and the associated pentacoordinate transition species is always higher in energy than that of backside S_N2-b. However, the energy difference between the two becomes smaller if A descends in group 14. Relativistic effects destabilize reactant complexes and transition species by up to 10 kcal/mol (for S_N2-f@Pb) but they do not change heights of barriers relative to each other. We also address the nature of the transformation in the frontside S_N2-f reactions in terms of turnstile rotation versus Berry pseudorotation mechanism. To understand the trends in activation barriers, we have analyzed our model reactions using the extended Activation Strain model, in which the PES $\Delta E(\zeta)$ is decomposed into the strain $\Delta E_{\text{strain}}(\zeta)$ associated with deforming the reactants plus the interaction $\Delta E_{\text{int}}(\zeta)$ between the deformed reactants.

6.1. Introduction

Bimolecular nucleophilic substitution (S_N2) reactions play an important role in organic synthesis¹ and various experimental and theoretical studies have therefore been devoted to obtain a better understanding of the nature of these processes.²⁻⁷ The symmetric, thermoneutral S_N2 reaction between the chloride anion and chloromethane, $Cl^- + CH_3Cl$, in the gas phase is generally employed as the archetypal model for nucleophilic substitution (eq 6.1).



This reaction proceeds preferentially through backside nucleophilic attack of the chloride anion at the carbon atom ($S_N2@C$) with concerted expulsion of the leaving group. A well-known feature of gas-phase $S_N2@C$ reactions is their double-well potential energy surface (PES) along the reaction coordinate, shown in Figure 6.1. This PES is characterized by a central barrier, provided by a trigonal bipyramidal transition state (TS), that separates two pronounced minima, associated with the reactant and product ion–molecule complexes (RC and PC).

Interestingly, if one goes from the $S_N2@C$ reaction of $Cl^- + CH_3Cl$ (eq 6.1) to the corresponding $S_N2@Si$ reaction of the isoelectronic and isostructural reaction system of $Cl^- + SiH_3Cl$ (eq 6.2), the central barrier disappears.^{2,8-10}



This phenomenon, which leads to a transition from a double-well to a single-well PES, is as such well known (see Figure 6.1). Recently (see Chapter 5), we have shown in complementary studies that the disappearance of the central barrier in the $S_N2@Si$ reactions is associated with less steric congestion around the large silicon atom as well as with a more favorable nucleophile–substrate interaction.^{2,6,7} Interestingly, the central barrier reappears as the steric bulk around the silicon atom is raised yielding the first example of an $S_N2@Si$ reaction that proceeds via the classical double-well potential with a central reaction barrier. Importantly, these results also highlight the steric nature of the S_N2 barrier in general.

The available data are less abundant for pentacoordinate group-14 atoms heavier than silicon, that is, germanium ($S_N2@Ge$),^{9,10} tin ($S_N2@Sn$),^{9,11} and lead ($S_N2@Pb$).¹¹ They find that the central, pentacoordinate transition species is a stable intermediate in the case of germanium, tin as well as lead. This suggests a single-well PES also for S_N2 at heavier group-14 atoms (eqs 6.3 - 6.5).

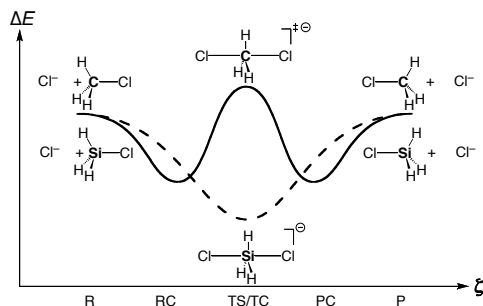


Figure 6.1. Double-well $S_N2@C$ (solid line) and single-well $S_N2@Si$ (dashed line) potential energy surfaces along the reaction coordinate ζ (R = reactants, RC = reactant complex, TS = transition state, TC = stable transition complex, PC = product complex, P = products).



Likewise, frontside nucleophilic substitution (S_N2-f) at carbon has been studied much less than the regular backside pathway (S_N2-b). Yet, a number of studies on this retention-of-configuration mechanism appeared throughout the years.^{4,5,12-14} Experimental support for a retention-of-configuration (or S_N2-f) mechanism was first provided, in 1978 by Cayzergues *et al.*,¹² in a study on the reaction between lithium ethoxide and 3-chlorobut-1-ene in ethanol. Harder *et al.*⁵ later on conducted calculations in which it was shown that for $F^- + CH_3F$ the TS of S_N2-f is 47 kcal/mol higher than the TS of regular S_N2-b while for $LiF + CH_3F$, at variance, the S_N2-f pathway is more favorable than S_N2-b . In a computational study on identity S_N2 reactions of halide anions with methyl halides, Glukhovtsev *et al.*¹³ confirmed that the frontside S_N2-f mechanism is associated with a far higher central barrier than the backside S_N2-b pathway.

Herein, we present the results of a computational study on the backside S_N2-b and frontside S_N2-f reactions at carbon and silicon (eqs 6.1 - 6.2) as well as those at germanium, tin and lead (eqs 6.3 - 6.5) based on relativistic density functional theory (DFT) calculations at ZORA-OLYP/ TZ2P as implemented in the Amsterdam Density Functional (ADF) program.^{15,16} This level of theory was previously shown to agree within a few kcal/mol with highly correlated *ab initio* benchmarks.¹⁷

Our purpose is threefold. In the first place, we wish to explore and understand how the reaction coordinate ζ and potential energy surfaces (PES) along ζ vary as the center of nucleophilic attack changes from carbon to the heavier group-14 atoms. Secondly, this is done not only for the more common backside reaction (S_N2-b) but also for the frontside

pathway (S_N2-f). A third issue is the question in how far the trends are influenced by relativistic effects, especially for the heaviest group-14 congeners.

6.2. Methods

6.2.1. Computational Details

All calculations were performed with the Amsterdam Density Functional (ADF) program developed by Baerends and others.^{15,16} The molecular orbitals (MOs) were expanded in a large uncontracted set of Slater-type orbitals (STOs) containing diffuse functions, TZ2P. This basis is of triple- ζ quality and has been augmented by two sets of polarization functions: $2p$ and $3d$ on hydrogen, $3d$ and $4f$ on carbon, silicon and chlorine, $4d$ and $4f$ on germanium, $5d$ and $4f$ on tin and $5f$ and $6d$ on lead. The core shells of carbon ($1s$), silicon ($1s2s2p$), germanium ($1s2s2p3s3p$), tin ($1s2s2p3s3p3d4s4p$), lead ($1s2s2p3s3p3d4s4p4d$) and chlorine ($1s2s2p$) were treated by the frozen-core approximation.¹⁵ An auxiliary set of s , p , d , f and g STOs was used to fit the molecular density and to represent the Coulomb and exchange potentials accurately in each SCF cycle.

Energies and fully optimized geometries were computed with the OLYP¹⁸ density functional, which involves Handy's optimized exchange (OPTX). Relativistic effects were treated using the zeroth-order regular approximation (ZORA) method.¹⁹ This approach was previously shown to agree satisfactorily with highly correlated *ab initio* benchmarks.^{17,20} All stationary points were confirmed by vibrational analysis:²¹ for equilibrium structures all normal modes have real frequencies, whereas transition states²² have one normal mode with one imaginary frequency. Furthermore, transition states were verified to connect the supposed reactant and product minima by carrying out intrinsic reaction coordinate (IRC) calculations.²³

Enthalpies at 298.15K and 1atm (ΔH_{298}) were calculated from 0K electronic energies (ΔE) according to eq 6.6, assuming an ideal gas.²⁴

$$\Delta H_{298} = \Delta E + \Delta E_{\text{trans},298} + \Delta E_{\text{rot},298} + \Delta E_{\text{vib},0} + \Delta(\Delta E_{\text{vib},0})_{298} + \Delta(pV) \quad (6.6)$$

$\Delta E_{\text{trans},298}$, $\Delta E_{\text{rot},298}$, $\Delta E_{\text{vib},0}$ are the differences between products and reactants in translational, rotational and zero point vibrational energy, respectively; $\Delta(\Delta E_{\text{vib},0})_{298}$ is the change in the vibrational energy difference as one goes from 0 to 298.15K. The vibrational energy corrections are based on the frequency calculations. The molar term $\Delta(pV)$ is $(\Delta n)RT$, where $\Delta n = -1$ for two reactants combining into one species. Thermal corrections for the electronic energy are neglected.

6.2.2. Analysis of the Potential Energy Surfaces

Insight into how the activation barriers arise was obtained using the Activation Strain model of chemical reactivity (see Chapter 2). In this model, the potential energy surface $\Delta E(\zeta)$ is decomposed, along the reaction coordinate ζ , into the strain $\Delta E_{\text{strain}}(\zeta)$ associated with deforming the individual reactants, plus the actual interaction $\Delta E_{\text{int}}(\zeta)$ between the deformed reactants:

$$\Delta E(\zeta) = \Delta E_{\text{strain}}(\zeta) + \Delta E_{\text{int}}(\zeta) \quad (6.7)$$

The strain $\Delta E_{\text{strain}}(\zeta)$ is determined by the rigidity of the reactants and on the extent to which groups must reorganize in a particular reaction mechanism, whereas the interaction $\Delta E_{\text{int}}(\zeta)$ between the reactants depends on their electronic structure and on how they are mutually oriented as they approach each other. In the present study, the reactants are the nucleophile Cl^- and either one of the substrates AH_3Cl .

6.3. Results and Discussion

6.3.1. Backside $\text{S}_{\text{N}}2\text{-b}$: Reaction Profiles

Our ZORA-OLYP/TZ2P results for relative energies and structures of stationary points are collected in Tables 6.1 - 6.3. Generic structures of stationary points are illustrated in Scheme 6.1. For backside nucleophilic substitution ($\text{S}_{\text{N}}2\text{-b}$), we recover the well-known change from a double-well PES with a central barrier and transition state **1TS-b** for the $\text{S}_{\text{N}}2\text{-b@C}$ of $\text{Cl}^- + \text{CH}_3\text{Cl}$ (eq 6.1) to a single-well PES for the $\text{S}_{\text{N}}2\text{-b@Si}$ of $\text{Cl}^- + \text{SiH}_3\text{Cl}$ (eq 6.2) in which the pentavalent transition species **2TC-b** has turned from a labile TS into a stable transition complex. This is illustrated in Figure 6.1. The reactant complex **1RC-b** of the $\text{S}_{\text{N}}2\text{-b@C}$ reaction is bound by 9.0 kcal/mol, and it is separated from the product complex **1PC-b** by a central barrier of 8.8 kcal/mol. The $\text{S}_{\text{N}}2\text{-b@Si}$ reaction features only a stable pentacoordinate TC (no TS, RC or PC) at -24.4 kcal/mol.

Here, we find that this trend further continues along the $\text{S}_{\text{N}}2\text{-b}$ substitutions at the heavier central atoms germanium, tin and lead (eqs 6.3 - 6.5) which all have single-well reaction profiles with a TC at -24.3, -32.3 and -32.3 kcal/mol, respectively (see Table 6.1). The A-Cl bond distances of the D_{3h} symmetric transition species is essentially equal for **1TS-b** and **2TC-b**, namely 2.36 Å, and then monotonically increases from 2.36 to 2.49 to 2.63 to 2.75 Å along **3TC-b**, **4TC-b** and **5TC-b** (see Table 6.2). The disappearance of the central barrier from $\text{S}_{\text{N}}2\text{-b@C}$ to $\text{S}_{\text{N}}2\text{-b@Si}$ (and also $\text{S}_{\text{N}}2\text{-b@P}$) has

Table 6.1. Energies (in kcal/mol) relative to reactants of stationary points occurring in backside and frontside S_N2 reactions.^[a]

| reaction | A | backside S_N2 -b | | frontside S_N2 -f | | | |
|----------|----|--------------------|---------------|---------------------|---------------|-------|---------|
| | | RC-b | TS-b or TC-b | TS-H | RC-f | TS-f | |
| 6.1 | C | -9.0 (-9.0) | -0.2 (-0.1) | [c] | [c] | 40.2 | (40.4) |
| 6.2 | Si | [b] | -24.4 (-24.4) | -6.1 (-6.2) | -9.3 (-9.4) | -6.2 | (-6.3) |
| 6.3 | Ge | [b] | -24.3 (-24.8) | [c] | [c] | -2.1 | (-3.3) |
| 6.4 | Sn | [b] | -32.3 (-33.7) | -14.5 (-17.5) | -16.8 (-20.0) | -15.3 | (-18.6) |
| 6.5 | Pb | [b] | -32.3 (-36.3) | -14.3 (-21.1) | -14.5 (-23.5) | -12.9 | (-22.4) |

[a] Computed at ZORA-OLYP/TZ2P (nonrelativistic OLYP/TZ2P values in parentheses). [b] Nonexistent: reaction proceeds barrierless to central transition complex TC-b. [c] Nonexistent: reaction proceeds directly from minima RC-b or TC-b to frontside transition state TS-f.

Table 6.2. Geometries (in Å and deg.) of stationary points occurring in backside and frontside S_N2 reactions.^[a]

| species | A | A-Cl | A-Cl ⁺ | A-H _a | A-H _b | Cl _a -A-H _a | H _a -A-H _b | Cl-A-Cl |
|---------------------|----|-------|-------------------|------------------|------------------|-----------------------------------|----------------------------------|---------|
| AH ₃ Cl | C | 1.792 | [b] | 1.090 | 1.090 | 108.4 | 110.5 | [b] |
| | Si | 2.066 | [b] | 1.489 | 1.489 | 108.9 | 110.0 | [b] |
| | Ge | 2.179 | [b] | 1.531 | 1.531 | 106.6 | 112.2 | [b] |
| | Sn | 2.364 | [b] | 1.713 | 1.713 | 105.9 | 112.8 | [b] |
| | Pb | 2.465 | [b] | 1.767 | 1.767 | 103.9 | 114.4 | [b] |
| backside S_N2 -b | | | | | | | | |
| 1RC-b | C | 1.836 | 3.374 | 1.086 | 1.086 | 108.2 | 110.7 | 180.0 |
| 1TS-b | C | 2.359 | 2.359 | 1.074 | 1.074 | 90.0 | 120.0 | 180.0 |
| 2TC-b | Si | 2.356 | 2.356 | 1.485 | 1.485 | 90.0 | 120.0 | 180.0 |
| 3TC-b | Ge | 2.493 | 2.493 | 1.525 | 1.525 | 90.0 | 120.0 | 180.0 |
| 4TC-b | Sn | 2.631 | 2.631 | 1.713 | 1.713 | 90.0 | 120.0 | 180.0 |
| 5TC-b | Pb | 2.754 | 2.754 | 1.762 | 1.762 | 90.0 | 120.0 | 180.0 |
| frontside S_N2 -f | | | | | | | | |
| 1TS-H | C | [c] | [c] | [c] | [c] | [c] | [c] | [c] |
| 2TS-H | Si | 2.155 | 2.556 | 1.541 | 1.493 | 102.2 | 96.6 | 110.0 |
| 3TS-H | Ge | [c] | [c] | [c] | [c] | [c] | [c] | [c] |
| 4TS-H | Sn | 2.440 | 2.786 | 1.805 | 1.726 | 98.8 | 96.5 | 104.8 |
| 5TS-H | Pb | 2.538 | 2.924 | 1.878 | 1.776 | 93.6 | 98.8 | 96.2 |
| 1RC-f | C | [c] | [c] | [c] | [c] | [c] | [c] | [c] |
| 2RC-f | Si | 2.151 | 2.500 | 1.542 | 1.495 | 91.3 | 96.9 | 89.5 |
| 3RC-f | Ge | [c] | [c] | [c] | [c] | [c] | [c] | [c] |
| 4RC-f | Sn | 2.468 | 2.672 | 1.791 | 1.738 | 87.7 | 97.9 | 87.0 |
| 5RC-f | Pb | 2.560 | 2.825 | 1.868 | 1.793 | 88.3 | 99.2 | 88.5 |
| 1TS-f | C | 2.658 | 2.658 | 1.080 | 1.078 | 90.6 | 117.6 | 90.1 |
| 2TS-f | Si | 2.293 | 2.293 | 1.497 | 1.523 | 100.8 | 105.6 | 86.9 |
| 3TS-f | Ge | 2.434 | 2.434 | 1.543 | 1.574 | 99.9 | 108.0 | 85.0 |
| 4TS-f | Sn | 2.564 | 2.564 | 1.735 | 1.768 | 100.7 | 107.7 | 84.7 |
| 5TS-f | Pb | 2.675 | 2.675 | 1.798 | 1.836 | 99.8 | 109.5 | 84.6 |

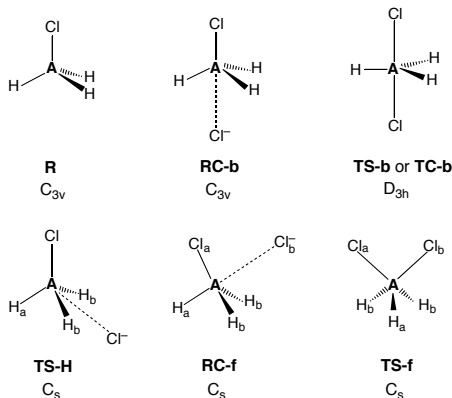
[a] Computed at ZORA-OLYP/TZ2P. See Scheme 6.1 for definition of geometry parameters. [b] Not contained in AH₃Cl. [c] Nonexistent: reaction proceeds directly from minima RC-b or TC-b to frontside transition state TS-f.

Table 6.3. Energies, enthalpies, entropies and Gibbs free energies (in kcal/mol and cal mol⁻¹ K⁻¹) of the transition species in backside and frontside S_N2 reactions relative to reactants.^[a]

| reaction | A | ΔE | ΔH | ΔS | ΔG |
|------------------------------|----|------------|------------|------------|------------|
| backside S _N 2-b | | | | | |
| 1 | C | -0.2 | -1.2 | -25.1 | 6.3 |
| 2 | Si | -24.4 | -24.0 | -26.1 | -16.2 |
| 3 | Ge | -24.3 | -24.0 | -24.8 | -16.6 |
| 4 | Sn | -32.3 | -31.9 | -25.2 | -24.4 |
| 5 | Pb | -32.3 | -32.5 | -24.9 | -25.1 |
| frontside S _N 2-f | | | | | |
| 1 | C | 40.2 | 38.4 | -16.9 | 43.4 |
| 2 | Si | -6.2 | -6.7 | -24.8 | 0.6 |
| 3 | Ge | -2.1 | -2.9 | -24.0 | 4.2 |
| 4 | Sn | -15.3 | -16.1 | -24.5 | -8.8 |
| 5 | Pb | -12.9 | -14.4 | -24.8 | -7.1 |

[a] Computed at ZORA-OLYP/TZ2P.

previously been traced to a decrease in steric congestion in the case of the larger central atom as well as a more favorable nucleophile–substrate interaction.^{2,6} We come back to this later on in this chapter.

Scheme 6.1. Structures of stationary points for backside S_N2-b and frontside S_N2-f.

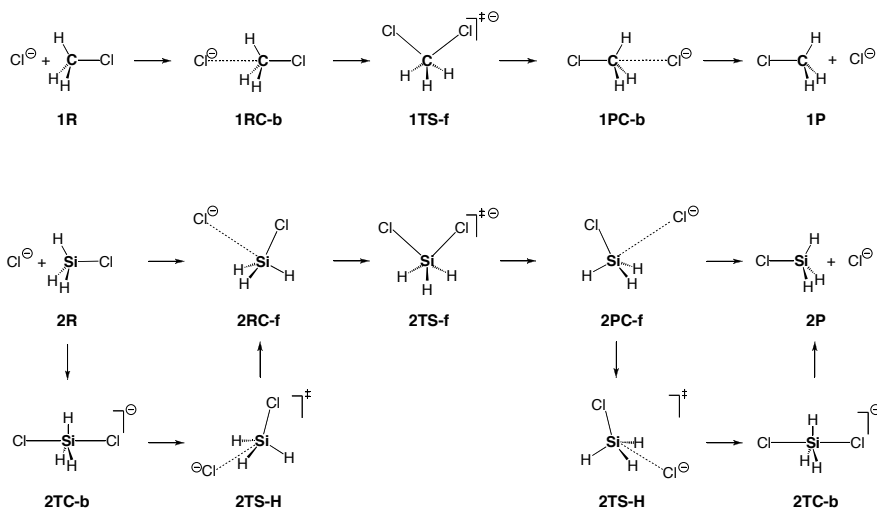
6.3.2. Frontside S_N2-f: Reaction Profiles

Frontside nucleophilic substitution (S_N2-f) proceeds, at variance with backside S_N2-b, in *all* cases via a central barrier and a C_s symmetric pentavalent TS that is significantly higher in energy than the corresponding transition species for backside substitution (S_N2-b). Thus, the TS for the S_N2-f substitutions is at 40.2 (C), -6.2 (Si), -2.1 (Ge), -15.3 (Sn) and -12.9 kcal/mol (Pb) relative to the reactants which has to be compared with the corresponding transition species of the backside S_N2-b pathway which are at -0.2 (C), -24.4 (Si), -24.3 (Ge), -32.3 (Sn) and -32.3 kcal/mol (Pb) (see Table 6.1). The frontside

S_N2 -f pathway can in all cases be characterized by a double-well PES but the nature of the minima may differ between the various model reaction systems, as explained in the following.

The frontside S_N2 -f@C reaction of $\text{Cl}^- + \text{CH}_3\text{Cl}$ proceeds via the same reactant and product complexes **1RC-b** and **1PC-b** as the backside S_N2 -b@C pathway (see Scheme 6.2). Separate frontside reactant and product complexes do not exist for this model system. The minima **1RC-b** and **1PC-b** on the double-well PES are now interconverted via the C_s symmetric transition state, **1TS-f** (Scheme 6.2), at 40.2 kcal/mol (see Table 6.1). This corresponds to a central barrier of 49.2 kcal/mol. In **1TS-f**, the nucleophile and leaving group are direct neighbors that bind to carbon via two equivalent C–Cl bonds of 2.66 Å (see Scheme 6.2 and Table 6.2).

Scheme 6.2. Stationary points along frontside S_N2 -f at carbon and silicon.



The frontside S_N2 -f@Si reaction of $\text{Cl}^- + \text{SiH}_3\text{Cl}$ may proceed via characteristic frontside reactant and product complexes **2RC-f** and **2PC-f** that are bound by 9.3 kcal/mol relative to separate reactants or products (see Scheme 6.2 and Table 6.1). These minima on the double-well PES are interconverted via the C_s symmetric transition state, **2TS-f** (Scheme 6.2), at –6.2 kcal/mol (see Table 6.1) which corresponds to a central barrier of 3.1 kcal/mol. In **2TS-f**, the nucleophile and leaving group are direct neighbors that bind to silicon via two equivalent Si–Cl bonds of 2.29 Å (see Scheme 6.2 and Table 6.2). Alternatively, the reaction may also proceed via prior association of the reactants in the stable transition complex **2TC-b** of the backside pathway at –24.4 kcal/mol. From here, instead of following the S_N2 -b pathway, the frontside reactant complex **2RC-f** is obtained through rearrangement via transition state **2TS-H**, at –6.1 kcal/mol, in which the Cl^-

nucleophile is migrating on the bisector, in between two Si–H bonds, towards the frontside (see Scheme 6.2 and Table 6.1). The corresponding process can occur in the product complex. And, of course, also the leaving group may undergo an equivalent migration, which represents a shortcut from **2TC-b** to **2PC-f** not shown in Scheme 6.2.

The frontside S_N2 -f substitutions at the heavier group-14 atoms Ge, Sn and Pb show similar reaction profiles and stationary points as that for S_N2 @Si, with one exception. In the case of the S_N2 -f@Ge reaction of $Cl^- + GeH_3Cl$, the intrinsic reaction coordinate (IRC) leads from the frontside **3TS-f** directly to the backside transition complex **3TC-b**. No stable frontside reactant or product complexes and no transition state of the type TS-H exist on the PES of this reaction pathway.

The trends found on the PESes, i.e., in terms of relative energies, are hardly affected by zero-point vibrational and thermal effects as well as entropy effects computed at 298 K (see Table 6.3). Thus, enthalpies ΔH_{298} of transition species (TS or TC) relative to reactants differ by about 2 kcal/mol or less from the corresponding energies. The decreased density of states in the more tightly bound transition species leads consistently to a reduction in entropy ΔS_{298} of some -24 to -26 cal mol $^{-1}$ K $^{-1}$ which translates into a destabilization of the Gibbs free energies ΔG_{298} (as compared to the enthalpies ΔH_{298}) of 6 to 8 kcal/mol (see Table 6.3). A somewhat smaller, negative activation entropy ΔS_{298} is obtained for frontside S_N2 -f substitution at carbon, only -16.9 cal mol $^{-1}$ K $^{-1}$ which corresponds to a slight destabilization of 3 kcal/mol $^{-1}$ of the activation Gibbs free energy ΔG_{298} (as compared to the activation enthalpy ΔH_{298}). We come back to this in the section on activation strain analyses of frontside S_N2 -f.

6.3.3. Frontside S_N2 -f: Berry Pseudorotation and/or Turnstile Rotation?

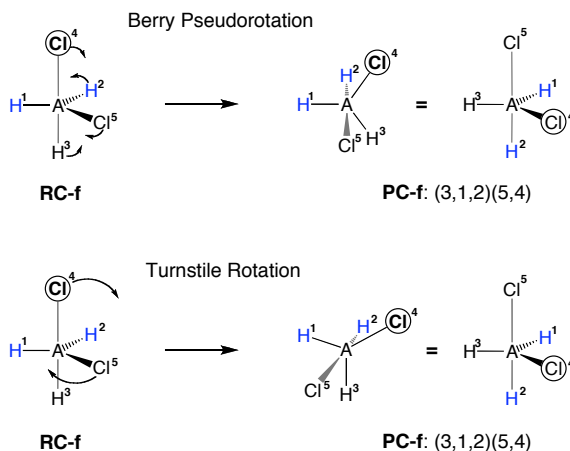
The backside S_N2 -b process leads to inversion of configuration of the AH_3 moiety whereas the frontside S_N2 -f pathway goes with retention of configuration. However, whereas the overall transformation of the backside pathway is easily envisaged as an "inverting umbrella" the situation is, at first sight, somewhat less clear in the case of the frontside substitution. The question is, in particular, *how* and *to which position* the three H atoms move while the nucleophile Cl and leaving group Cl exchange their axial and equatorial position from **RC-f** to **PC-f**.

Ligand rearrangements in pentavalent silicon compounds have been described, among others, in terms of the Berry Pseudorotation²⁵ and the Turnstile Rotation²⁶ mechanisms. These two mechanisms are illustrated in Scheme 6.3 for our frontside S_N2 -f process. It will become clear in a moment that Berry Pseudorotation and Turnstile Rotation are two ways of looking at one and the same geometrical transformation. In the Berry Pseudorotation mechanism, the axial Cl^4 (nucleophile) and H^3 bent to the right, away from the equatorial H^1 , and become themselves equatorial while the equatorial Cl^5

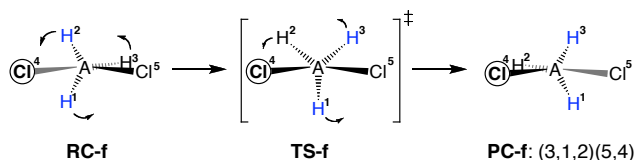
(leaving group) and H^2 bent to the left, *towards* the equatorial H^1 which is standing still (Scheme 6.3, upper). The result is a permutation of positions in the trigonal bipyramid indicated as $(1,2,3)(4,5) \rightarrow (3,1,2)(5,4)$, i.e., H^3 to H^1 , H^1 to H^2 , H^2 to H^3 and Cl^5 to Cl^4 , Cl^4 to Cl^5 , indicated as $(3,1,2)(5,4)$.

In the Turnstile Rotation mechanism, the axial Cl^4 (nucleophile) and the equatorial Cl^5 (leaving group) are conceived as a pair that rotates with respect to the AH_3 moiety such that Cl^4 adopts an *equatorial* position in between H^1 and H^3 (which in the course also changes from axial to equatorial!) and Cl^5 adopts an *axial* position opposite to H^2 (which thus also changes from equatorial to axial!). Note that the result is again a $(3,1,2)(5,4)$ permutation of positions, identical to the result of the Berry Pseudorotation.

Scheme 6.3. Berry Pseudorotation and Turnstile Rotation Mechanisms (gray: axial bonds)



Next, we have examined in detail, for all five reaction systems, the nature of the motions in the frontside S_N2 -f transition state and along the IRC that leads away from this TS. The motions appear in all five transition states (i.e., for $A = C, Si, Ge, Sn$ and Pb) as a rotation between the pair of Cl^4 and Cl^5 relative to the trio of H^1 , H^2 and H^3 as shown in Scheme 6.4. In the case of $A = Si, Sn$ and Pb , this corresponds to the $(3,1,2)(5,4)$ permutation of positions, discussed above, as we go from **RC-f** to **PC-f**. In the perspective shown in Scheme 6.4, this appears as a relative rotation over 50° . The reduced mass associated with this normal mode is approximately equal to that of the three hydrogens (as they are much lighter than the two chlorines) and a visualization of the normal mode and the IRC therefore shows an AH_3 group rotating with respect to two Cl atoms standing practically still.

Scheme 6.4. IRC of all frontside S_N2 -f substitutions (gray: axial bonds)

The fact that the transition vector and the IRC associated with the frontside S_N2 -f substitutions appears as a rotation makes it natural to designate this process as a Turnstile Rotation. However, we stress that this is not really different from the Berry Pseudorotation, it is just a different way of expressing the overall transformation in terms of partial motions. In fact, if one considers the Berry Pseudorotation in Scheme 6.3 more carefully, one can recognize that the simultaneous bending of the two A–Cl bonds together generates a rotational motion of Cl^4 and Cl^5 relative to the AH_3 fragment.

6.3.4. Backside S_N2 -b: Activation Strain Analyses

Next, we examine *why* S_N2 central barriers decrease as the central atom descends in group 14 and why they are higher for frontside S_N2 -f than backside S_N2 -b. To this end, we have carried out Activation Strain analyses (see eq 6.7; see also Chapter 2) of the reaction potential energy surfaces (PES) along the IRC projected onto the nucleophile–central atom distance (Nu–A). Because there is no central barrier and no TS in the backside S_N2 -b reactions of the heavier group-14 central atoms, the IRC is modeled for this pathway by a linear transit in which the Nu–A distance and the central atom–leaving group (A–L) distance run synchronously in 20 steps from their value in the D_{3h} symmetric transition species to that in the RC-b (for A = C) or to a geometry that closely resembles the separate reactants defined as Nu–A = 6 Å and A–L = equilibrium value in isolated substrate (for A = Si, Ge, Sn, Pb). For the S_N2 -b reaction of $Cl^- + CH_3Cl$, we have verified that this yields essentially the same reaction profiles as the one based on a regular IRC. The results of the Activation Strain analyses are collected in Figure 6.2 in which the reaction coordinate is the nucleophile–central atom distance Cl^- –A *relative to the transition species* at which it is set to 0. Note that in the graphs of Figure 6.2 the reaction proceeds from the right to the left.

Figure 6.2a shows the reaction profiles of our backside and frontside substitutions (for numerical data, see Table 6.1). The disappearance of the central barrier in the backside S_N2 -b reaction from A = C to Si is due to both, a reduced strain ΔE_{strain} and a more stabilizing nucleophile–substrate interaction ΔE_{int} (see Figure 6.2b, left). The origin of this decrease in strain for $Cl^- + SiH_3Cl$ has been recently traced to the reduced steric congestion and steric (Pauli) repulsion between the five substituents in the D_{3h} symmetric

pentavalent transition species as the central atom becomes larger from C to Si.^{2,6} The stronger interaction in the latter case is due to the better nucleophile–substrate $\langle 3p \mid \sigma_{A-Cl}^* \rangle$ overlap if the relatively diffuse Cl^- $3p$ AO approaches the also more extended silicon $3p$ lobe of SiH_3Cl σ_{Si-Cl}^* (0.29 in **2TC-b**) than if it approaches the compact $2p$ lobe in the CH_3Cl σ_{C-Cl}^* LUMO (0.21 in **1TS-b**, not shown in the tables). The contour plots in Figure 6.3 provide a graphical representation of the shape of the substrate σ_{A-Cl}^* LUMO and how this obtains a more extended backside lobe if we go from A = C to Si (see also Ref. 27).

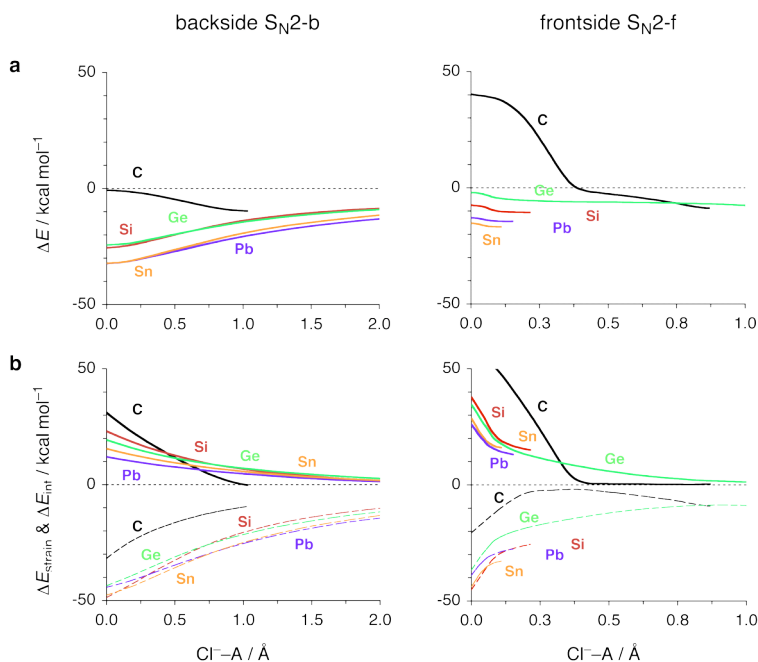


Figure 6.2. Analysis of backside and frontside S_N2 reactions of $Cl^- + AH_3Cl$ with A = C, Si, Ge, Sn, Pb along the intrinsic reaction coordinate projected onto the Cl^-A (i.e., Nu–A) distance relative to the transition species at which $Cl^-A = 0$: (a) potential energy surface ΔE ; (b) decomposition $\Delta E = \Delta E_{strain} + \Delta E_{int}$ indicated with plain and dashed curves, respectively.

Our analyses show that the trend of decreasing strain from $Cl^- + CH_3Cl$ to $Cl^- + SiH_3Cl$ continues also along the backside S_N2 -b substitutions at the heavier group-14 atoms. Thus, the ΔE_{strain} curves in Figure 6.2b, left, become less and less destabilizing as the size of the central atom increases along A = C, Si, Ge, Sn and Pb and the steric congestion decreases. The nucleophile–substrate interaction is furthermore consistently more stabilizing for S_N2 -b substitution at the heavier group-14 atoms than at carbon because of the better HOMO–LUMO overlap and thus orbital interactions and a stronger electrostatic attraction with the more electropositive central atom,²⁷ in particular, in the case of A = Pb (not shown in the tables).

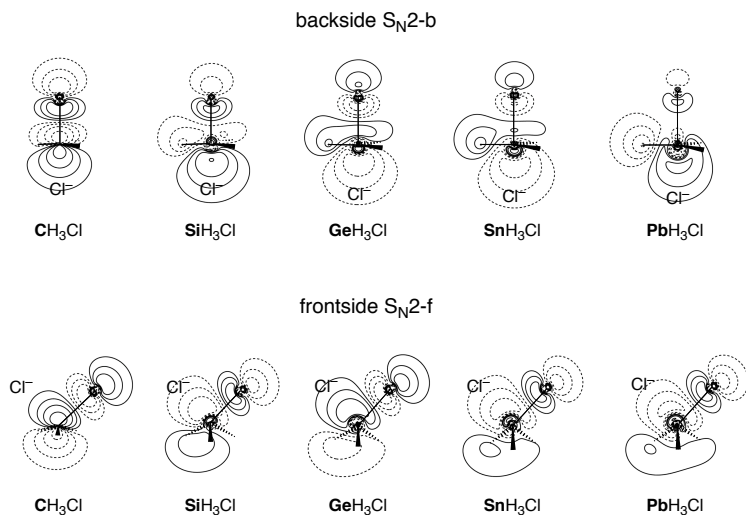


Figure 6.3. Contour plots of the $\sigma^*_{\text{A-Cl}}$ acceptor orbital of AH_3Cl fragments (see wire frames) in backside $S_N2\text{-b}$ and frontside $S_N2\text{-f}$ transition species, computed at ZORA-OLYP/TZ2P (contour values: 0.0, ± 0.02 , ± 0.05 , ± 0.1 , ± 0.2 , ± 0.5 a.u.; solid and dashed contours refer to positive and negative values). For each AH_3Cl $\sigma^*_{\text{A-Cl}}$ orbital, the position of the nucleophile Cl^- in the corresponding transition species is indicated.

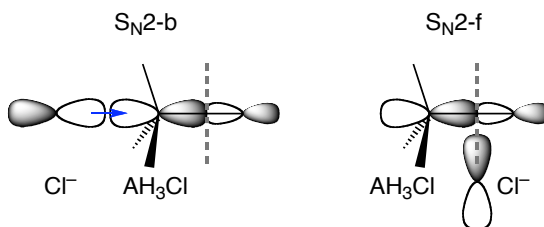
6.3.5. Frontside $S_N2\text{-f}$: Activation Strain Analyses

The destabilization of the frontside $S_N2\text{-f}$ transition states compared to the corresponding backside $S_N2\text{-b}$ transition species (TS or TC) is mainly the result of increased activation strain as can be seen from a comparison of the strain curves ΔE_{strain} in the left and right panels of Figure 6.2b. This is so especially for $S_N2\text{-f@C}$ for which the ΔE_{strain} curve runs off the scale: for comparison, $\Delta E_{\text{strain}}^\ddagger$ amounts to 31.8 and 60.8 kcal/mol in **1TS-b** and **1TS-f**, respectively (not shown in tables). But also the nucleophile–substrate interaction ΔE_{int} is weakened from backside to frontside substitution (compare again left and right panels of Figure 6.2b). This effect is however significantly smaller than the destabilization of the activation strain. For example, $\Delta E_{\text{int}}^\ddagger$ amounts to -32.0 and -20.6 kcal/mol in **1TS-b** and **1TS-f**, respectively (not shown in tables).

The weakening in the nucleophile–substrate interaction ΔE_{int} originates from the poor bond overlap in the frontside orientation between the Cl^- 3p AOs and the AH_3Cl $\sigma^*_{\text{A-Cl}}$ acceptor orbital. Thus, the $\langle 3p | \sigma^*_{\text{A-Cl}} \rangle$ overlap in the frontside TS-f varies from 0.10 to 0.26 to 0.23 to 0.24 to 0.19 along $\text{A} = \text{C}, \text{Si}, \text{Ge}, \text{Sn}$ and Pb (not shown in tables).²⁸ This has to be compared with the larger overlap values in the corresponding backside transition species which vary from 0.21 to 0.29 to 0.27 to 0.28 to 0.22 (not shown in tables). The reason for this effect is the cancellation of overlap as the Cl^- 3p AO approaches the $\sigma^*_{\text{A-Cl}}$ acceptor orbital in the frontside orientation at its nodal surface (see Scheme 6.5). Such cancellation of overlap does not occur when the Cl^- 3p AO

approaches the backside lobe of the $\sigma^*_{\text{A-Cl}}$ acceptor orbital (see Scheme 6.5). The cancellation of overlap is the largest for $\text{A} = \text{C}$ and becomes less pronounced for the heavier group-14 central atoms. The reason is the increasing amplitude of the central atom's np AO in $\sigma^*_{\text{A-Cl}}$ as this atom becomes more electropositive (see Figure 6.3). This overlap argument has been proposed on qualitative grounds by Anh and Minot²⁹ and is here quantitatively confirmed for $\text{S}_{\text{N}}2$ reactions in general.

Scheme 6.5. Overlap between Cl^- 3p HOMO and AH_3Cl $\sigma^*_{\text{A-Cl}}$ LUMO in $\text{S}_{\text{N}}2\text{-b}$ and $\text{S}_{\text{N}}2\text{-f}$.



Yet, interestingly, not reduced bond overlap but increased strain is the dominant factor causing the higher frontside $\text{S}_{\text{N}}2\text{-f}$ barriers, as pointed out above (see also Figure 6.2b). This can be traced to the fact that in the frontside substitution two large substituents, i.e., nucleophile and leaving group, must be accommodated in the pentavalent transition state. This unfavorable situation causes a slightly larger deformation in the case of the heavier group-14 atoms (see Table 6.2). But in the case of the sterically congested carbon, it causes a more significant and energetically quite unfavorable deformation (see Table 6.2). This is aggravated by the fact that the CH_3 moiety is relatively rigid and gives in much less to the steric pressure of the (unfavorably placed) fifth substituent than the C-Cl (leaving group) bond. The result is a strongly expanded C-Cl distance of 2.658 Å which has to be compared with the much shorter C-Cl bond of 2.359 Å in **1TS-b** or the Si-Cl bond of 2.293 Å in **2TS-f** (see Table 6.2). This more weakly bound character of the **1TS-f** is associated with a higher density of states which is reflected by the less negative activation entropy ΔS_{298} for this reaction mechanism mentioned above (see also Table 6.3).

6.3.6. Relativistic Effects

We have assessed the importance of taking relativistic effects into account by comparing our relativistic ZORA-OLYP/TZ2P reaction profiles with nonrelativistic OLYP/TZ2P results. The latter are also shown in Table 6.1, in parentheses. The main trends for the $\text{Cl}^- + \text{AH}_3\text{Cl}$ substitution reactions are preserved if relativity is neglected, i.e., decreasing barriers as the central atom descends in group 14 and higher frontside than backside barriers.

Absolute values of barriers can however be significantly affected by relativity which destabilizes the stationary points relative to reactants. For the carbon, silicon and germanium containing systems, the relativistic effects are negligible to small, up to ca. 1 kcal/mol for $A = \text{Ge}$. However, in the case of $A = \text{Sn}$ and Pb , the frontside $\text{S}_{\text{N}}2\text{-f}$ transition state is destabilized by about 3 and 10 kcal/mol, respectively. Note that relativistic destabilization is more pronounced for the frontside than for the backside transition states making the former even less viable than they already are.

The origin of the relativistic destabilization has been traced to the relativistic contraction and energy lowering of the central atom $n\text{p}$ AOs. This causes their amplitude in the antibonding $\sigma^*_{\text{A-Cl}}$ acceptor orbital to become smaller which in turn leads to a smaller overlap and less stabilizing donor–acceptor orbital interaction with the nucleophile Cl^- 3p HOMO. In the case of $\text{Cl}^- + \text{PbH}_3\text{Cl}$, for example, switching on relativity causes the $\langle 3\text{p}_z | \sigma^*_{\text{Pb-Cl}} \rangle$ overlap in **5TS-b** to decrease from 0.272 to 0.216 which goes with a *weakening* of the nucleophile–substrate interaction ΔE_{int} from -50.6 to -44.3 kcal/mol (not shown in the tables).

6.4. Conclusions

In conclusion, our Activation Strain analyses show that the central barrier for backside nucleophilic substitution ($\text{S}_{\text{N}}2\text{-b}$) of $\text{Cl}^- + \text{AH}_3\text{Cl}$ disappears as the central atom A goes from carbon to silicon and the heavier group-14 atoms (up till lead). This is because the steric congestion (and repulsion) decreases for the larger central atoms and the orbital interactions become more stabilizing due to a better overlap between the chloride 3p_z HOMO and the substrate $\sigma^*_{\text{A-Cl}}$ LUMO which obtains an increasingly extended amplitude on an even more electropositive atom A .

Furthermore, frontside nucleophilic substitution ($\text{S}_{\text{N}}2\text{-f}$) proceeds in *all* cases via a central barrier associated with a C_s symmetric pentavalent TS that is significantly higher in energy than the corresponding transition species for backside substitution ($\text{S}_{\text{N}}2\text{-b}$). One reason is the less efficient $\langle \text{chloride HOMO} | \text{substrate LUMO} \rangle$ overlap for $\text{S}_{\text{N}}2\text{-f}$ mentioned before by others.²⁹

Interestingly, however, the main reason for the higher barrier for frontside substitution is the increased steric repulsion between nucleophile and leaving group which are adjacent in the TS for frontside $\text{S}_{\text{N}}2\text{-f}$ while they are on opposite sides of the trigonal bipyramidal transition structure for backside $\text{S}_{\text{N}}2\text{-b}$.

References

- 1 Smith, M. B.; March, J. *March's Advanced Organic Chemistry: Reactions, Mechanisms, and Structure*; Wiley: New York, 2007; Carey, F. A.; Sundberg, R. J. *Advanced Organic Chemistry, Part A*; 5th ed.; Springer: New York, 2007; Ingold, C. *Structure and Mechanism in Organic Chemistry*; 2nd ed.; Cornell University Press: Ithaca, NY, 1969; Lowry, T. H.; Richardson, K. S. *Mechanism and Theory in Organic Chemistry*; Harper and Row: New York, 1987.
- 2 Bento, A. P.; Bickelhaupt, F. M. *J. Org. Chem.* **2007**, 72, 2201; van Bochove, M. A.; Swart, M.; Bickelhaupt, F. M. *J. Am. Chem. Soc.* **2006**, 128, 10738.
- 3 Vayner, G.; Houk, K. N.; Jorgensen, W. L.; Brauman, J. I. *J. Am. Chem. Soc.* **2004**, 126, 9054; Gronert, S. *Acc. Chem. Res.* **2003**, 36, 848; Laerdahl, J. K.; Uggerud, E. *Int. J. Mass Spectrom.* **2002**, 214, 277; Chabinyk, M. L.; Craig, S. L.; Regan, C. K.; Brauman, J. I. *Science* **1998**, 279, 1882; Shaik, S. S.; Schlegel, H. B.; Wolfe, S. *Theoretical Aspects of Physical Organic Chemistry: The S_N2 Mechanism*; Wiley: New York, 1992; Olmstead, W. N.; Brauman, J. I. *J. Am. Chem. Soc.* **1977**, 99, 4219; Botschwina, P. *Theor. Chem. Acc.* **1998**, 99, 426; Chandrasekhar, J.; Smith, S. F.; Jorgensen, W. L. *J. Am. Chem. Soc.* **1985**, 107, 154; Lee, I.; Kim, C. K.; Sohn, C. K.; Li, H. G.; Lee, H. W. *J. Phys. Chem. A* **2002**, 106, 1081; Nibbering, N. M. M. *Acc. Chem. Res.* **1990**, 23, 279; DePuy, C. H.; Gronert, S.; Mulin, A.; Bierbaum, V. M. *J. Am. Chem. Soc.* **1990**, 112, 8650; van Bochove, M. A.; Swart, M.; Bickelhaupt, F. M. *ChemPhysChem* **2007**, 8, 2452; Bach, R. D.; Dmitrenko, O.; Thorpe, C. *J. Org. Chem.* **2008**, 73, 12; van Bochove, M. A.; Bickelhaupt, F. M. *Eur. J. Org. Chem.* **2008**, 649; Glukhovtsev, M. N.; Pross, A.; Radom, L. *J. Am. Chem. Soc.* **1995**, 117, 2024; Norton, S. H.; Bachrach, S. M.; Hayes, J. M. *J. Org. Chem.* **2005**, 70, 5896; Bachrach, S. M.; Pereverzev, A. *Org. Biomol. Chem.* **2005**, 3, 2095; Bickelhaupt, F. M. *J. Comput. Chem.* **1999**, 20, 114.
- 4 Deng, L.; Branchadell, V.; Ziegler, T. *J. Am. Chem. Soc.* **1994**, 116, 10645.
- 5 Harder, S.; Streitwieser, A.; Petty, J. T.; Schleyer, P. v. R. *J. Am. Chem. Soc.* **1995**, 117, 3253.
- 6 Pierrefixe, S. C. A. H.; Fonseca Guerra, C.; Bickelhaupt, F. M. *Chem. Eur. J.* **2008**, 14, 819.
- 7 Carvalho, A. T. P.; Swart, M.; van Stralen, J. N. P.; Fernandes, P. A.; Ramos, M. J.; Bickelhaupt, F. M. *J. Phys. Chem. B* **2008**, 112, 2511.
- 8 Elschenbroich, C. *Organometallics*; Wiley-VCH: Weinheim, Germany, 2006; Sommer, L. H. *Stereochemistry, Mechanism and Silicon*; McGraw-Hill: New York, 1965; Holmes, R. R. *Chem. Rev.* **1990**, 90, 17; Damrauer, R.; Hankin, J. A. *Chem. Rev.* **1995**, 95, 1137; Dewar, M. J. S.; Healy, E. *Organometallics* **1982**, 1, 1705;

- Sheldon, J. C.; Hayes, R. N.; Bowie, J. H. *J. Am. Chem. Soc.* **1984**, *106*, 7711; Damrauer, R.; Burggraf, L. W.; Davis, L. P.; Gordon, M. S. *J. Am. Chem. Soc.* **1988**, *110*, 6601; Windus, T. L.; Gordon, M. S.; Davis, L. P.; Burggraf, L. W. *J. Am. Chem. Soc.* **1994**, *116*, 3568; Gronert, S.; Glaser, R.; Streitwieser, A. *J. Am. Chem. Soc.* **1989**, *111*, 3111; DePuy, C. H.; Bierbaum, V. M.; Flippin, L. A.; Grabowski, J. J.; King, G. K.; Schmitt, R. J.; Sullivan, S. A. *J. Am. Chem. Soc.* **1980**, *102*, 5012; Méndez, F.; Romero, M. D. L.; Gazquez, J. L. *J. Chem. Sci.* **2005**, *117*, 525; Hilderbrandt, R. L.; Homer, G. D.; Boudjouk, P. *J. Am. Chem. Soc.* **1976**, *98*, 7476; Shi, Z.; Boyd, R. J. *J. Phys. Chem.* **1991**, *95*, 4698; Bowie, J. H. *Acc. Chem. Res.* **1980**, *13*, 76; van der Wel, H.; Nibbering, N. M. M.; Sheldon, J. C.; Hayes, R. N.; Bowie, J. H. *J. Am. Chem. Soc.* **1987**, *109*, 5823; Couzijn, E. P. A.; Ehlers, A. W.; Schakel, M.; Lammertsma, K. *J. Am. Chem. Soc.* **2006**, *128*, 13634.
- 9 Hao, C.; Kaspar, J. D.; Check, C. E.; Lobring, K. C.; Gilbert, T. M.; Sunderlin, L. S. *J. Phys. Chem. A* **2005**, *109*, 2026.
- 10 Benin, V. A.; Martin, J. C.; Willcott, M. R. *Tetrahedron* **1997**, *53*, 10133.
- 11 Allan, R. E.; Beswick, M. A.; Davies, M. K.; Raithby, P. R.; Steiner, A.; Wright, D. S. *J. Organomet. Chem.* **1998**, *550*, 71.
- 12 Cayzergues, P.; Georgoulis, C.; Ville, G. *J. Chem. Res. (S)* **1978**, 325.
- 13 Glukhovtsev, M. N.; Pross, A.; Schlegel, H. B.; Bach, R. D.; Radom, L. *J. Am. Chem. Soc.* **1996**, *118*, 11258.
- 14 Uggerud, E.; Bache-Andreassen, L. *Chem. Eur. J* **1999**, *5*, 1917.
- 15 te Velde, G.; Bickelhaupt, F. M.; Baerends, E. J.; Fonseca Guerra, C.; van Gisbergen, S. J. A.; Snijders, J. G.; Ziegler, T. *J. Comput. Chem.* **2001**, *22*, 931; Baerends, E. J.; Ellis, D. E.; Ros, P. *Chem. Phys.* **1973**, *2*, 41.
- 16 Fonseca Guerra, C.; Snijders, J. G.; te Velde, G.; Baerends, E. J. *Theor. Chem. Acc.* **1998**, *99*, 391; Baerends, E. J.; Autschbach, J.; Bérces, A.; Berger, J. A.; Bickelhaupt, F. M.; Bo, C.; de Boeij, P. L.; Boerrigter, P. M.; Cavallo, L.; Chong, D. P.; Deng, L.; Dickson, R. M.; Ellis, D. E.; van Faassen, M.; Fan, L.; Fischer, T. H.; Fonseca Guerra, C.; van Gisbergen, S. J. A.; Groeneveld, J. A.; Gritsenko, O. V.; Grüning, M.; Harris, F. E.; van den Hoek, P.; Jacob, C. R.; Jacobsen, H.; Jensen, L.; Kadantsev, E. S.; van Kessel, G.; Klooster, R.; Kootstra, F.; van Lenthe, E.; McCormack, D. A.; Michalak, A.; Neugebauer, J.; Nicu, V. P.; Osinga, V. P.; Patchkovskii, S.; Philipsen, P. H. T.; Post, D.; Pye, C. C.; Ravenek, W.; Romaniello, P.; Ros, P.; Schipper, P. R. T.; Schreckenbach, G.; Snijders, J.; Solà, M.; Swart, M.; Swerhone, D.; te Velde, G.; Vernooijs, P.; Versluis, L.; Visscher, L.; Visser, O.; Wang, F.; Wesolowski, T. A.; van Wezenbeek, E. M.; Wiesenekker, G.; Wolff, S. K.; Woo, T. K.; Yakovlev, A. L.; Ziegler, T.; *ADF2006.01*; SCM: Amsterdam, The Netherlands.

- 17 Bento, A. P.; Solà, M.; Bickelhaupt, F. M. *J. Comput. Chem.* **2005**, *26*, 1497; de Jong, G. Th.; Solà, M.; Visscher, L.; Bickelhaupt, F. M. *J. Chem. Phys.* **2004**, *121*, 9982; de Jong, G. Th.; Geerke, D. P.; Diefenbach, A.; Bickelhaupt, F. M. *Chem. Phys.* **2005**, *313*, 261; de Jong, G. Th.; Geerke, D. P.; Diefenbach, A.; Solà, M.; Bickelhaupt, F. M. *J. Comput. Chem.* **2005**, *26*, 1006; de Jong, G. Th.; Bickelhaupt, F. M. *J. Phys. Chem. A* **2005**, *109*, 9685; de Jong, G. Th.; Bickelhaupt, F. M. *J. Chem. Theory Comput.* **2006**, *2*, 322.
- 18 Handy, N. C.; Cohen, A. J. *Mol. Phys.* **2001**, *99*, 403; Lee, C.; Yang, W.; Parr, R. G. *Phys. Rev. B* **1988**, *37*, 785.
- 19 van Lenthe, E.; Baerends, E. J.; Snijders, J. G. *J. Chem. Phys.* **1994**, *101*, 9783.
- 20 Swart, M.; Ehlers, A. W.; Lammertsma, K. *Mol. Phys.* **2004**, *102*, 2467; Baker, J.; Pulay, P. *J. Chem. Phys.* **2002**, *117*, 1441; Xu, X.; Goddard III, W. A. *J. Phys. Chem. A* **2004**, *108*, 8495; Gonzales, J. M.; Allen, W. D.; Schaefer III, H. F. *J. Phys. Chem. A* **2005**, *109*, 10613; Grüning, M.; Gritsenko, O. V.; Baerends, E. J. *J. Phys. Chem. A* **2004**, *108*, 4459.
- 21 Fan, L.; Versluis, L.; Ziegler, T.; Baerends, E. J.; Ravenek, W. *Int. J. Quantum Chem. Quantum Chem. Symp.* **1988**, *S22*, 173.
- 22 Fan, L.; Ziegler, T. *J. Chem. Phys.* **1990**, *92*, 3645.
- 23 Fukui, K. *Acc. Chem. Res.* **1981**, *14*, 363.
- 24 Atkins, P. W. *Physical Chemistry*; Oxford University Press: Oxford, 1998.
- 25 Berry, R. S. *J. Chem. Phys.* **1960**, *32*, 933; Mislow, K. *Acc. Chem. Res.* **1970**, *3*, 321.
- 26 Ugi, I.; Maquarding, D.; Klusacek, H.; Gillespie, P. *Acc. Chem. Res.* **1971**, *4*, 288; Gillespie, P.; Hoffman, P.; Klusacek, H.; Maquarding, D.; Pfohl, S.; Ramirez, F.; Tsolis, E. A.; Ugi, A. *Angew. Chem.* **1971**, *83*, 691.
- 27 Bickelhaupt, F. M.; Ziegler, T.; Schleyer, P. v. R. *Organometallics* **1996**, *15*, 1477.
- 28 Computed as $\langle 3p \mid \sigma_{\text{A-Cl}}^* \rangle = [(\langle 3p_x \mid \sigma_{\text{A-Cl}}^* \rangle)^2 + (\langle 3p_y \mid \sigma_{\text{A-Cl}}^* \rangle)^2 + (\langle 3p_z \mid \sigma_{\text{A-Cl}}^* \rangle)^2]^{1/2}$.
- 29 Anh, N. T.; Minot, C. *J. Am. Chem. Soc.* **1980**, *102*, 103.

7 *Nucleophilicity and Leaving-Group Ability in Frontside and Backside S_N2 Reactions*

Adapted from

Bento, A. P.; Bickelhaupt, F. M. *J. Org. Chem.* **2008**, *73*, online

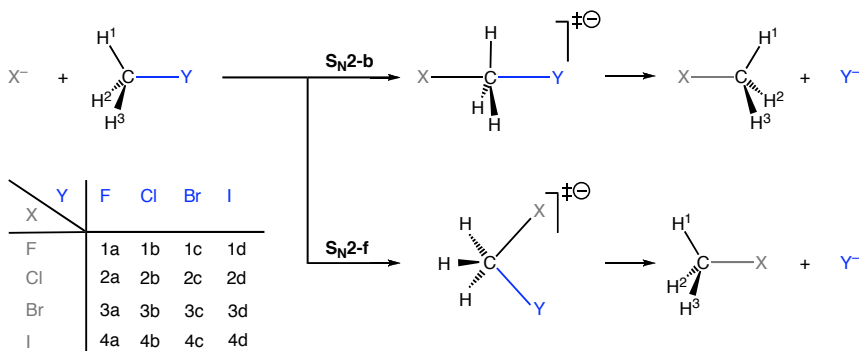
Abstract

Nucleophilic substitution is ubiquitous in chemistry, and well studied. Nucleophilicity and leaving-group ability have been related to various reactant properties, such as, electronegativity, size, polarizability and others. Yet, the state-of-the-art is to some extent still phenomenological. Here, we try to arrive at a straightforward, causal relationship between the reactants' electronic structure and their S_N2 reactivity. To this end, we have explored the potential energy surfaces of the backside as well as frontside S_N2 reactions of X⁻ + CH₃Y with X, Y = F, Cl, Br and I, using relativistic density functional theory (DFT) at ZORA-OLYP/TZ2P. These explorations provide us with a consistent overview of trends, over a wide range of reactivities and pathways, which were analyzed using the Activation Strain model of chemical reactivity. A clear picture emerges from these analyses: nucleophilicity is determined by the electron-donor capability of the nucleophile (i.e., energy and shape of the X⁻ *np* atomic orbital) and leaving-group ability derives directly from carbon–leaving-group (C–Y) bond strength.

7.1. Introduction

Bimolecular nucleophilic substitution (S_N2 , see Scheme 7.1) reactions feature in many routes in organic synthesis.¹ Over the past decades, various experimental and theoretical studies have been conducted to explore trends in reactivity as well as the nature of the S_N2 potential energy surface (PES).²⁻⁸ In the late seventies, Olmstead and Brauman⁷ proposed the double-well PES for gas-phase S_N2 reactions which is characterized by reactant and product complexes (RC, PC) that are separated by a central transition state (TS). This is shown in Scheme 7.2 for a thermoneutral ($X = Y$) as well as an exothermic ($X \neq Y$) S_N2 reaction. The barrier in the latter may disappear if the process becomes sufficiently exothermic, as shown in Scheme 7.2c.

Scheme 7.1. Model reaction systems.

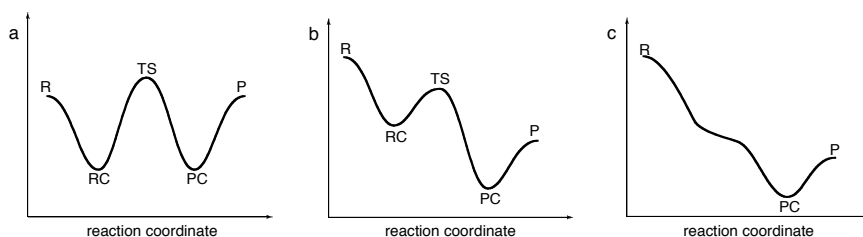


Many factors play a role in determining the efficiency of an S_N2 reaction, for example, the steric demand and/or effective electronegativity of the substituents at the central carbon atom (or in the nucleophile and leaving group) or the central atom itself which may be, e.g., N, Si, P or S instead of C. The regular backside S_N2 -b substitution, which goes with inversion of configuration at carbon (cf. Walden inversion), is in general significantly more efficient, i.e., has a lower reaction barrier, than the corresponding frontside S_N2 -f pathway, which goes with retention of configuration. The nature of condensed-phase S_N2 mechanisms furthermore strongly depends on solvation effects.

In the present study, we focus on yet two other factors, namely, nucleophilicity and leaving-group ability. These properties refer to how good a nucleophile or leaving group is in the sense of yielding a low barrier to S_N2 substitution. Nucleophilicity and leaving-group ability have been related to various properties of X^- and Y^- (Scheme 7.1), such as, electronegativity, size, polarizability and others. Yet, the state-of-the-art is to some extent still phenomenological.^{1,9} Here, we try to arrive at a straightforward, causal relationship between the reactants' electronic structure and their S_N2 reactivity. To this end, we have

explored the potential energy surfaces of the backside (S_N2 -b) as well as frontside (S_N2 -f) nucleophilic substitution reactions of $X^- + CH_3Y$ with X and $Y = F, Cl, Br$ and I , using relativistic density functional theory (DFT) at ZORA-OLYP/TZ2P as implemented in the Amsterdam Density Functional (ADF) program. Scheme 7.1 provides an overview of all model systems and our nomenclature.

Scheme 7.2. S_N2 potential energy surfaces: (a) thermoneutral, (b) exothermic with central barrier, (c) exothermic without central barrier (R, RC, TS, PC, P stands for reactants, reactant complex, transition state, product complex and products, respectively).



The explorations of our S_N2 -b and S_N2 -f model reactions provide us with an overview of trends in reaction energies and barriers, over a wide range of reactivities and pathways, all obtained consistently with one and the same method. This nicely augments the existing experimental and theoretical data and constitutes an objective on its own. But the main purpose, as pointed out above, is to obtain a qualitative, physical understanding of the trends in reactivity and, in particular, the concepts of nucleophilicity and leaving-group ability. This is achieved through an analysis of the PESes using the Activation Strain model of chemical reactivity in which the potential energy surface $\Delta E(\zeta)$ is decomposed, along the reaction coordinate ζ , into the strain $\Delta E_{\text{strain}}(\zeta)$ associated with deforming the individual reactants plus the actual interaction $\Delta E_{\text{int}}(\zeta)$ between the deformed reactants: $\Delta E(\zeta) = \Delta E_{\text{strain}}(\zeta) + \Delta E_{\text{int}}(\zeta)$ (see Chapter 2 for details).

A clear picture emerges from these analyses. They show that nucleophilicity is determined in a straightforward manner by the electron-donor capability of the nucleophile (i.e., energy and shape of the X^- np atomic orbital) while leaving-group ability derives directly from the carbon–leaving-group ($C-Y$) bond strength.

7.2. Methods

7.2.1. Computational Details

All calculations were performed with the Amsterdam Density Functional (ADF) program developed by Baerends and others.^{10,11} The molecular orbitals (MOs) were expanded in a large uncontracted set of Slater-type orbitals (STOs) containing diffuse functions, TZ2P.

This basis is of triple- ζ quality and has been augmented by two sets of polarization functions: $2p$ and $3d$ on hydrogen, $3d$ and $4f$ on carbon, fluorine and chlorine, $4d$ and $4f$ on bromine and $5d$ and $4f$ on iodine. The core shells of carbon ($1s$), fluorine ($1s$), chlorine ($1s2s2p$), bromine ($1s2s2p3s3p$) and iodine ($1s2s2p3s3p3d4s4p$) were treated by the frozen-core approximation.¹¹ An auxiliary set of s , p , d , f and g STOs was used to fit the molecular density and to represent the Coulomb and exchange potentials accurately in each SCF cycle. Relativistic effects were accounted for by using the zeroth-order approximation (ZORA).¹²

Equilibrium and transition-state geometries were fully optimized at the OLYP¹³ density functional, which involves Handy's optimized exchange, OPTX. This level of theory was previously shown to agree satisfactorily with highly correlated *ab initio* benchmarks¹⁴ (see also Chapters 3 and 4). All stationary points were confirmed by vibrational analysis:¹⁵ for equilibrium structures all normal modes have real frequencies whereas transition states¹⁶ have one normal mode with an imaginary frequency. Furthermore, transition states were verified to connect the supposed reactant and product minima by carrying out intrinsic reaction coordinate (IRC) calculations.¹⁷

7.2.2. Analysis of the Potential Energy Surfaces

Insight into how the activation barriers arise was obtained using the Activation Strain model of chemical reactivity (see Chapter 2). In this model, the potential energy surface $\Delta E(\zeta)$ is decomposed, along the reaction coordinate ζ , into the strain $\Delta E_{\text{strain}}(\zeta)$ associated with deforming the individual reactants, plus the actual interaction $\Delta E_{\text{int}}(\zeta)$ between the deformed reactants:

$$\Delta E(\zeta) = \Delta E_{\text{strain}}(\zeta) + \Delta E_{\text{int}}(\zeta) \quad (7.1)$$

The strain $\Delta E_{\text{strain}}(\zeta)$ is determined by the rigidity of the reactants and on the extent to which groups must reorganize in a particular reaction mechanism, whereas the interaction $\Delta E_{\text{int}}(\zeta)$ between the reactants depends on their electronic structure and on how they are mutually oriented as they approach each other. In the present study, the reactants are one of the halide nucleophiles X^- and either one of the halomethane substrates CH_3Y .

7.3. Results and Discussion

7.3.1. Reaction Profiles Backside S_N2 -b

The results of our ZORA-OLYP/TZ2P calculations are collected in Table 7.1 (energies) and Figures 7.1 - 7.4 (geometries). The CH_3Y substrates, which are not contained in Figures 7.1 - 7.4, have C–Y bond distances of 1.396 Å (C–F), 1.791 Å (C–Cl), 1.959 Å (C–Br) and 2.157 Å (C–I).

Table 7.1. Energies (in kcal/mol) relative to the reactants of the stationary points occurring in backside and frontside S_N2 reactions of $\text{X}^- + \text{CH}_3\text{Y}$.^[a]

| X | species | Y = | F a | Cl b | Br c | I d |
|---------|-------------|-----|-------------|--------------|-------------|-------------|
| F 1 | RC-b | | –15.7 | –19.4 | [b] | [b] |
| | TS-b | | –7.6 | –19.2 | [b] | [b] |
| | PC-b | | –15.7 | –43.6 | –51.9 | –57.8 |
| | P | | 0.0 | –36.0 | –45.8 | –52.5 |
| | TS-H | | –15.5 | –19.0 | –21.0 | –22.7 |
| | RC-f | | –17.5 | –21.3 | –22.8 | –24.5 |
| | TS-f | | 33.4 | 19.4 | 12.7 | 7.9 |
| | PC-f | | –17.5 | [b] | [b] | [b] |
| Cl 2 | RC-b | | –7.6 | –9.0 | –10.0 | –10.8 |
| | TS-b | | 16.8 | –0.2 | –5.6 | –8.6 |
| | PC-b | | 16.7 | –9.0 | –17.0 | –22.6 |
| | P | | 36.0 | 0.0 | –9.7 | –16.5 |
| | TS-H | | 17.1 | [b] | [b] | [b] |
| | RC-f | | [b] | [b] | [b] | [b] |
| | TS-f | | 55.4 | 40.2 | 33.5 | 28.9 |
| | PC-f | | 14.8 | [b] | [b] | [b] |
| Br 3 | RC-b | | –6.2 | –7.3 | –8.0 | –8.6 |
| | TS-b | | [b] | 4.1 | –1.7 | –5.0 |
| | PC-b | | [b] | –0.2 | –8.0 | –13.4 |
| | P | | 45.8 | 9.7 | 0.0 | –6.7 |
| | TS-H | | 24.8 | [b] | [b] | [b] |
| | RC-f | | [b] | [b] | [b] | [b] |
| | TS-f | | 58.4 | 43.3 | 36.6 | 32.0 |
| | PC-f | | 22.9 | [b] | [b] | [b] |
| I 4 | RC-b | | –5.2 | –6.2 | –6.7 | –7.3 |
| | TS-b | | [b] | 7.9 | 1.8 | –1.9 |
| | PC-b | | [b] | 5.7 | –1.9 | –7.3 |
| | P | | 52.5 | 16.5 | 6.7 | 0.0 |
| | TS-H | | 29.8 | [b] | [b] | [b] |
| | RC-f | | [b] | [b] | [b] | [b] |
| | TS-f | | 60.4 | 45.4 | 38.8 | 34.2 |
| | PC-f | | 28.0 | [b] | [b] | [b] |

[a] Computed at ZORA-OLYP/TZ2P. See Scheme 7.1 for numbering species. [b] Nonexistent.

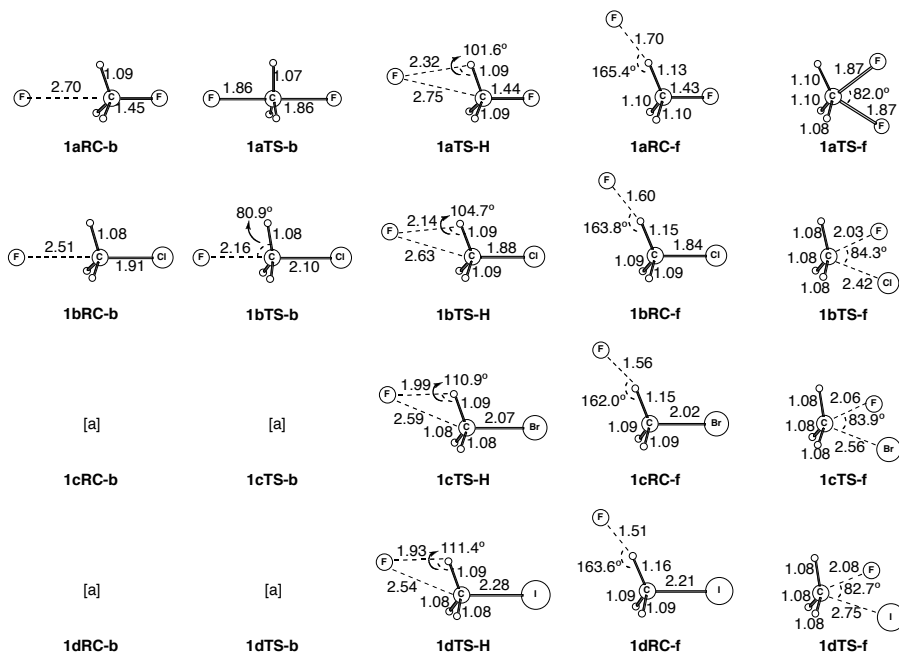


Figure 7.1. Structures (in Å, deg.) of stationary points in backside and frontside S_N2 reactions 1a-d of F^- + CH_3Y , computed at ZORA-OLYP/TZ2P. [a] Nonexistent.

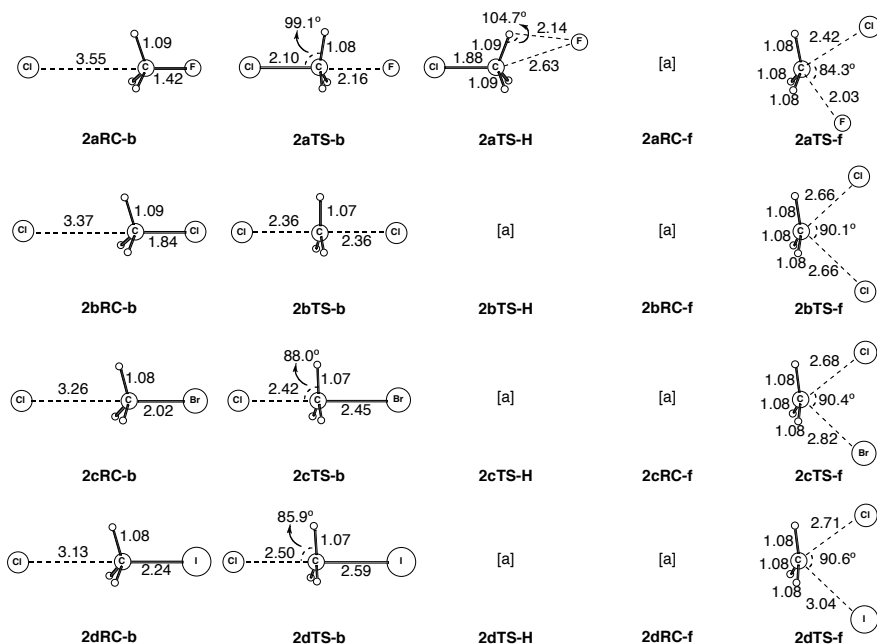


Figure 7.2. Structures (in Å, deg.) of stationary points in backside and frontside S_N2 reactions 2a-d of Cl^- + CH_3Y , computed at ZORA-OLYP/TZ2P. [a] Nonexistent.

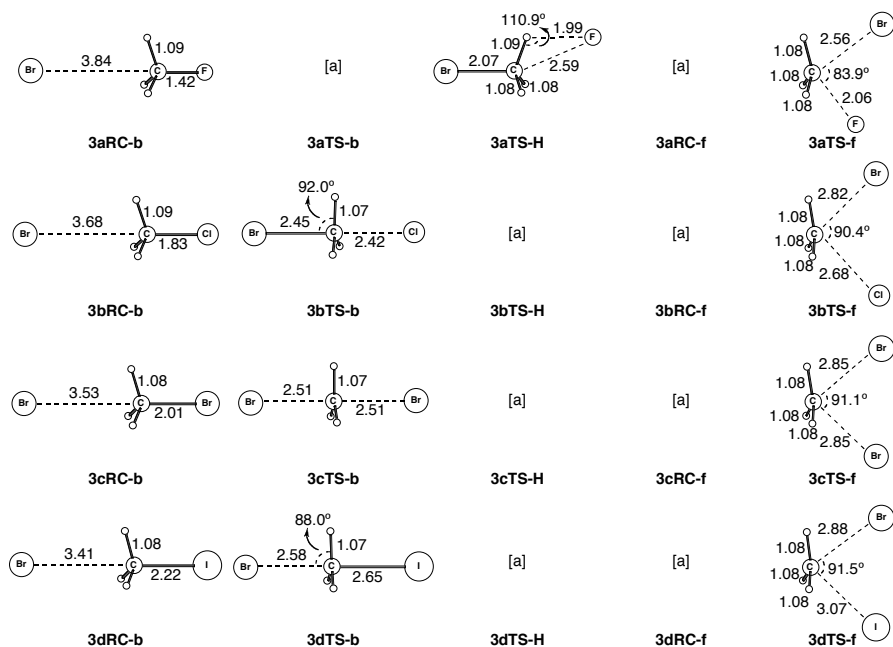


Figure 7.3. Structures (in Å, deg.) of stationary points in backside and frontside S_N2 reactions 3a-d of $\text{Br}^- + \text{CH}_3\text{Y}$, computed at ZORA-OLYP/TZ2P. [a] Nonexistent.

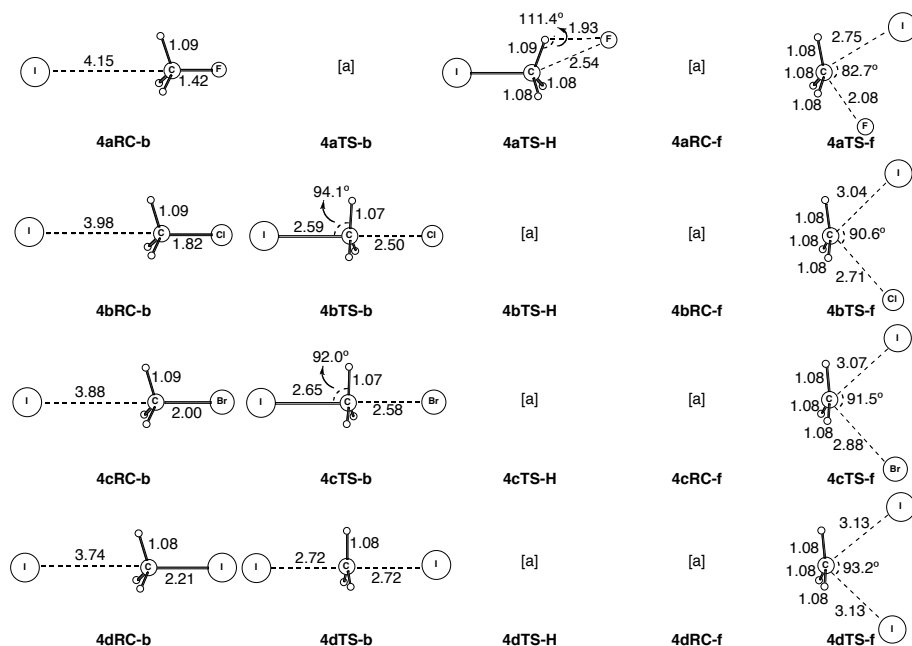


Figure 7.4. Structures (in Å, deg.) of stationary points in backside and frontside S_N2 reactions 4a-d of $\text{I}^- + \text{CH}_3\text{Y}$, computed at ZORA-OLYP/TZ2P. [a] Nonexistent.

Most but not all of our model backside S_N2 -b reactions (see Scheme 7.1) proceed via a double-well PES involving a central barrier and transition state (TS-b) as shown in Scheme 7.2a and 7.2b. We begin our exploration of reactivity with the trends along the backside S_N2 -b substitutions in two series of reaction systems: 1b - 4b, in which the chloride nucleophile reacts with the four different halomethanes, and 2a - 2d, in which the four different halide nucleophiles react with chloromethane (see Scheme 7.1). Note that the two orthogonal series have the well-known $Cl^- + CH_3Cl$ reaction (2b) in common. The reactant and product complexes that are connected by the backside S_N2 -b transition states in these two series are C_{3v} symmetric with a linear $X\cdots C-Y$ arrangement. They are stabilized with respect to the reactants and products, respectively, by 6 to 19 kcal/mol (see Table 7.1).

As the nucleophile in $X^- + CH_3Cl$ is varied along $X^- = F^-, Cl^-, Br^-$ and I^- , the overall barrier (i.e., the energy of the TS-b relative to reactants R) increases monotonically from -19.2 to -0.2 to +4.1 to +7.9 kcal/mol, respectively (see Table 7.1, S_N2 -b reactions 1b, 2b, 3b, 4b). Likewise, the central barrier (i.e., the energy of the TS-b relative to reactant complex RC-b) increases monotonically (from +0.2 to +8.8 to +11.4 to +14.1 kcal/mol, respectively) and the reaction energy changes from exothermic to increasingly endothermic (from -36.0 to 0.0 to +9.7 to +16.5 kcal/mol, respectively). Also the structural trends are nicely systematic with a TS-b for $X^- + CH_3Cl$ that becomes more and more product like along $X^- = F^-, Cl^-, Br^-$ and I^- , with an increasingly stretched carbon-leaving-group (C-Cl) bond of 2.10, 2.36, 2.42 and 2.50 Å, respectively (see Figures 7.1 - 7.4).

On the other hand, variation of the leaving group in $Cl^- + CH_3Y$ along $Y = F, Cl, Br$ and I causes the overall barrier to monotonically *decrease* from +16.8 to -0.2 to -5.6 to -8.6 kcal/mol (see Table 7.1, S_N2 -b reactions 2a, 2b, 2c, 2d). And again, the central barrier shows the same behavior: it decreases from +24.4 to +8.8 to +4.4 to +2.2 kcal/mol, respectively.

Similar trends occur along all other series of S_N2 -b reaction systems: for a given leaving group, barriers increase as the nucleophile goes from fluoride to iodide; and for a given nucleophile, they decrease as the leaving group varies from fluorine to iodine. The two trends approximately cancel each other if both nucleophile and leaving group are symmetrically varied in $X^- + CH_3X$ along $X = F, Cl, Br$ and I : here, the overall barrier, for example, changes less, namely, from -7.6 to -0.2 to -1.7 to -1.9 kcal/mol, respectively (see Table 7.1, S_N2 -b reactions 1a, 2b, 3c, 4d).

If the reaction exceeds a certain exothermicity (1c, 1d) or endothermicity (3a, 4a), the TS merges with the RC or PC, respectively (see Table 7.1). Consequently, the central barrier disappears in for $F^- + CH_3Br$ or CH_3I (and the reverse S_N2 -b reactions) and the reaction profile changes from double-well to single-well PES (see Scheme 7.2c).

7.3.2. Reaction Profiles Frontside S_N2 -f

All of our frontside S_N2 -f reactions are characterized by a double-well PES involving a central barrier and transition state (TS-f) as shown in Scheme 7.2a and 7.2b. They proceed from and to the same reactant (RC-b) and product complexes (PC-b), respectively, as the backside S_N2 -b reactions, unless such a complex involves a fluoride anion. In the latter case, the minimum energy path leads from the frontside transition state (TS-f) to separate frontside reactant (RC-f) or product complexes (PC-f) in which fluoride forms an $F^{\cdots}H-C$ hydrogen bond with the methyl group of the neutral halomethane fragment (see Figures 7.1 - 7.4). Such a frontside complex has been reported also by Angel and Ervin² for the reaction of $F^- + CH_3Cl$.

The alternative "frontside complexes" RC-f and PC-f are about 2 kcal/mol more stable than the C_{3v} symmetric backside complexes RC-b and PC-b which are separated by slight barriers (TS-H) of only a few kcal/mol from the former (see Table 7.1). In the case of the single-well reactions of $F^- + CH_3Br$ or CH_3I (1c, 1d) and Br^- or $I^- + CH_3F$ (3a, 4a), in which the backside ion-molecule complexes are nonexistent as stable stationary points, the transition states TS-H separate the frontside complexes from the barrier-free backside substitution process.

The barriers of the frontside S_N2 -f reactions are consistently higher by 36 – 41 kcal/mol than those of the backside S_N2 -b reactions. Note however that the trends in reactivity for S_N2 -f and S_N2 -b are essentially equal. Thus, as the nucleophile in $X^- + CH_3Cl$ is varied along $X^- = F^-, Cl^-, Br^-$ and I^- , the overall frontside barrier (i.e., the energy of the TS-f relative to reactants R) increases monotonically from +19.4 to +40.2 to +43.3 to +45.4 kcal/mol, respectively (see Table 7.1, S_N2 -f reactions 1b, 2b, 3b, 4b). Also the structural trends are nicely systematic with a TS-f for $X^- + CH_3Cl$ that becomes more and more product like along $X^- = F^-, Cl^-, Br^-$ and I^- , with an increasingly stretched carbon-leaving-group (C-Cl) bond of 2.42, 2.66, 2.68 and 2.71 Å, respectively (see Figures 7.1 - 7.4). Note that these C-Cl bonds in the various TS-f are consistently longer by 0.2 – 0.3 Å than those in the corresponding TS-b.

On the other hand, variation of the leaving group in $Cl^- + CH_3Y$ along $Y = F, Cl, Br$ and I causes the frontside overall barrier to monotonically *decrease* from +55.4 to +40.2 to +33.5 to +28.9 kcal/mol (see Table 7.1, S_N2 -f reactions 2a, 2b, 2c, 2d).

Similar trends occur along all other series of S_N2 -f reaction systems: for a given leaving group, barriers increase as the nucleophile goes from fluoride to iodide; and for a given nucleophile, they decrease as the leaving group varies from fluorine to iodine. Again, as in the case of the backside reactions, the two trends approximately cancel each other if both nucleophile and leaving group are symmetrically varied in $X^- + CH_3X$ along $X = F, Cl, Br$ and I : here, the frontside overall barrier, for example, changes less, namely,

from +33.4 to +40.2 to +36.6 to +34.2 kcal/mol, respectively (see Table 7.1, S_N2-f reactions 1a, 2b, 3c, 4d).

7.3.3. Activation Strain Analyses: Nucleophilicity in S_N2-b

Next, we address the main purpose of our study: to understand *why*, for a given leaving group, the S_N2 barrier increases as the nucleophile goes from fluoride to iodide and *why*, for a given nucleophile, it decreases as the leaving group varies from fluorine to iodine. A model for arriving at such understanding emerges from our Activation Strain analyses^{5,18} in which the potential energy surface $\Delta E(\zeta)$ of the model reactions is decomposed, along the reaction coordinate ζ , into the strain $\Delta E_{\text{strain}}(\zeta)$ associated with deforming the individual reactants plus the actual interaction $\Delta E_{\text{int}}(\zeta)$ between the deformed reactants (see eq 7.1; see also Chapter 2). The analysis results of the backside S_N2-b and frontside S_N2-f reactions are collected and visualized in Figures 7.5 and 7.6, respectively, which show potential energy surfaces $\Delta E(\zeta)$ (bold lines), strain energies $\Delta E_{\text{strain}}(\zeta)$ (plain lines) and interaction energies $\Delta E_{\text{int}}(\zeta)$ (dashed lines). Both figures are divided into a left and a right panel. The left panel addresses trends in nucleophilicity and contains four diagrams showing for each of the four leaving groups Y how the situation changes along the nucleophiles X[−] = F[−], Cl[−], Br[−] and I[−]. In an analogous manner, the right panel addresses trends in leaving-group ability and contains four diagrams showing for each of the four nucleophiles X[−] how the situation changes along the leaving groups Y = F, Cl, Br and I. The color code in each of the subdiagrams of Figures 7.5 and 7.6 is black, blue, red and green as one goes along F, Cl, Br and I.

A surprisingly clear picture emerges from the Activation Strain analyses. They show that nucleophilicity is determined in a straightforward manner by the electron-donor capability of the nucleophile (i.e., energy and shape of the X[−] *np* atomic orbital) while leaving-group ability derives directly from the carbon–leaving-group (C–Y) bond strength. We first examine the trend in nucleophilicity along the four halide nucleophiles in backside S_N2-b reactions (Figure 7.5, left panel). We choose the reactions of X[−] + CH₃Cl for a detailed discussion but note that other leaving groups provide the same picture. Thus, as we go along X[−] = F[−], Cl[−], Br[−] and I[−], we can see that the reaction profile ΔE becomes more and more destabilized and the transition states (indicated by bullets) occur at still higher energies (see Figure 7.5b). Interestingly, this trend stems entirely from the interaction curves ΔE_{int} while the strain curves ΔE_{strain} of the four different reaction systems are nearly identical and superimposed (see Figure 7.5b). We come back to the strain curves ΔE_{strain} in Section 7.3.4, where we discuss trends in leaving-group ability.

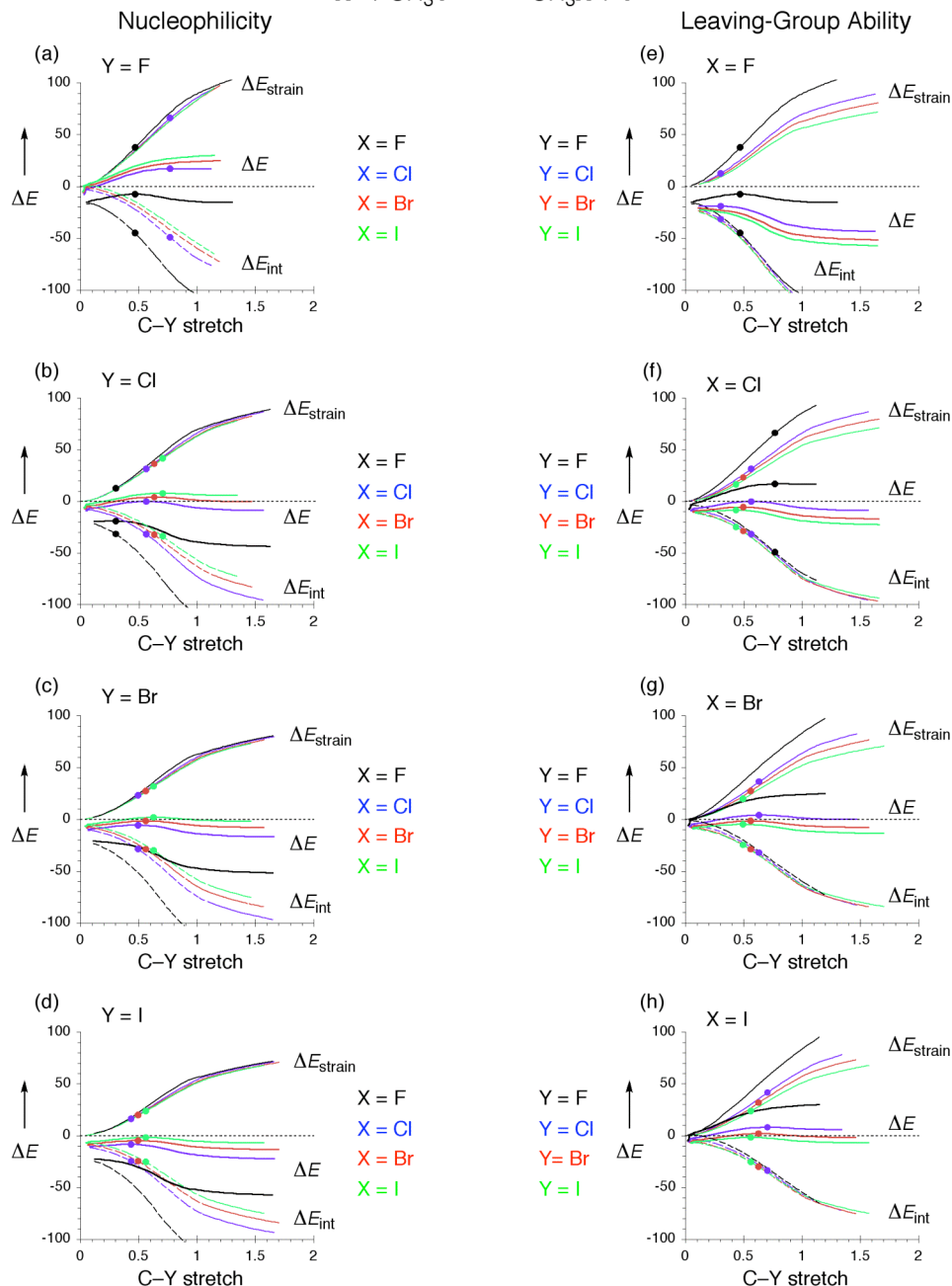
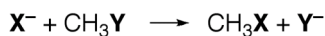


Figure 7.5. Activation-strain analysis of backside $\text{S}_{\text{N}}2$ reaction profiles (in kcal/mol) along the reaction coordinate projected onto the C-Y stretch (in Å). Left panel: variation of nucleophile X^- for fixed leaving group Y. Right panel: variation of leaving group Y for fixed nucleophile X^- . Bullets indicate TSs.

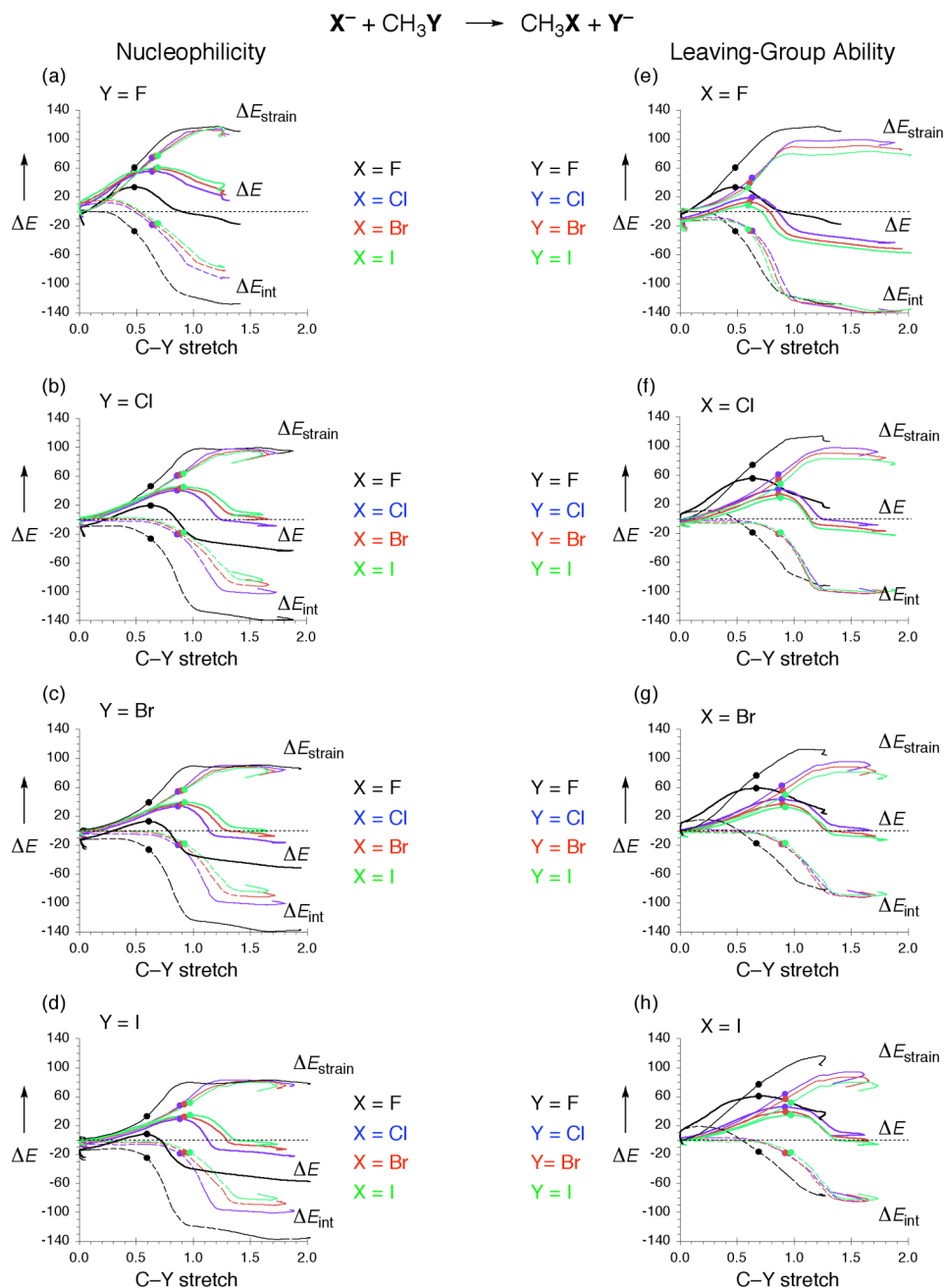


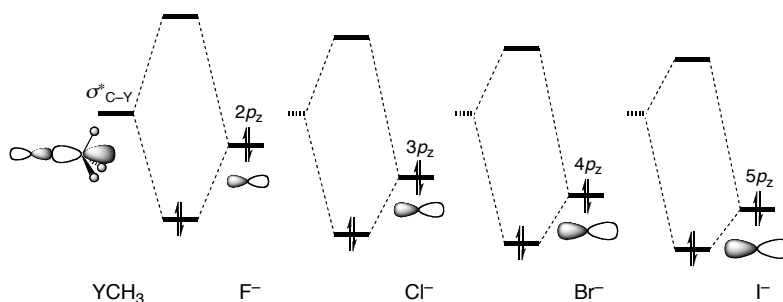
Figure 7.6. Activation-strain analysis of frontside S_N2 reaction profiles (in kcal/mol) along the reaction coordinate projected onto the C-Y stretch (in Å). Left panel: variation of nucleophile X^- for fixed leaving group Y . Right panel: variation of leaving group Y for fixed nucleophile X^- . Bullets indicate TSs.

Note also that, if we go from $X^- = F^-$ to Cl^- to Br^- and to I^- , the transition states occur at still later points along the reaction coordinate (i.e., for larger C–Y stretch). This phenomenon, which is reminiscent of the Hammond postulate¹⁹ ("more endothermic reactions have more product like transition states"), is the logical consequence of the fact that the transition state occurs at that point along the reaction coordinate ξ where $d\Delta E_{\text{int}}(\xi)/d\xi = -d\Delta E_{\text{strain}}(\xi)/d\xi$. Thus, as the $\Delta E_{\text{int}}(\xi)$ curve becomes less stabilizing, its slope also diminishes and the aforementioned condition is satisfied at a later, more product-like point along ξ .

We continue with the trend along interaction curves ΔE_{int} as they determine the trend along the nucleophiles. An analysis of the bonding mechanism behind this interaction curve shows that the dominant orbital interaction is the HOMO–LUMO interaction between the occupied $X^- np$ AO pointing to the backside lobe of the empty CH_3Y σ^*_{C-Y} orbital. In all of the reactions, the interaction curve ΔE_{int} is stabilized as reaction proceeds and the C–Y bond elongates. One reason is that the methyl group becomes more positively charged which leads to a better electrostatic attraction ΔV_{elstat} . The other important reason is that the C–Y antibonding σ^*_{C-Y} goes down in energy (smaller HOMO–LUMO gap) and gains more amplitude on the more electropositive methyl end of the substrate (better HOMO–LUMO overlap).

Importantly, regarding the trend in nucleophilicity, this HOMO–LUMO interaction becomes less stabilizing as the nucleophile is varied along $X^- = F^-$, Cl^- , Br^- and I^- which causes the observed destabilization in the ΔE_{int} curve and thus the overall reaction profile ΔE . The reason is that the orbital energy of the $X^- np$ AO decreases in this order which causes the HOMO–LUMO gap to become larger and thus the orbital interaction ΔE_{oi} less stabilizing (see qualitative illustration in Scheme 7.3).

Scheme 7.3. HOMO–LUMO interaction of $X^- = F^-$, Cl^- , Br^- and I^- with a halomethane CH_3Y .



Note that this trend in orbital energies of the halide anions X^- runs counter to that in the neutral halogen atoms X . In the latter, the energy of the electronegative F $2p$ AO is lowest and as the principal quantum number increases down the periodic table, the

valence Cl 3p, Br 4p and I 5p AOs become effectively more shielded and higher in energy. This is the orbital picture of the decreasing electronegativity along this series of halogens. However, if we put an excess electron on the halogens, the small and compact fluorine AOs experience more Coulomb repulsion and destabilization than in the case of the heavier and more diffuse halogens which leads to the reversed trend in AO energies for the halide anions.

In conclusion, nucleophilicity is determined in a straightforward manner by the electron-donor capability of the nucleophile, i.e., the energy (and shape; not discussed, here) of the X^- np atomic orbital. Thus, a higher X^- np orbital energy goes with a lower S_N2 barrier because of stronger, more stabilizing nucleophile–substrate interactions.

7.3.4. Activation Strain Analyses: Leaving-Group Ability in S_N2 -b

Next, we examine the trend in leaving-group ability along the four halomethane substrates in backside S_N2 -b reactions (Figure 7.5, right panel). We choose the reactions of $Cl^- + CH_3Y$ for a detailed discussion but note again that series with other nucleophiles provide the same picture. Thus, as we go along $Y = F, Cl, Br$ and I , we can see that the reaction profile ΔE becomes more and more *stabilized* and the transition states (indicated by bullets) occur at still lower energies along this series (see Figure 7.5f).

This time the trend stems entirely from the strain curves ΔE_{strain} while now the interaction curves ΔE_{int} of the four different reaction systems are nearly identical and superimposed (see Figure 7.5f). The strain curves ΔE_{strain} become systematically destabilized as the leaving group varies along $Y = F, Cl, Br$ and I . A closer look at the origin of this behavior shows that it is directly related to the trend in the C–Y bond strengths: the H_3C –Y bond dissociation energy amounts to 113.7, 83.8, 71.3 and 60.0 kcal/mol along this series (see also Ref. 6). In fact, the strain curves ΔE_{strain} are very similar to the simple bond dissociation energy curves of the halomethanes involved. They differ however increasingly from the latter as the reaction approaches completion. This is because in a simple dissociation, the halomethane transforms into a planar methyl radical plus a halogen atom whereas along the S_N2 -b reaction, the methyl moiety of the $[CH_3\cdots Y]$ fragment adopts eventually again an (inverted) pyramidal configuration.

We conclude that leaving-group ability derives directly from carbon–leaving-group (C–Y) bond strength. Thus, a stronger C–Y bond leads to a higher S_N2 barrier because of a higher, more *destabilizing* substrate strain.

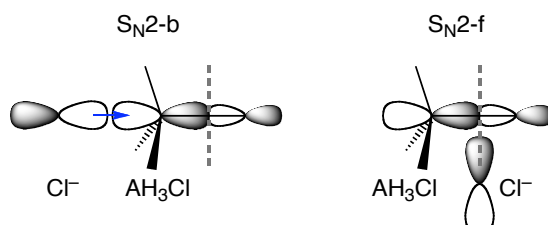
7.3.5. Activation Strain Analyses: S_N2 -f versus S_N2 -b

The frontside S_N2 -f barriers show, as pointed out above, the same trends as the backside ones: they increase along the nucleophiles F^- , Cl^- , Br^- and I^- and decrease along the

substrates CH_3F , CH_3Cl , CH_3Br and CH_3I . They also have the same two origins (compare the corresponding diagrams in Figures 7.5 and 7.6). Thus, a higher X^- np orbital energy goes with a lower $\text{S}_{\text{N}}2$ -f barrier because of stronger, more stabilizing nucleophile–substrate interactions ΔE_{int} (see Figure 7.6). On the other hand, a stronger $\text{C}-\text{Y}$ bond leads to a higher $\text{S}_{\text{N}}2$ -f barrier because of a higher, more *destabilizing* substrate strain ΔE_{strain} (see again Figure 7.6).

The higher frontside $\text{S}_{\text{N}}2$ -f as compared to backside $\text{S}_{\text{N}}2$ -b barriers have been previously attributed to less efficient $\langle \text{nucleophile HOMO} \mid \text{substrate LUMO} \rangle$ overlap and thus less stabilizing nucleophile–substrate interaction ΔE_{int} ²⁰ (see Scheme 7.4). Previously (see Chapter 6), we have shown this mechanism to be partially responsible for the higher $\text{S}_{\text{N}}2$ -f than $\text{S}_{\text{N}}2$ -b barrier for $\text{Cl}^- + \text{CH}_3\text{Cl}$.⁸ And here, we find that indeed also for all other combinations of $\text{X}^- + \text{CH}_3\text{Y}$, the interaction curves ΔE_{int} are less stabilizing in the early parts of the reaction process (up till the transition states) of the frontside substitutions (compare corresponding reaction systems in Figures 7.5 and 7.6). This constitutes a significant contribution to the higher energy of the frontside as compared to the backside reaction profiles ΔE .

Scheme 7.4. Overlap between X^- np HOMO and CH_3Y $\sigma_{\text{C}-\text{Y}}^*$ LUMO in $\text{S}_{\text{N}}2$ -b and $\text{S}_{\text{N}}2$ -f.



Interestingly, however, the main reason for the higher barrier for frontside substitution is the increased steric repulsion between nucleophile X and leaving group Y which are adjacent in the TS for frontside $\text{S}_{\text{N}}2$ -f while they are on opposite sides of the trigonal bipyramidal transition structure for backside $\text{S}_{\text{N}}2$ -b. The proximity of the two large X and Y groups in the frontside TS-f translates into a more deformed substrate in the frontside $\text{S}_{\text{N}}2$ -f processes and thus to the higher-energy strain curves ΔE_{strain} (compare Figures 7.5 and 7.6). This constitutes the main source of the higher-energy frontside reaction profiles ΔE . Note that this is also the reason for the above-mentioned larger $\text{C}-\text{X}$ and $\text{C}-\text{Y}$ distances in the frontside transition states TS-f as compared to the backside transition states TS-b (see Figures 7.1 - 7.4).

7.4. Conclusions

In conclusion, our analyses of the backside and frontside S_N2 reactions of $X^- + CH_3Y$ (X , Y = halogen), based on relativistic density functional theory, yield a consistent overview of trends and a clear picture of what makes a good or poor nucleophile or leaving group. In line with previous experimental and theoretical work, we find that backside S_N2 -b barriers increase along the nucleophiles F^- , Cl^- , Br^- and I^- and decrease along the substrates CH_3F , CH_3Cl , CH_3Br and CH_3I . Frontside S_N2 -f barriers show the same trends but are in all cases much higher (ca 10 – 60 kcal/mol) because of more steric repulsion as a result of the proximity between the nucleophile and leaving group.

Our analyses of these trends, based on the activation strain model of chemical reactivity (see eq 7.1 and Chapter 2 for details), yield a clear picture of what makes a good nucleophile or leaving group in the sense of yielding a low S_N2 barrier. Nucleophilicity is determined in a straightforward manner by the electron-donor capability of the nucleophile (i.e., energy and shape of the X^- np atomic orbital) whereas leaving-group ability derives directly from carbon–leaving-group (C–Y) bond strength.

Thus, a higher X^- np orbital energy goes with a lower S_N2 barrier (both backside and frontside) because of stronger, more stabilizing nucleophile–substrate interactions. On the other hand, a stronger C–Y bond leads to a higher S_N2 barrier (both backside and frontside) because of a higher, more *destabilizing* substrate strain. An interesting next step is to explore how the introduction of a solvent interferes with these basic principles. This will contribute to a more complete picture of the factors that determine relative rates of condensed-phase S_N2 reactions.

References

- 1 Smith, M. B.; March, J. *March's Advanced Organic Chemistry: Reactions, Mechanisms, and Structure*, Wiley, New York, **2007**; Carey, F. A.; Sundberg, R. J. *Advanced Organic Chemistry, Part A*, Springer, New York, **2007**; Lowry, T. H.; Richardson, K. S. *Mechanism and Theory in Organic Chemistry*, Harper and Row, New York, **1987**; Ingold, C. *Structure and Mechanism in Organic Chemistry*, Cornell University Press, Ithaca, NY, **1969**.
- 2 Angel, L. A.; Ervin, K. M. *J. Phys. Chem. A* **2001**, *105*, 4042.
- 3 Angel, L. A.; Ervin, K. M. *J. Phys. Chem. A* **2004**, *108*, 9827; Bach, R. D.; Dmitrenko, O.; Thorpe, C. *J. Org. Chem.* **2008**, *73*, 12; Botschwina, P. *Theor. Chem. Acc.* **1998**, *99*, 426; Carvalho, A. T. P.; Swart, M.; van Stralen, J. N. P.; Fernandes, P. A.; Ramos, M. J.; Bickelhaupt, F. M. *J. Phys. Chem. B* **2008**, *112*, 2511;

- Chabinyo, M. L.; Craig, S. L.; Regan, C. K.; Brauman, J. I. *Science* **1998**, 279, 1882; Chandrasekhar, J.; Smith, S. F.; Jorgensen, W. L. *J. Am. Chem. Soc.* **1985**, 107, 154; DePuy, C. H.; Gronert, S.; Mulin, A.; Bierbaum, V. M. *J. Am. Chem. Soc.* **1990**, 112, 8650; Glukhovtsev, M. N.; Pross, A.; Radom, L. *J. Am. Chem. Soc.* **1995**, 117, 2024; Glukhovtsev, M. N.; Pross, A.; Radom, L. *J. Am. Chem. Soc.* **1996**, 118, 6273; Glukhovtsev, M. N.; Pross, A.; Schlegel, H. B.; Bach, R. D.; Radom, L. *J. Am. Chem. Soc.* **1996**, 118, 11258; Gonzales, J. M.; Pak, C.; Cox, R. S.; Allen, W. D.; Schaefer III, H. F.; Császár, A. G.; Tarczay, G. *Chem. Eur. J.* **2003**, 9, 2173; Gronert, S. *Acc. Chem. Res.* **2003**, 36, 848; Harder, S.; Streitwieser, A.; Petty, J. T.; Schleyer, P. v. R. *J. Am. Chem. Soc.* **1995**, 117, 3253; Laerdahl, J. K.; Uggerud, E. *Int. J. Mass Spectrom.* **2002**, 214, 277; Lee, I.; Kim, C. K.; Sohn, C. K.; Li, H. G.; Lee, H. W. *J. Phys. Chem. A* **2002**, 106, 1081; Li, C.; Ross, P.; Szulejko, J. E.; McMahon, T. B. *J. Am. Chem. Soc.* **1996**, 118, 9360; Nibbering, N. M. M. *Acc. Chem. Res.* **1990**, 23, 279; Norton, S. H.; Bachrach, S. M.; Hayes, J. M. *J. Org. Chem.* **2005**, 70, 5896; Ren, Y.; Yamataka, H. *Chem. Eur. J.* **2007**, 13, 677; Schmatz, S. *ChemPhysChem* **2004**, 5, 600; Schmatz, S.; Botschwina, P.; Stoll, H. *Int. J. Mass Spectrom.* **2000**, 201, 277; Shaik, S. S.; Schlegel, H. B.; Wolfe, S. *Theoretical Aspects of Physical Organic Chemistry: The S_N2 Mechanism*, Wiley, New York, **1992**; Su, T.; Wang, H.; Hase, W. L. *J. Phys. Chem. A* **1998**, 102, 9819; van Bochove, M. A.; Bickelhaupt, F. M. *Eur. J. Org. Chem.* **2008**, 649; van Bochove, M. A.; Swart, M.; Bickelhaupt, F. M. *J. Am. Chem. Soc.* **2006**, 128, 10738; van Bochove, M. A.; Swart, M.; Bickelhaupt, F. M. *ChemPhysChem* **2007**, 8, 2452; Vayner, G.; Houk, K. N.; Jorgensen, W. L.; Brauman, J. I. *J. Am. Chem. Soc.* **2004**, 126, 9054; Wang, H.; Hase, W. L. *J. Am. Chem. Soc.* **1997**, 119, 3093; Wladkowski, B. D.; Allen, W. D.; Brauman, J. I. *J. Phys. Chem.* **1994**, 98, 13532; Uggerud, E. *Chem. Eur. J.* **2006**, 12, 1127.
- 4 Bento, A. P.; Bickelhaupt, F. M. *J. Org. Chem.* **2007**, 72, 2201.
 - 5 Bickelhaupt, F. M. *J. Comput. Chem.* **1999**, 20, 114.
 - 6 Deng, L.; Branchadell, V.; Ziegler, T. *J. Am. Chem. Soc.* **1994**, 116, 10645; Bickelhaupt, F. M.; Hermann, H.; Boche, G. *Angew. Chem.* **2006**, 118, 838; *Angew. Chem. Int. Ed.* **2006**, 45, 823.
 - 7 Olmstead, W. N.; Brauman, J. I. *J. Am. Chem. Soc.* **1977**, 99, 4219.
 - 8 Bento, A. P.; Bickelhaupt, F. M. *Chem. Asian J.* **2008**, 3, in press.
 - 9 According to the IUPAC Gold Book, nucleophilicity is the relative reactivity of nucleophilic reagent and the leaving-group ability (nucleofugality) is the tendency of atoms or groups to depart with the bonding electron pair.
 - 10 *Computer code ADF 2007.01*, Baerends, E. J.; Autschbach, J.; Bérces, A.; Berger, J. A.; Bickelhaupt, F. M.; Bo, C.; de Boeij, P. L.; Boerrigter, P. M.; Cavallo, L.;

- Chong, D. P.; Deng, L.; Dickson, R. M.; Ellis, D. E.; van Faassen, M.; Fan, L.; Fischer, T. H.; Fonseca Guerra, C.; van Gisbergen, S. J. A.; Groeneveld, J. A.; Gritsenko, O. V.; Grüning, M.; Harris, F. E.; van den Hoek, P.; Jacob, C. R.; Jacobsen, H.; Jensen, L.; Kadantsev, E. S.; van Kessel, G.; Klooster, R.; Kootstra, F.; van Lenthe, E.; McCormack, D. A.; Michalak, A.; Neugebauer, J.; Nicu, V. P.; Osinga, V. P.; Patchkovskii, S.; Philipsen, P. H. T.; Post, D.; Pye, C. C.; Ravenek, W.; Romaniello, P.; Ros, P.; Schipper, P. R. T.; Schreckenbach, G.; Snijders, J.; Solà, M.; Swart, M.; Swerhone, D.; te Velde, G.; Vernooijs, P.; Versluis, L.; Visscher, L.; Visser, O.; Wang, F.; Wesolowski, T. A.; van Wezenbeek, E. M.; Wiesenekker, G.; Wolff, S. K.; Woo, T. K.; Yakovlev, A. L.; Ziegler, T. SCM, Amsterdam, The Netherlands; Fonseca Guerra, C.; Snijders, J. G.; te Velde, G.; Baerends, E. J. *Theor. Chem. Acc.* **1998**, *99*, 391.
- 11 Baerends, E. J.; Ellis, D. E.; Ros, P. *Chem. Phys.* **1973**, *2*, 41; te Velde, G.; Bickelhaupt, F. M.; Baerends, E. J.; Fonseca Guerra, C.; van Gisbergen, S. J. A.; Snijders, J. G.; Ziegler, T. *J. Comput. Chem.* **2001**, *22*, 931.
- 12 van Lenthe, E.; Baerends, E. J.; Snijders, J. G. *J. Chem. Phys.* **1994**, *101*, 9783.
- 13 Handy, N. C.; Cohen, A. J. *Mol. Phys.* **2001**, *99*, 403; Lee, C.; Yang, W.; Parr, R. G. *Phys. Rev. B* **1988**, *37*, 785.
- 14 Baker, J.; Pulay, P. *J. Chem. Phys.* **2002**, *117*, 1441; Bento, A. P.; Solà, M.; Bickelhaupt, F. M. *J. Comput. Chem.* **2005**, *26*, 1497; Gonzales, J. M.; Allen, W. D.; Schaefer III, H. F. *J. Phys. Chem. A* **2005**, *109*, 10613; Grüning, M.; Gritsenko, O. V.; Baerends, E. J. *J. Phys. Chem. A* **2004**, *108*, 4459; Swart, M.; Ehlers, A. W.; Lammertsma, K. *Mol. Phys.* **2004**, *102*, 2467; Xu, X.; Goddard III, W. A. *J. Phys. Chem. A* **2004**, *108*, 8495.
- 15 Fan, L.; Versluis, L.; Ziegler, T.; Baerends, E. J.; Ravenek, W. *Int. J. Quantum Chem. Quantum Chem. Symp.* **1988**, *S22*, 173.
- 16 Fan, L.; Ziegler, T. *J. Chem. Phys.* **1990**, *92*, 3645.
- 17 Fukui, K. *Acc. Chem. Res.* **1981**, *14*, 363.
- 18 de Jong, G. Th.; Bickelhaupt, F. M. *ChemPhysChem* **2007**, *8*, 1170; Diefenbach, A.; Bickelhaupt, F. M. *J. Chem. Phys.* **2001**, *115*, 4030; Diefenbach, A.; de Jong, G. Th.; Bickelhaupt, F. M. *J. Chem. Theory Comput.* **2005**, *1*, 286.
- 19 Hammond, G. S. *J. Am. Chem. Soc.* **1955**, *77*, 334.
- 20 Anh, N. T.; Minot, C. *J. Am. Chem. Soc.* **1980**, *102*, 103.

Summary

In this thesis, a computational study on gas-phase nucleophilic substitution (S_N2) reactions using *ab initio* and density functional theory (DFT) calculations is presented. The purpose of the investigations is to obtain a deeper understanding of the nature of this important class of reactions, in particular, when it comes to the factors affecting their intrinsic reactivity, such as, the steric hindrance in the substrate, the center of nucleophilic attack and the nucleophilicity and leaving-group ability. The long-term goal is to contribute to a more rational and thus efficient design of chemical reactions.

After a general introduction in Chapter 1 and a brief description of the quantum theoretical methods used to perform these computational studies in Chapter 2, the performance of several popular density functionals in describing S_N2 substitution and E2 elimination reactions is evaluated and validated, in Chapters 3 and 4, against our *ab initio* benchmark potential energy surfaces for this class of reactions. Thus, in Chapter 3, *ab initio* benchmarks for the archetypal nucleophilic substitution of chloride at chloromethane ($S_N2@C$) and chlorosilane ($S_N2@Si$) have been computed. These benchmarks derive from a hierarchical series of methods up to CCSD(T)/aug-cc-pVQZ, which is converged with respect to the basis-set size within a few tenths of kcal/mol. This benchmark is then used to evaluate the performance of four popular density functionals, BP86, BLYP, B3LYP and OLYP, for describing the above $S_N2@C$ and $S_N2@Si$ substitution reactions. Interestingly, OLYP and B3LYP functionals perform satisfactorily with mean absolute errors in overall barrier of 2.2 and 2.4 kcal/mol, respectively, and in central barriers of 2.7 and 2.5 kcal/mol, respectively. However, the underestimation of the overall and central $S_N2@C$ barriers is more pronounced in the case of B3LYP (4.8 and 5.4 kcal/mol, respectively) than in the case of OLYP (2.5 and 4.1 kcal/mol).

In Chapter 4, similar *ab initio* benchmarks have been computed, although now for the archetypal competing E2 and S_N2 reactions of fluoride + fluoroethane and chloride + chloroethane. These benchmarks derive now from hierarchical series of methods up to CCSD(T)/aug-cc-pVQZ [up to CCSD(T)/aug-cc-pV(T + *d*)/Z for chloride + chloroethane], which are converged with respect to the basis-set size within less than half a kcal/mol. The resulting reaction profiles show that anti-E2 dominates for $F^- + CH_3CH_2F$ while S_N2 dominates for $Cl^- + CH_3CH_2Cl$. Our *ab initio* benchmark is then used to evaluate the performance of 31 density functionals for describing the above anti-E2, syn-E2 and S_N2 reactions. Best overall agreement regarding central reaction barriers

with our *ab initio* benchmark is obtained by representatives from each of the three categories of functionals, GGA, meta-GGA and hybrid DFT, with mean absolute errors of 4.3 (OPBE), 2.2 (M06-L) and 2.0 kcal/mol (M06), respectively. Importantly, the hybrid functional BHandH and the meta-GGA M06-L yield incorrect trends and qualitative features of the PESes (in particular, an erroneous preference for S_N2 over anti-E2 in the case of $F^- + CH_3CH_2F$) even though they are among the best functionals as measured by their small mean absolute errors of 3.3 and 2.2 kcal/mol in reaction barriers. OLYP and B3LYP have somewhat higher mean absolute errors in central barriers (5.6 and 4.8 kcal/mol, respectively) but the error distribution is somewhat more uniform and, as a consequence, the correct trends are reproduced.

From these studies, OLYP emerges as a sound and efficient approach for the routine investigation of trends, not only in nucleophilic substitutions but also in elimination reactions. For this reason, all calculations in Chapters 5, 6 and 7 were conducted using OLYP level of theory.

In Chapter 5, the potential energy surfaces (PES) of various $Cl^- + CR_3Cl$ ($R = H, CH_3$) and $Cl^- + SiR_3Cl$ model reactions ($R = H, CH_3, C_2H_5$ and OCH_3) have been investigated. It is textbook knowledge that $S_N2@C$ proceeds via a central reaction barrier, which disappears in the corresponding $S_N2@Si$. The purpose of this chapter is to understand why the central barrier disappears from $S_N2@C$ to $S_N2@Si$ despite the fact that these processes are isostructural and isoelectronic, and, in particular, which factors are responsible, in the first place, for the existence of a central S_N2 barrier. Our results show that the central barrier in S_N2 reactions is determined by the interplay of steric and electronic effects, such as, Pauli repulsion between the substituents (including nucleophile and leaving group) at the central atom and donor–acceptor orbital interactions between nucleophile and substrate. From $S_N2@C$ in $Cl^- + CH_3Cl$ to $S_N2@Si$ in $Cl^- + SiH_3Cl$, the central barrier disappears because there is less steric congestion and a more favorable interaction. But the central barrier reappears as the steric bulk around the silicon atom is raised. These results highlight the steric nature of the S_N2 barrier in general.

In Chapter 6, a computational study on the backside S_N2 -b and frontside S_N2 -f reactions of $Cl^- + AH_3Cl$ ($A = Si, Ge, Sn$ and Pb) is conducted. The purpose is, in the first place, to explore and understand how the reaction coordinate ζ and potential energy surfaces (PES) along ζ vary as the center of nucleophilic attack changes from carbon to the heavier group-14 atoms. A second issue is the question in how far the trends are influenced by relativistic effects, especially for the heaviest group-14 atoms. Our analyses show that the central barrier for backside S_N2 -b reaction of $Cl^- + AH_3Cl$ disappears as the central atom A goes from carbon to silicon and the heavier group-14 atoms (up till lead). This is because the steric congestion (and repulsion) decreases for

the larger central atoms and the orbital interactions become more stabilizing due to a better overlap between the chloride $3p_z$ HOMO and the substrate σ^*_{A-Cl} LUMO which obtains an increasingly extended amplitude on the more electropositive atom A. Furthermore, frontside S_N2-f substitution proceeds in *all* cases via a central barrier associated with a C_s symmetric pentavalent transition state that is significantly higher in energy than the corresponding transition species for backside S_N2-b reaction. One reason is the less efficient <chloride HOMO | substrate LUMO> overlap for S_N2-f . Interestingly, however, the main reason for the higher barrier for frontside substitution is the increased steric repulsion between nucleophile and leaving group which are adjacent in the transition state for frontside S_N2-f while they are on opposite sides of the trigonal bipyramidal transition structure for backside S_N2-b .

Finally, in Chapter 7, the concepts of nucleophilicity and leaving-group ability are examined through a detailed analysis of the backside S_N2-b and frontside S_N2-f reactions of $X^- + CH_3Y$ with $X, Y = F, Cl, Br$ and I . In line with previous experimental and theoretical work, it is found that backside S_N2-b barriers increase along the nucleophiles F^- , Cl^- , Br^- and I^- and decrease along the substrates CH_3F , CH_3Cl , CH_3Br and CH_3I . Frontside S_N2-f reactions show the same trends but are in all cases much (ca. 10–60 kcal/mol) higher. Our analyses of these trends, based on the Activation Strain model of chemical reactivity (see Section 2.3), yield a clear picture of what makes a good nucleophile or leaving group in the sense of yielding a low S_N2 barrier. Nucleophilicity is determined in a straightforward manner by the electron-donor capability of the nucleophile (i.e., energy and shape of the X^- np atomic orbital) whereas leaving-group ability derives directly from carbon–leaving-group ($C-Y$) bond strength.

Samenvatting

In dit proefschrift worden de resultaten gepresenteerd van een op *ab-initio*- en dichtheidsfunctionaal-theorie (DFT) gebaseerd computationeel onderzoek aan nucleofiele substitutiereacties (S_N2) in de gasfase. Het doel van dit onderzoek is het verkrijgen van meer inzicht in de aard van deze belangrijke klasse van reacties, in het bijzonder wat betreft de factoren die de intrinsieke reactiviteit bepalen, zoals sterische hindering, het centrum waarop de nucleofiele aanval plaatsvindt alsmede de nucleofiliciteit en nucleofugiciteit. Het lange-termijn-doel is een bijdrage te leveren aan een rationeler en daardoor efficiënter design van chemische reacties.

Na een algemene inleiding in hoofdstuk 1 en een korte beschrijving in hoofdstuk 2 van de gebruikte kwantumtheoretische methoden, wordt in hoofdstuk 3 en 4 de betrouwbaarheid van verscheidene populaire dichtheidsfunctionalen geëvalueerd m.b.t. de beschrijving van S_N2 - en E2-reacties, door een vergelijking met onze *ab-initio*-referentiewaarden voor de potentiaaloppervlakken van dit type reacties. In hoofdstuk 3 worden de *ab-initio*-referentiewaarden berekend voor de archetypische nucleofiele substitutie van chloride met chloormethaan ($S_N2@C$) en chloorsilaan ($S_N2@Si$). Deze referentiewaarden komen voort uit een hiërarchische reeks van methoden tot op het CCSD(T)/aug-cc-pVQZ-niveau. Deze reeks is tot op een paar tienden van een kcal/mol geconvergeerd m.b.t. de grootte van de basisset. De referentiewaarden worden vervolgens gebruikt om de prestatie af te schatten van vier populaire dichtheidsfunctionalen (BP86, BLYP, B3LYP en OLYP) voor het beschrijven van boven genoemde $S_N2@C$ - en $S_N2@Si$ -reacties. De OLYP- en B3LYP-functionalen blijken zeer bevredigend te presteren met *mean absolute errors* in overallbarrières van 2.2 respectievelijk 2.4 kcal/mol, en in centrale barrières van 2.7 respectievelijk 2.5 kcal/mol. De onderschatting van de *overall*- en centrale $S_N2@C$ -barrières is echter uitgesprokener in het geval van B3LYP (4.8 respectievelijk 5.4 kcal/mol) dan in het geval van OLYP (2.5 en 4.1 kcal/mol).

In hoofdstuk 4 zijn soortgelijke *ab-initio*-referentiewaarden berekend voor de archetypische concurrerende E2- en S_N2 -reacties van fluoride + fluorethaan en chloride + chloorethaan. Deze referentiewaarden komen nu voort uit een hiërarchische reeks van methoden tot op het CCSD(T)/aug-cc-pVQZ-niveau [dan wel tot het CCSD(T)/aug-cc-pV(T + *d*)Z-niveau voor chloride + chloorethaan]. Deze reeksen zijn tot op een halve kcal/mol geconvergeerd m.b.t. de grootte van de basisset. De resulterende

reactieprofielen laten zien dat anti-E2 dominant is voor $F^- + CH_3CH_2F$ terwijl S_N2 domineert in het geval van $Cl^- + CH_3CH_2Cl$. Vervolgens hebben we onze *ab-initio*-referentiewaarden gebruikt om 31 dichtheidsfunctionalen te evalueren m.b.t. hun prestaties bij het beschrijven van boven genoemde anti-E2-, syn-E2- en S_N2 -reacties. Over het geheel genomen de beste overeenstemming bij centrale reactiebarrières wordt verkregen door vertegenwoordigers uit elke van de drie categorieën functionalen (GGA, meta-GGA en hybride-DFT) met *mean absolute errors* van 4.3 (OPBE), 2.2 (M06-L) respectievelijk 2.0 kcal/mol (M06). Een belangrijk gegeven is dat de hybride-functionaal BHandH en de meta-GGA M06-L *foutieve* trends en kwalitatieve verkeerde vormen van het potentiaaloppervlak opleveren (met name een foutieve voorkeur voor S_N2 boven anti-E2 in het geval van $F^- + CH_3CH_2F$) ondanks dat zij zich onder de beste functionalen bevinden wat betreft hun kleine *mean absolute errors* van 3.3 en 2.2 kcal/mol in reactiebarrières. OLYP en B3LYP hebben iets hogere *mean absolute errors* in centrale barrières (5.6 respectievelijk 4.8 kcal/mol) maar de fout is iets homogener verdeeld, waardoor de correcte trends gereproduceerd worden.

Uit deze studies komt OLYP naar voren als een solide en efficiënte aanpak voor routinematig onderzoek naar trends, niet alleen in nucleofiele substituties maar ook in eliminatiereacties. Daarom zijn alle berekeningen in hoofdstukken 5, 6 en 7 uitgevoerd op het OLYP-niveau van DFT.

In hoofdstuk 5 zijn de potentiaaloppervlakken onderzocht van verschillende $Cl^- + CR_3Cl$ ($R = H, CH_3$) en $Cl^- + SiR_3Cl$ modelreacties ($R = H, CH_3, C_2H_5$ en OCH_3). Het is leerboekwijsheid dat $S_N2@C$ via een centrale reactiebarrière verloopt, welke in de overeenkomstige $S_N2@Si$ verdwijnt. Het doel van dit hoofdstuk is te begrijpen: (i) waarom de centrale barrière gaande van $S_N2@C$ naar $S_N2@Si$ verdwijnt, ondanks het feit dat deze processen isostructureel en isoëlectronisch zijn; en (ii) welke factoren er voor verantwoordelijk zijn dat er überhaupt een centrale S_N2 -barrière bestaat. Onze resultaten tonen aan dat de centrale barrière in S_N2 -reacties bepaald wordt door het samenspel van sterische en elektronische effecten, zoals Pauli-repulsie tussen de substituenten (inclusief nucleofiel en vertrekkende groep) aan het centrale atoom en donor-acceptor-orbitaal-wisselwerking tussen nucleofiel en substraat. Van $S_N2@C$ in $Cl^- + CH_3Cl$ naar $S_N2@Si$ in $Cl^- + SiH_3Cl$, verdwijnt de centrale barrière door een afname van de sterische verstopping en door een gunstigere (lees: sterker stabiliserende) wisselwerking tussen nucleofiel en substraat. De centrale barrière keert echter terug zodra de ruimtelijke afmetingen van de substituenten rond het siliciumatoom verder toenemen. Deze resultaten beklemtonen de sterische aard van de S_N2 -barrière in het algemeen.

In hoofdstuk 6 wordt een computationele studie uitgevoerd aan de *backside* S_N2 -b- en *frontside* S_N2 -f-reacties van $Cl^- + AH_3Cl$ ($A = Si, Ge, Sn$ en Pb). Het doel is in de eerste plaats om te verkennen en begrijpen hoe en waarom de reactiecoördinaat ζ en het

potentiaaloppervlak langs ζ variëren wanneer het centrum van de nucleofiele aanval verandert van koolstof naar de zwaardere groep-14-atomen. Een tweede punt is in hoeverre de trends beïnvloed worden door relativistische effecten, vooral bij de zwaarste groep-14-atomen. Onze analyses laten zien dat de centrale barrière voor de *backside* S_N2 -b-reactie van $Cl^- + AH_3Cl$ verdwijnt als het centrale atoom A van koolstof verandert naar silicium of één van de nog zwaardere groep-14-atomen (t/m lood). Dit is zo omdat de sterische verstopping en afstoting in het geval van de grotere centrale atomen afneemt en de orbitaalwisselwerking stabiliserender wordt t.g.v. een betere overlapping tussen de chloride $3p_z$ -HOMO en de substraat σ^*_{A-Cl} -LUMO die een steeds uitgestrektere amplitude op het electropositieve atoom A ontwikkelt. De *frontside* S_N2 -f-substitutie verloopt in *alle* gevallen via een centrale barrière, verbonden met een C_s -symmetrische, pentavalente overgangstoestand die significant hoger in energie is dan de overeenkomstige overgangsstructuren bij de *backside* S_N2 -b-reactie. Eén reden hiervoor is de minder efficiënte <chloride HOMO | substraat LUMO> overlap voor S_N2 -f. Interessant genoeg is de hoofdoorzaak voor de hogere barrière voor *frontside* substitutie echter de toegenomen sterische afstoting tussen nucleofiel en vertrekkende groep die in de overgangstoestand voor *frontside* S_N2 -f twee naburige posities innemen, terwijl ze zich aan weerszijden bevinden (en dus op grotere onderlinge afstand) in de trigonale bipyramidale overgangsstructuur van *backside* S_N2 -b.

Tenslotte worden in hoofdstuk 7 de concepten nucleofiliciteit en nucleofugiciteit onderzocht d.m.v. een gedetailleerde analyse van de *backside* S_N2 -b- en *frontside* S_N2 -f-reacties van $X^- + CH_3Y$ met $X, Y = F, Cl, Br$ en I . In overeenstemming met eerder experimenteel en theoretisch werk vinden wij dat *backside* S_N2 -b-barrières toenemen langs de reeks nucleofielen F^-, Cl^-, Br^- en I^- , en dat zij dalen langs de reeks substraten CH_3F, CH_3Cl, CH_3Br en CH_3I . *Frontside* S_N2 -f-reacties vertonen dezelfde trends, maar zijn in alle gevallen beduidend (ca. 10–60 kcal/mol) hoger. Onze analyses van deze trends, gebaseerd op het *Activation-Strain*-model van de chemische reactiviteit (zie Sectie 2.3), levert een helder beeld op van wat een goed nucleofiel of een goede vertrekkende groep is in de zin dat deze tot een lage S_N2 -barrière leiden. Nucleofiliciteit wordt direct bepaald door de elektronen-donorende capaciteit van het nucleofiel (d.w.z., energie en vorm van de X^- np atoomorbitaal) terwijl nucleofugiciteit een directe afgeleide is van de koolstof-vertrekkende-groep- (C–Y) bindingssterkte.

Acknowledgements

This thesis would not be possible without the help and support from many people, who directly or indirectly have contributed to this achievement.

Firstly, I would like to express my gratitude to my supervisor, Matthias Bickelhaupt, who gave me the opportunity to work under his supervision and benefit from his experience, knowledge and vision. Working on this interesting project with you has been truly rewarding and has allowed me to grow not only scientifically but also professionally. I really appreciated you sharing your expertise and research insight with me. Your enthusiasm and tenacity have kept me in the right path to this achievement. Thank you for always being there when I needed and for all the useful discussions.

I would also like to thank my promotor, Prof. Baerends, for also giving me the chance to work in such a leading-edge science group. Your kindness, knowledge and availability have been much appreciated throughout these years. Thank you for the valuable comments on my thesis.

I am also very grateful to Prof. Solà, for the fruitful collaboration, which resulted in two chapters of this thesis.

A special thanks also to Theodoor and Célia, with whom I shared the office for the last four years. Theodoor, thank you for introducing me to the ADF program and helping me solving a number of technical and scientific issues. Thanks also for getting me acquainted with the Dutch culture and politics. Thank you, Célia, for your kindness, friendship, willingness to help and for our conversations in Portuguese, which gave me the feeling of being closer to home. Obrigada por tudo!

A very special word also to Marc, who has always been there when I needed. Thank you for the useful discussions and for making the frustrating moments feel less harsh by turning them into moments of confidence and strength. I will always be grateful for your support and patience throughout these years. And I will always remember our Seinfeld moments. Big thanks also to Marcello, who helped me with every Macintosh-related problem and taught me most of the Macintosh world. Thanks for sharing your imagination and creativity whenever it was needed. Some of the funniest and artistic

ideas resulted in the coolest farewell gifts for former TC-members. Many thanks also to Simon, for the helpful discussions and for the great parties and barbecues that you and Daniel organized at your place. Thank you, guys, for your friendship and always welcoming me with a smile in your office and homes. I am also very grateful to Ivan for making me feel part of the group from the very beginning and to André for all the nice conversations about Brazil and Portugal.

I would like also to thank the SCM team (Stan, Olivier, Erik and Alexei), who were always available to help with any ADF-related problem and for always keeping us up-to-date with the new features of the program. Many thanks also to Marcel, for the useful discussions on technical and scientific issues. Thanks to Willem-Jan, for developing Pyfrag and make it available to all of us. Without it, finishing most of my projects would have been a lot harder. Thanks also to Drew, for the computer assistance.

Many thanks to Joost, Christoph, Johannes, Kasia, Daniel, Rosa, Paola (for the valuable help in parts of this thesis), Laura, Andreas (for the nice time in Chicago), Paul, Luuk, Manuel, Oleg, Leonardo, Jordi, Maya, Jetze, Pier, Klaas and all the rest of the (former) members and guests of the TC group for making the department such a nice and interesting place to work at and for the amusing lunches and coffee-breaks.

I am also greatly indebted to Paula, for always finding time to help me with all sorts of things. You are one of the reasons why the department runs so smoothly. Thanks so much for "sharing" Fu Wei with us. It was really nice to get to know you.

Many thanks also to Victoria, Eitan, Francesca, Petra, Izhar, Arantxa, Veronica, Juan, Baoxu for the nice parties and weekends that we have spent together. Thanks for your kindness and friendship.

I was very fortunate to have met all of you and I would like to thank you all for your friendship.

I am also very grateful to my friends in Portugal and England (and elsewhere), for their support, understanding and encouragement when I most needed it. Obrigada por sempre me apoiarem e por me receberem sempre de braços abertos e sempre tão carinhosamente!

A very special thanks also to Nuno... you know why.

E um muito obrigada aos meus pais, por todo o apoio incondicional, dedicação e aconselhamento que me deram durante estes anos. Obrigada por tudo o que foram por mim!

List of Publications

1. *Ab Initio* and DFT Benchmark Study for Nucleophilic Substitution at Carbon ($S_N2@C$) and Silicon ($S_N2@Si$)
Bento, A. P.; Solà, M.; Bickelhaupt, F. M.
J. Comput. Chem. 2005, 26, 1497
2. Nucleophilic Substitution at Silicon ($S_N2@Si$) via a Central Reaction Barrier
Bento, A. P.; Bickelhaupt, F. M.
J. Org. Chem. 2007, 72, 2201
3. E2 and S_N2 Reactions of $X^- + CH_3CH_2X$ ($X = F, Cl$).
An *Ab Initio* and DFT Benchmark Study
Bento, A. P.; Solà, M.; Bickelhaupt, F. M.
J. Chem. Theory Comput. 2008, 4, 929
4. Frontside versus Backside S_N2 Substitution at Group-14 Atoms:
Origin of Reaction Barriers and Reasons for their Absence
Bento, A. P.; Bickelhaupt, F. M.
Chem. Asian J. 2008, 3, online
5. Nucleophilicity and Leaving-Group Ability in Frontside and Backside S_N2 Reactions
Bento, A. P.; Bickelhaupt, F. M.
J. Org. Chem. 2008, 73, online

